CHEMICAL REVIEWS

pubs.acs.org/CR

Review

Interfaces and Interphases in All-Solid-State Batteries with Inorganic Solid Electrolytes

Abhik Banerjee,*,⊥ Xuefeng Wang,*,⊥ Chengcheng Fang, Erik A. Wu, and Ying Shirley Meng*

Cite This: https://dx.doi.org/10.1021/acs.chemrev.0c00101

Read Online

ACCESS | Metrics & More | Article Recommendations

ABSTRACT: All-solid-state batteries (ASSBs) have attracted enormous attention as one of the critical future technologies for safe and high energy batteries. With the emergence of several highly conductive solid electrolytes in recent years, the bottleneck is no longer Li-ion diffusion within the electrolyte. Instead, many ASSBs are limited by their low Coulombic efficiency, poor power performance, and short cycling life due to the high resistance at the interfaces within ASSBs. Because of the diverse chemical/physical/mechanical properties of various solid components in ASSBs as well as the nature of solid−solid contact, many types of interfaces are present in ASSBs. These include loose physical contact, grain boundaries, and chemical and electrochemical reactions to name a few. All of these contribute to increasing resistance at the interface. Here, we present the distinctive features of the typical interfaces and interphases in ASSBs and summarize the recent work on identifying, probing, understanding, and engineering them. We highlight the complicated, but important, characteristics of interphases, namely the composition, distribution, and electronic and ionic properties of the cathode−electrolyte and electrolyte−anode interfaces; understanding these properties is the key to designing a stable interface. In addition, conformal coatings to prevent side reactions and their selection criteria are reviewed. We emphasize the significant role of the mechanical behavior of the interfaces as well as the mechanical properties of all ASSB components, especially when the soft Li metal anode is used under constant stack pressure. Finally, we provide full-scale (energy, spatial, and temporal) characterization methods to explore, diagnose, and understand the dynamic and buried interfaces and interphases. Thorough and in-depth understanding on the complex interfaces and interphases is essential to make a practical high-energy ASSB.

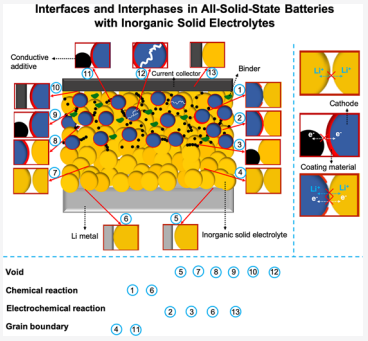

CONTENTS

Special Issue: Beyond Li-Ion Battery Chemistry

Received: February 5, 2020

1. INTRODUCTION

Lithium-ion batteries have become one of our life's necessities, ubiquitous and playing essential roles in a multitude of applications ranging from consumer electronics and electric vehicles, to aerospace products. They are widely used to store energy and provide power. As demand for electrification continues to grow, the adoption of Li-ion batteries in turn is growing exponentially. Thus, batteries that are safe and have high energy densities are exceedingly desired. Current Li-ion batteries that contain liquid electrolytes (LEs) have a significant risk of catching fire and even exploding due to the highly flammable organic solvents used in LEs. Replacing the liquid electrolytes with solid electrolytes (SEs) will definitely enhance battery safety, as flammability and electrolyte leakage are not issues for SEs. Additionally, SEs potentially enable the use of the Li metal anode, which would greatly increase the energy density of batteries.[1] As a consequence, all-solid-state batteries (ASSBs) are regarded as one of the critical future technologies and have continued to attract enormous attention over recent years.

ASSB research began with seeking suitable materials that can serve as SEs, namely, materials with high ionic conductivity (σ_{Li+} > 0.1 mS/cm, commonly referred to as "superionic conductors") but low electronic conductivity ($\sigma_e < 10^{-7}$ mS/cm). Such materials include polymer-, oxide-, and sulfide-based electrolytes.[2] Sulfide-based electrolytes have been shown to have higher ionic conductivities than oxide- and polymer-based electrolytes due to their *bcc*-like anion framework, favorable for Li-ion diffusion.[3] Recently, sulfide-based superionic conductors have achieved ionic conductivities close to or higher than those of conventional LEs (~1 mS/cm). These include $Li_7P_3S_{11}$ (17 mS/cm), $Li_{10}GeP_2S_{12}$ (12 mS/cm), and $Li_{9.54}Si_{1.74}P_{1.44}S_{11.7}Cl_{0.3}$ (25 mS/cm).[4−6] However, compared with LE cells, most ASSBs have higher polarization, lower capacity, and inferior power and cycling capabilities, which are attributed to severe interfacial problems.[7] Loose physical contact, the presence of grain boundaries, and chemical and electrochemical reactions, to name a few, all contribute to increasing resistance at the cathode−electrolyte, electrolyte−electrolyte, and electrolyte−anode interfaces (Figure 1). This is partially due to the SE properties; some have a narrow electrochemical stability window, meaning they begin to undergo oxidative decomposition at relatively low voltages, such as $Li_{10}GeP_2S_{12}$ (LGPS) at 2.15 V and Li_3PS_4 (LPS) at 2.41 V versus Li/Li^+.[8] Furthermore, due to the inherent chemical potential incompatibility of SEs with cathode/anode materials, spontaneous chemical reactions will occur. Such reactions will form a resistive solid electrolyte interphase (SEI) on the anode side or a cathode electrolyte interphase (CEI) on the cathode side, thereby hindering both Li-ion diffusion and charge transfer inside the ASSBs.[9,10]

Both computational and experimental methods are useful to explore the complex nature of the interfaces in ASSBs. Density functional theory (DFT) calculations and molecular dynamics simulations can provide microscopic viewpoints on thermodynamic stability, favorable kinetics, and atomic interactions at an interface. For example, the combination of $LiCoO_2$ (LCO) and $Li_2S−P_2S_5$ was predicted to be thermodynamically unstable since a reaction involving the interionic diffusion between Co and P at the interface is energetically favorable.[11,12] Although DFT calculations can predict the decomposition products, experimentally determining and confirming the presence of specific species and their distribution as well as their physical/chemical properties remains a challenging and rarely addressed problem. The physically buried nature of the interface along with the fact that most cathodes are composites that contain SE and carbon conductive additives, brings about much of the difficulty in isolating, probing, and identifying the chemical species. Such characterization requires proper experimental design and the use of various complementary techniques with a wide range of detection energy and spatial and temporal scales. Microscopy techniques, such as transmission electron microscopy (TEM), enables the visualization of the structure, morphology, and distribution at the interface. Spectroscopic techniques in turn provide the chemical state and electronic structure of the interfacial components. Electrochemical techniques, such as cyclic voltammetry (CV) and impedance measurements, can provide kinetic information on Li-ion diffusion and charge transfer at the interface. Identifying the chemical species and determining their distribution at the interface is very important because their chemical and physical properties directly govern the interfacial charge transfer resistance and ultimately, the electrochemical performance of ASSBs.

Since the demand and research interest for high-energy and safe ASSBs is increasing exponentially, this work seeks to focus on and summarize the current research progress on the interfaces in ASSBs and efforts for effective interfacial design and engineering. First, we break down each type of interface that exists in ASSBs. The interfaces between the electrolyte and cathode/anode are discussed separately in terms of the electrochemical reaction, chemical reaction, physical contact, and mechanical properties. We provide the fundamental understanding of the main causes of several issues, remaining challenges, and potential solutions regarding the interfaces in ASSBs. Lastly, we present various characterization tools to probe and diagnose the properties of the interfacial products, such as the structure, composition, distribution, and electronic and ionic diffusion to name a few. This information enables the engineering of ASSB interfaces, which is essential to make a practical ASSB with high energy density.

Here, we primarily focus on the interfaces and interphases of sulfide-based SEs in ASSBs because sulfides offer state-of-the-art battery performance and usually do not require the addition of LE. Although there are plenty of review articles on oxide-based SEs,[13−16] we discuss a few important interfacial parameters for oxide−SE interfaces to compare them with sulfide-based SEs. We only minimally describe polymer-based SEs, as there are

https://dx.doi.org/10.1021/acs.chemrev.0c00101
Chem. Rev. XXXX, XXX, XXX−XXX

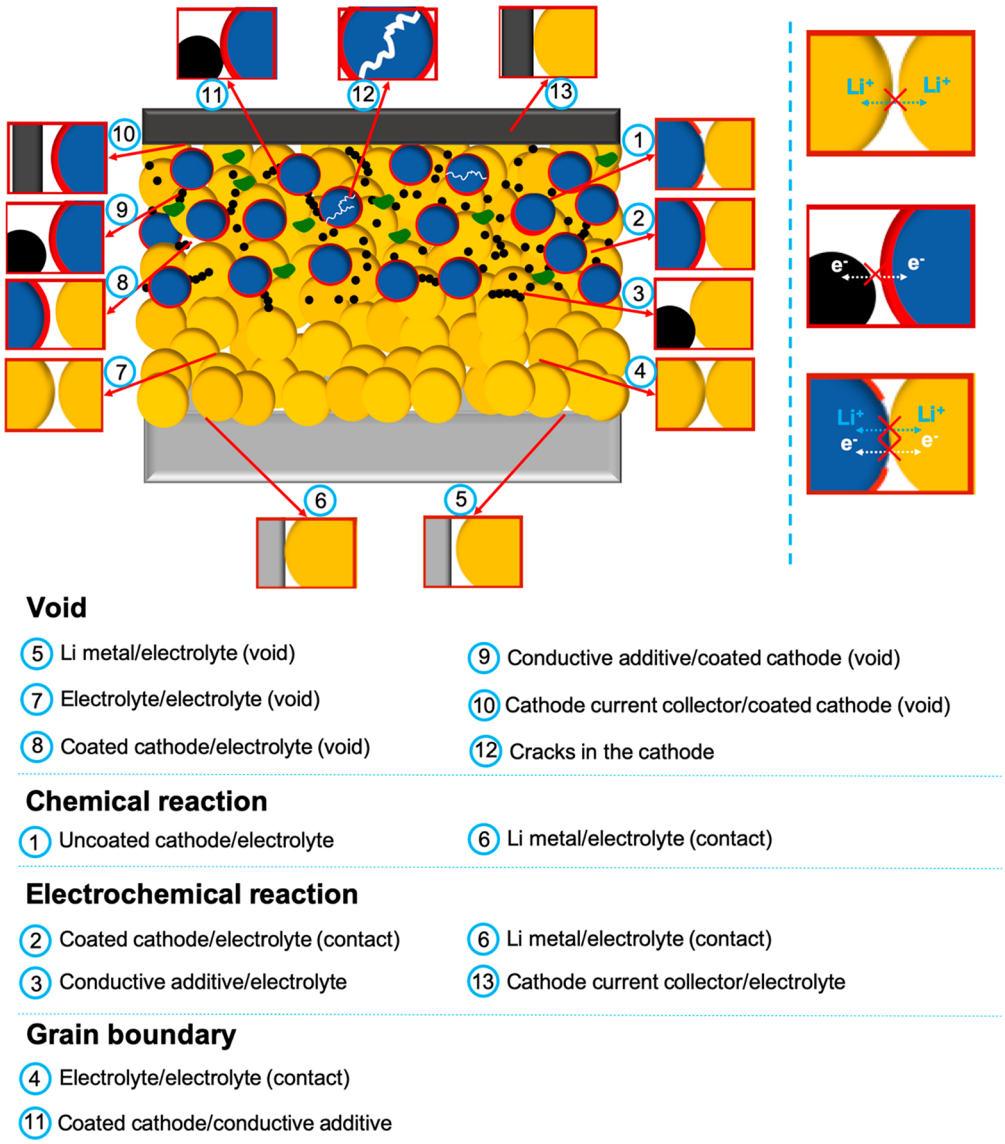

Figure 1. Schematic illustration of interfacial phenomena experienced in ASSBs.

already plenty of review articles on them.[17−20] We also discuss some very recent breakthroughs with halide solid electrolytes that offer a tantalizing road forward for the ASSB field.

2. INTERFACES IN ASSBS

Unlike LEs, SEs cannot flow or infiltrate into gaps and voids in an ASSB, resulting in poorer physical contact between particles. Since all of the components in ASSBs are solids, fabricating ASSBs requires stacking the cathode, electrolyte, and anode sequentially, resulting in numerous interfaces (Figure 1). As shown in Figure 1, 13 scenarios (that can all exist simultaneously in an ASSB) are listed, including the cathode−electrolyte, electrolyte−electrolyte, anode−electrolyte, current collector−electrolyte, and additive−electrolyte interfaces. These interfaces can be further categorized into the following classes: voids, those formed via chemical reactions or electrochemical reactions, and grain boundaries.

(1) Voids: although a high pressure (≥370 MPa) can be applied during cell fabrication, both the electrode and electrolyte are still far from the ideal closest-packing scenario; both remain quite porous. Such porosity usually ranges from 10%−40% depending on the pressure and mechanical properties of the electrolyte and electrode materials. Voids can also form during cell operation due to electrode pulverization caused by cracks forming in cathode particles and dendritic growth of Li metal. The presence of voids could (i) hinder Li-ion diffusion and charge transfer, resulting in high contact resistance, (ii) induce dendritic growth of Li metal, and (iii) increase the cell volume which decreases the volumetric energy density of ASSBs.

(2) Chemical reaction: If an electrode and the solid electrolyte have a mismatch of chemical potential, spontaneous chemical reaction(s) may occur once these two materials are put in contact. Consequently, solid electrolyte interphases (SEI) and cathode electrolyte interphases (CEI) form at the anode and cathode side, respectively. A beneficial SEI/CEI should be a passivating layer that is conductive to Li ions but not electrons, and extend the working voltage window of electrolytes, as shown in Figure 2. However, if the SEI/CEI is a mixed ionic and electronic conductor (MIEC), the SEI/CEI will

https://dx.doi.org/10.1021/acs.chemrev.0c00101
Chem. Rev. XXXX, XXX, XXX−XXX

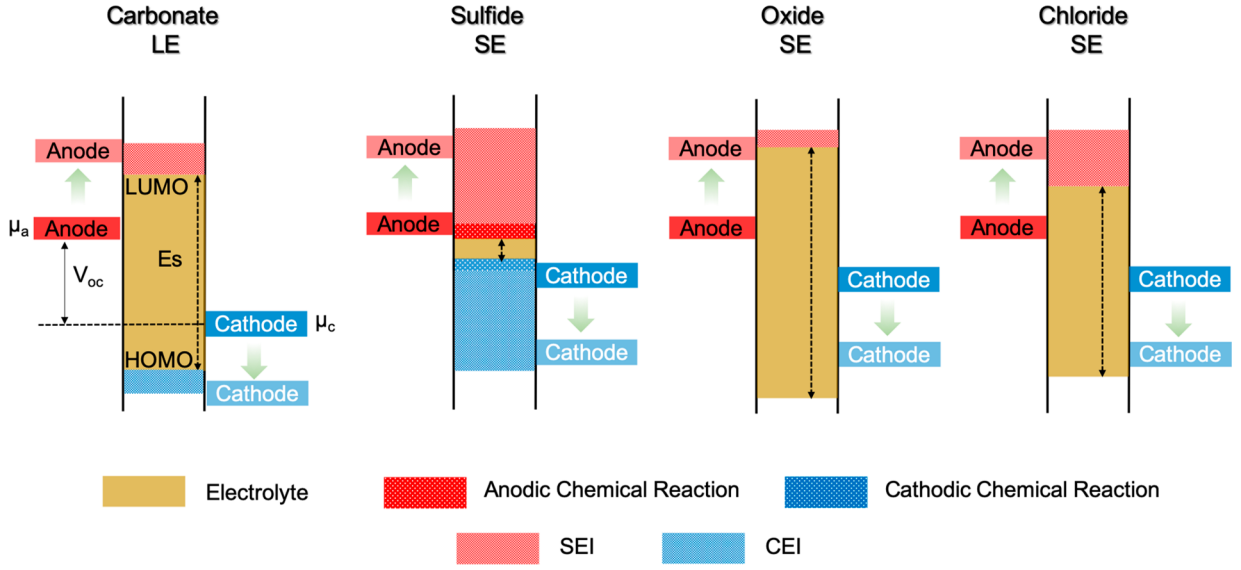

Figure 2. Schematic band diagrams of the HOMO and LUMO of different classes of electrolytes compared to typical μ_c and μ_a values. If the μ_c is below the HOMO of the electrolytes, a CEI will form; an SEI will form if the μ_a is above the LUMO of the electrolytes.

continue to grow, deteriorating the performance of ASSBs. Protecting the cathode/anode with relatively inert materials has proven to be an effective way to mitigate chemical reactions.

(3) Electrochemical reaction: most SEs have a narrow electrochemical stability window and cannot operate at the full voltage range of the cathode and anode materials. SEs can be oxidized at high voltages or reduced at low voltages if they have sufficient contact with electronically conductive materials, which can include the cathode/anode materials, current collector, or conductive additives. Note that oxide- and chloride-based SEs have a wider stability window than sulfide-based SEs (Figure 2); they are stable at high voltages but unstable at low voltages. The electrochemically decomposed electrolytes will also contribute to SEI/CEI formation and increase the charge transfer resistance. Coupling electrode materials with matching operating voltage windows and slowing down reaction kinetics are both beneficial as they reduce the electrochemical reactivity of SEs.

(4) Grain boundaries: a grain boundary is present if two particles are in contact and if they have different electrochemical potentials. The Li ions will then transfer from one particle to another particle, leaving a Li-deficient space-charge layer at the interface, which greatly suppresses ionic conduction at the interface.

3. ELECTROACTIVE INTERFACE OF SES

Aside from a high transference number, high ionic conductivity, and suitable mechanical properties, the most crucial criterion of a desired SE is that its highest occupied molecular orbital (HOMO) should be below the Fermi energy level of the cathode (μ_c) and its lowest unoccupied molecular orbital (LUMO) should be above the Fermi energy level of the anode (μ_a) (Figure 2). If the Fermi energy of the cathode is below the HOMO of the SEs, then oxidation of SE occurs at the cathode interface to form a CEI.[21] Analogous to this, if the Fermi energy of the anode is above the LUMO of the SEs, then reduction of the SEs occurs at the anode interface to form a SEI. The presence of a CEI or a SEI will increase resistance to both Li ion diffusion and charge transfer across the interface.

As the bottleneck of battery performance is strongly related with interfacial charge transfer kinetics, the electronic, ionic, and mechanical properties of the SEI/CEI are the most crucial parameters for building a better battery.[22−24] Such properties depend on its chemical composition and spatial distribution. Although SEI/CEI formation increases the interfacial charge transfer resistance, it may also passivate the interfaces in several ways such as by mitigating parasitic reactions, reducing ion dissolution, and accommodating the stress induced by electrode volume change; these may improve ASSB cycle life.[25−27] Important to note is that unlike LEs, SEs cannot infiltrate through the CEI/SEI if there are pores and cracks, making the mechanical properties of the SEI/CEI a more crucial consideration in ASSBs. Since most of ASSBs require a constant stack pressure to operate, the SEI/CEI is likely to experience additional stress from electrode volume changes.[28,29]

3.1. Electrochemical Stability Window of SEs

The grand potential diagram is usually applied to evaluate the electrochemical stability of SEs in equilibrium by changing the chemical potential of Li.[30,31] The grand potential diagram can show the stable voltage window of SEs and possible decomposition products when the chemical potential is outside the stability range. For example, the grand potential diagram of Li_6PS_5Cl (LPSCl) shows that reduction processes will occur at voltages below 1.7 V versus Li/Li^+ whereas oxidation will start at 2.3 V. Under phase equilibrium, the reduction products contain Li_3P, Li_2S, and LiCl, and the oxidation products contain S and P_2S_5. The phase equilibrium suggests that several binary materials are stable at 0 V (with Li metal): Li_2S, Li_3P, and Li_3N and LiF to name a few others. However, these SEs alone are not useful in ASSBs due to their poor Li ionic conductivity. In contrast, SEs such as LGPS and LPS are unstable at 0 V (as they have a favorable formation energy of −1.23 and −1.42 eV per atom, respectively).[11] The phase equilibria of LGPS contain Li_3P, Li_2S, and $Li_{15}Ge_4$ at 0 V whereas LPS contains Li_3P and Li_2S at 0 V, experimentally verified using XPS.[32,27] In addition, anodic decomposition of $Li_{0.33}La_{0.56}TiO_3$ (LLTO) and NASICON-type $Li_{1.3}Al_{0.3}Ti_{1.7}(PO_4)_3$ (LATP) occurs at 1.7

https://dx.doi.org/10.1021/acs.chemrev.0c00101
Chem. Rev. XXXX, XXX, XXX−XXX

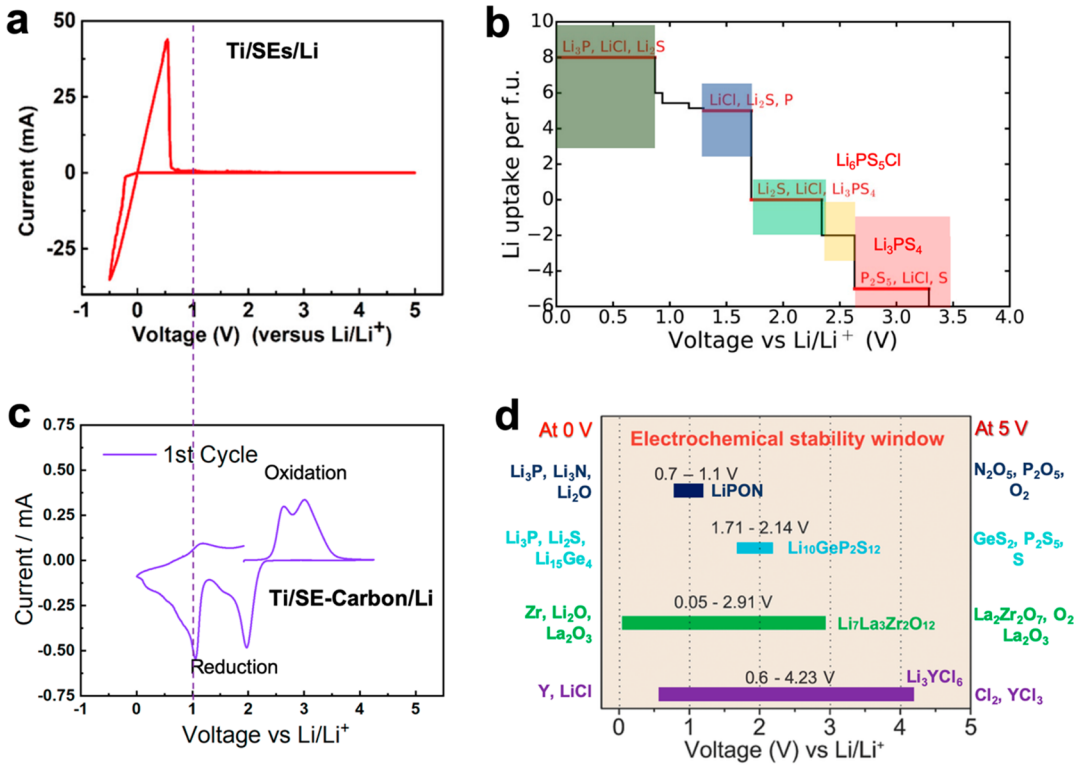

Figure 3. (a) Schematic of a CV scan where the SE is in direct contact with a flat Ti current collector; due to slow kinetics, no oxidation or reduction reactions can be seen. (b) Grand potential phase diagram of Li_6PS_5Cl (LPSCl). Below 1.7 V, LPSCl gets reduced and uptakes Li, while at 2.3 V and above, LPSCl gets oxidized and loses Li. The thermodynamically favored products at their respective voltages are highlighted. (c) Example of a CV scan where the SE is mixed with conductive carbon before contacting the Ti plunger. The faster kinetics of decomposition allow for the oxidation and reduction reactions to be visible. (d) Electrochemical stability windows for examples from the various classes (sulfide, oxide, nitride, chloride) of SEs.

and 2.4 V, respectively, due to reduction of Ti^{4+} to Ti^{3+}, in good agreement with CV experiments.[33,34] $Li_7La_3Zr_2O_{12}$ (LLZO) exhibits the lowest voltage stability of 0.05 V with negligible decomposition energy of −0.02 eV per atom. Such a low decomposition energy kinetically stabilizes LLZO at 0 V but results in poor wettability, which requires high-temperature heat-treatment to overcome.[11,35,36] In general, oxidative decomposition of sulfide-based SEs occurs at lower voltages than those of oxides and halides.[37,38]

It is important to note that these values are consistent with predictions from first-principles calculations but contrary to earlier CV measurements that had demonstrated the stability of SEs up to 5−10 V.[5,39] This discrepancy is likely caused by a lack of standard experimental procedures. When measuring the conductivity of a SE, if a flat metal plunger is used as the current collector, electronic contact with SEs is insufficient; the resultant SE electrochemical window is then usually overestimated as reactions would not be seen in CV measurements due to sluggish kinetics (Figure 3a). On the other hand, if conductive carbon is used between the plunger and SE, the decomposition of SE can begin to be clearly observed from a much lower voltage, that is, the emergence of multiple oxidation/reduction peaks in a CV scan. Such peaks from this measuring method match with the grand potential diagram of the DFT-calculated electrochemical stability (Figure 3c).[32,40−42] This modification in the experimental procedure increases the effective interfacial contact area with electronically conductive materials and thus increases the decomposition kinetics of SEs. Since this methodology can more accurately illustrate the electrochemical window of the SE, it should be widely applied for all kinds of SEs.

Obtaining an accurate electrochemical window for a SE is a necessary precondition before compatible cathode and anode materials can be examined.

The onset oxidation potential of a SE strongly depends on the anionic framework in the structure of SEs. The electronegativity of the anion and its charge density directly influence the oxidation stability of SEs. For example, the oxidation potential of SEs follows a general trend of chlorides > oxides > sulfides > nitrides (Li_3YCl_6 > LLZO > LPS > LiPON), which matches the charge density trend ($N^{3-} > S^{2-} > O^{2-} > Cl^-$) (Figure 3d). This principle also works for halide-based SEs; among them, fluoride-based SEs have the highest oxidation stability while iodide-based SEs have the lowest.[43] However, the ionic conductivity of fluoride-based SEs is much lower than their counterparts. Thus, a balance of favorable properties must be found to fabricate an effective room-temperature (RT) ASSB. Oxidation stability of oxide-based SEs depends on O^{2-}/O_2 gas release which is related to the oxygen atom bonding environment with neighboring atoms. For example, LLZO and LLTO oxidize at relatively low voltages of 2.91 and 3.71 V (vs Li/Li^+) respectively. The Li-deficient phase $La_2Zr_2O_7$ was generated from the oxidation of LLZO as identified by XPS.[44] LATP has the highest cathodic limit of 4.31 V versus Li/Li^+ with a low oxidation decomposition energy of −65 meV per atom at 5 V. The high oxidation stability of LATP originates from the overlap of energy orbitals between P and O, which form a strong covalent bond.

On the other hand, the reduction potential of a SE depends on its cation framework, especially the accessible lower oxidation states of the cation and its thermodynamic reduction potential. LiPON and LPS-based SEs contain phosphorus in the P^{5+} state

https://dx.doi.org/10.1021/acs.chemrev.0c00101
Chem. Rev. XXXX, XXX, XXX−XXX

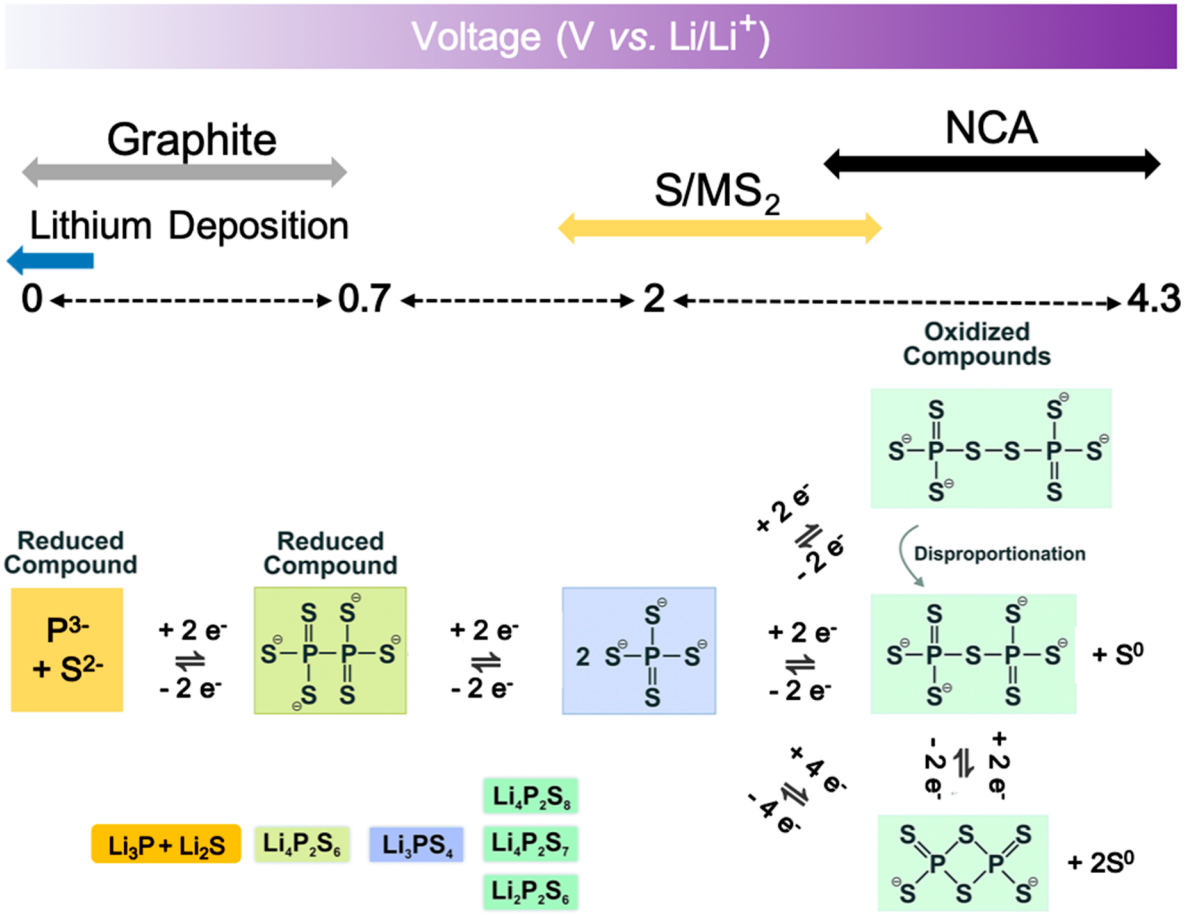

Figure 4. Possible interfacial reactions of sulfide SEs at a wide range of operating voltages. Top: The arrows correspond to the voltage ranges when using graphite, Li metal deposition, layered oxide cathode (NCA), Li−S, or metal sulfide. Bottom: The possible redox reactions at the corresponding voltage windows to illustrate the possible oxidation or reduction species. Reproduced with permission from ref 45. Copyright 2017 American Chemical Society.

which can be reduced to P at a lower oxidation state. This also applies to other transition metal-based cationic centers such as Y^{3+}, Zr^{4+}, and Ti^{4+}; they can be reduced to a lower valence oxidation state (e.g., Ti^{4+} to Ti^{3+}) or even to the final metallic form (Y^{3+} to Y^0). The extent of reductive decomposition depends on the amount of electrons transferred during reduction, such as eight electrons from P^{5+} (in PS_4^{3-}) to P^{3-} (as in Li_3P),[41,42] as opposed to one electron for Ti^{4+} to Ti^{3+}. Although thermodynamically possible, the occurrence of reduction processes is mainly controlled by kinetics. This being the case, a kinetically stabilized interface is favorable for passivation of the anode interface (e.g., with Li metal), which will be discussed in more detail later.

3.2. Tuning the Operating Voltage Window

If the operating voltage of the ASSBs exceeds the electrochemical stability window of SEs, the SEs will start to undergo oxidative/reductive decomposition (Figure 4). The decomposition products that form at the interface depend on the operating voltage and choice of electrode materials. For example, PS_4^{3-} can be oxidized to form sulfur-bridging (-S-) diphosphorus compounds and elemental S, whereas −P−P− bond formation takes place during the initial reduction of PS_4^{3-}, which is further reduced to Li_3P and Li_2S at voltages approaching 0 V. When sulfide-based SEs are coupled with high-voltage layered oxide cathodes such as $LiCoO_2$ (LCO) or $LiNi_xMn_yCo_{1-x-y}O_2$ (NMC), oxidative decomposition becomes more severe at higher voltages (as sulfide SE starts oxidative decomposition from very low voltages of 2−2.5 V vs Li/Li^+), resulting in a thicker CEI and a lower Coulombic efficiency (CE) during the first cycle compared with carbonate-based LE.[45] The extent of electrochemical decomposition, which is reflected by the first cycle CE also depends on the type of sulfide solid electrolyte. $Li_{9.54}Si_{1.74}P_{1.44}S_{11.7}Cl_{0.3}$, the highest Li-ion conductor (25 mS/cm at RT), readily oxidizes during cycling, resulting in a very low first cycle CE of 39%. In contrast, a relatively stable electrolyte, $Li_{9.6}P_3S_{12}$, which has an ionic conductivity 2 orders of magnitude lower (10^{-4} S cm^{-1} at RT), exhibits a higher first cycle CE of 73%.[6] Severe electrolyte oxidation therefore prevents the use of highly conductive SEs in conjunction with high-voltage cathodes. Thus, this is the most critical problem for most of the sulfide SEs as it is intrinsically unavoidable.[6] Using XPS, Koerver et al. showed a relative increase of the CEI when the voltage of a cell containing NMC was increased from 4.3 to 4.8 V. They also suggested that the continued growth of CEI with prolonged cycling, as well as SE oxidation on the current collectors, were the key reasons for capacity fade.[45] As an example, the $LiI-Li_3PS_4$ SE with the NCA cathode has the $I^-/I^{3-}/I_2$ redox couple along with the existing S^{2-}/S^0 redox couple, making the SE subject to decomposition, causing a large polarization and capacity fade.[46] In contrast, when TiS_2 and sulfur are used as the cathode, since the operating voltage is much lower (no greater than 2.4 V, i.e., within the

https://dx.doi.org/10.1021/acs.chemrev.0c00101
Chem. Rev. XXXX, XXX, XXX−XXX

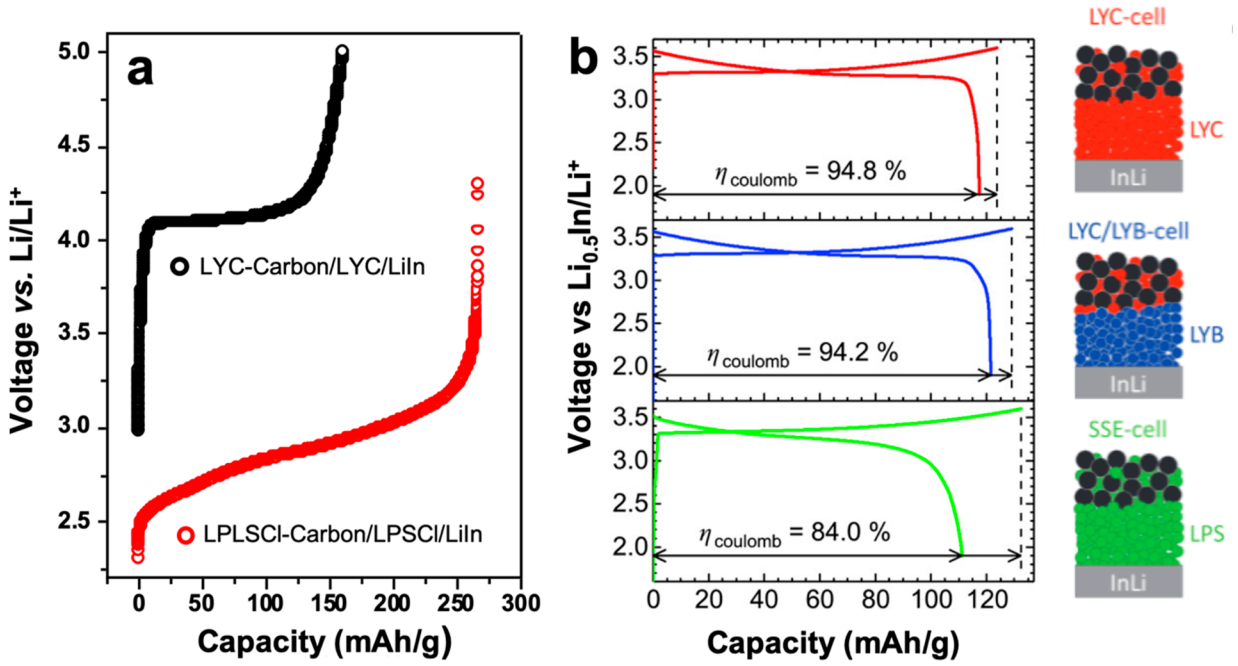

Figure 5. (a) Charging profile of LPSCl-carbon and LYC-carbon cathode composites made with 7:3 cathode: carbon wt % ratio using ball milling. The applied current density was 0.1 mA/cm^2 and the total cathode loading was 10 mg. (b) Charging profile with capacity and Coulombic efficiency of LCO with LYC, LYB, and LPS SE. Reproduced with permission from ref 48. Copyright 2018 Wiley-VCH Verlag.

stability window of the SE), the ASSBs with sulfide-based SEs show stable performance.[47] Therefore, suitable screening of electrolytes and finding compatible electrode materials is essential to mitigate electrolyte oxidation to realize ASSBs with high energy density.

Experimentally, it is found that Li_3YCl_6 begins to decompose at 4.2 V, while LPSCl starts to decompose at 2.3 V (Figure 5a), which closely matches with the grand potential computation phase diagram.[43] When coupled with the LCO cathode, less oxidative decomposition of Li_3YCl_6 is expected than for LPSCl, which agrees with the experimental data; ASSBs with LCO/LYCl and LCO/LPS exhibit a first cycle CE of 94.8% and 84%, respectively (Figure 5b).[48] Thus, careful selection of the SE can help to improve the first cycle CE and reduce charge transfer resistance at the cathode interface. Substitution or doping is one of the methods to improve both the oxidation and reduction stability of SEs. For example, partial oxygen substitution in sulfide-based SEs was found to be effective in enhancing the oxidation stability of SEs such as $Li_{3.35}P_{0.93}S_{3.5}O_{0.5}$ and $Li_{10}GeP_2S_{12-x}O_x$ (x = 0.3 and 0.6).[49,50]

Although the decomposition of SEs is unavoidable during the first cycle, it can be mitigated in subsequent cycles through self-passivation of the formed CEI. For example, LPSCl starts to decompose at 2.5 V and delivers a high charging capacity of 250 mAh/g during the first charge. However, no discharge capacity from LPSCl was found when the cell was discharged to 2.5 V.[51] When it was coupled with the NCA cathode, the low-voltage sloping region (from 2.5 to 3.6 V) corresponding to LPSCl decomposition disappeared from the second charge even though it was present during the first cycle. This suggests that the formed CEI is able to serve as a protective layer that prevents the SE from decomposing further, which enables the use of high-voltage cathodes such as LCO at voltages up to 4.2 V with LPS-based SEs.[6] Zhu et al. proposed that both thermodynamic and kinetic factors are responsible for this phenomenon. In principle, the thermodynamic stability of the CEI is much higher than the pristine SE. The decomposition kinetics of the SE and the CEI are sluggish in nature considering that they are both electronically insulating materials.[52] The thermodynamic stability and sluggish decomposition kinetics of the CEI thus extends the operating voltage window wider than the intrinsic thermodynamic stability window of the host SE.[53] Similar phenomena have been found at the LCO−LiPON and $LiNi_{0.5}Mn_{1.5}O_4$−LiPON interfaces.[54,55] Although LiPON has an intrinsically narrow stability window (0.68~2.63 V vs Li/Li$^+$),[56] the stable CEI enabled an ASSB to cycle up to 5 V over several thousands of cycles, due to the high overpotential of oxygen evolution.

3.3. Kinetic Control of SE Decomposition

Although the decomposition of SEs is unavoidable at the first cycle, SE decomposition kinetics can be tuned to enhance the CE of ASSBs. Since SEs have poor electronic conductivity (10^{-8}−10^{-12} S/cm),[57−63] highly electronically conductive surfaces would promote the decomposition of SEs[40,41] such as the electrode materials and carbon additives.[7] The particle size of the cathode material greatly affects the interfacial contact and electrochemical performance, as Strauss et al. found that smaller NMC622 particles (<10 μm) exhibited higher capacity than larger ones (for a carbon-free composite cathode with Li_3PS_4 (Figure 6a)). A composite with smaller particles possesses an electronic conductivity two or more orders of magnitude higher than composites made with larger particles, while Li ionic conductivity remains the same, resulting in faster kinetics and higher utilization of the cathode material.[64] The addition of conductive carbon is usually necessary for most cathodes to reduce the impedance of the ASSB, since cathodes such as NCA, $LiFePO_4$ (LFP), and $LiNi_{0.5}Mn_{1.5}O_4$ (LNMO) typically have poor electronic conductivity. Kanno et al. observed severe decomposition of LGPS at carbon surfaces (regardless of the anode used, whether Li or $Li_{0.5}In$) resulting in a low CE.[65] Zhang et al. also found that the decomposition of LGPS is directly related to the amount of carbon used (Figure 6b). For example,

https://dx.doi.org/10.1021/acs.chemrev.0c00101
Chem. Rev. XXXX, XXX, XXX−XXX

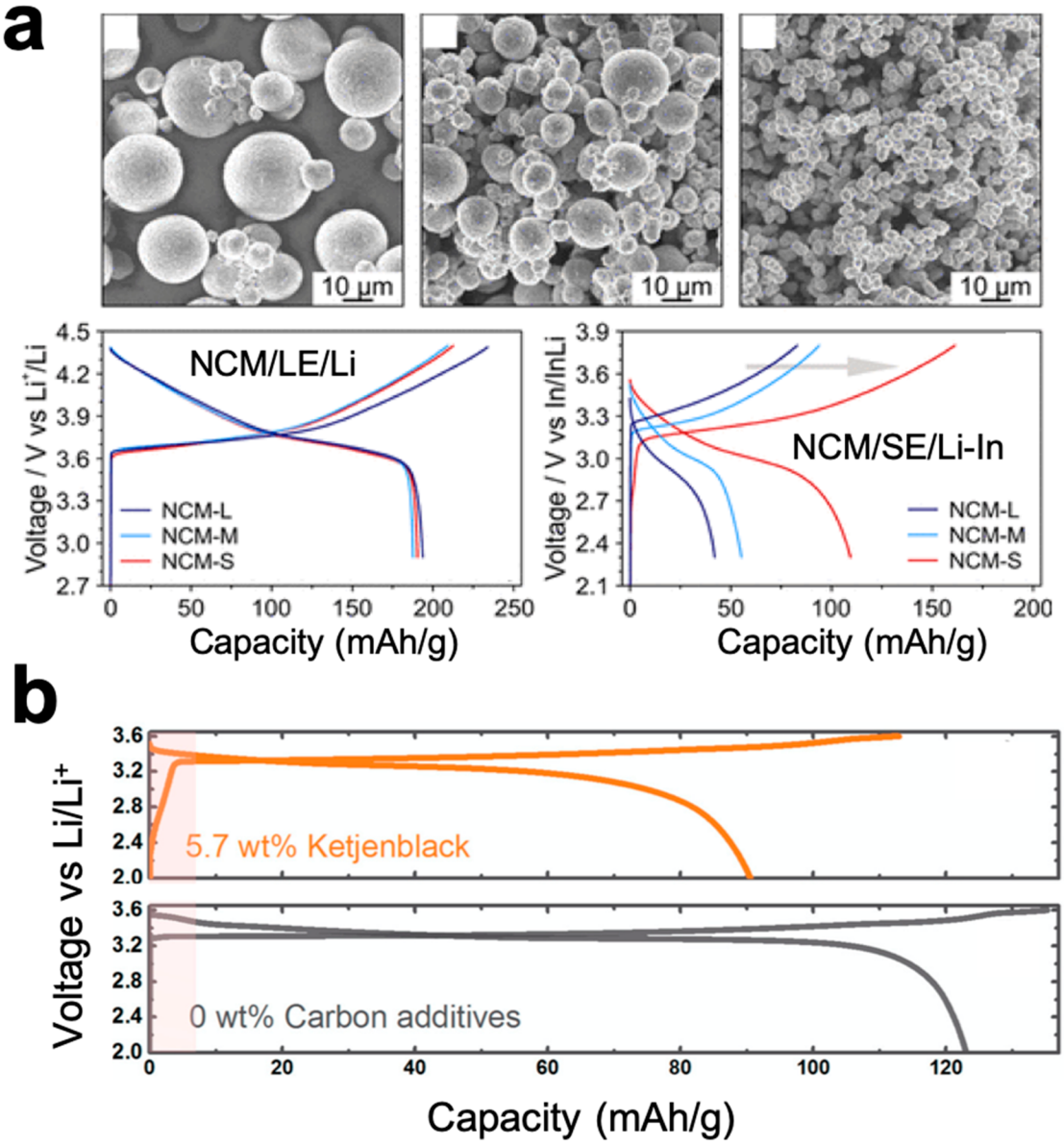

Figure 6. (a) SEM images of different sizes of NCM particles and the effect of NCM particle size on performance of carbonate-based LE and Li_3PS_4 SE cells, Reproduced with permission from ref 64. Copyright 2018 American Chemical Society. (b) Initial charging slope of LCO-LGPS solid-state cell with and without carbon. Reproduced with permission from ref 66. Copyright 2017 American Chemical Society.

the initial charging slope that originates from the oxidation of SE does not exist for the LCO-LGPS-based ASSB but it appears when conductive carbon is added into the composite mixture. They have also shown that increasing the carbon amount in the cathode composite resulted in an increase of the cathode interfacial resistance and a lower first cycle CE. This suggests that the kinetics of electrolyte decomposition is faster on highly electronically conducting surfaces such as carbon.[66,67] Therefore, the optimization of cathode composites, using a minimal amount of carbon, is paramount to reduce SE decomposition while maintaining the high performance of the cathode.

Furthermore, the type of carbon used in the cathode composite plays an important role with regards to the decomposition kinetics of SEs. Meng et al. found that LPSCl decomposition is significantly lowered when the lower surface area vapor-grown carbon fibers (VGCF) was used instead of the higher surface area acetylene black (AB) (Figure 7c). As a result, the initial decomposition slope is reduced, and the CE of the first cycle increased from 71 to 78% with NMC-VGCF cathode (Figure 7d).[41] A similar observation was reported by Passerini et al.[68]

3.4. Usage of SE Redox

Typically, the decomposition of electrolytes is irreversible; however, there are exceptions. Reversible decomposition of the Li_3PS_4 SE was recently identified by Tatsumisago et al. They demonstrated prolonged cycling and a reversible capacity of 185 mAh/g using a 7:3 (weight ratio) Li_3PS_4:carbon composite cathode with an operating voltage of 0.5 to 3 V vs Li/Li^+.[69−71] It is interesting to observe the reversible change of the S K-edge and P K-edge in the XAS spectra during charging and discharging (indicative of the redox related to S and P). It is believed that the P−S covalent bonds still exist after delithiation of Li_3PS_4 which helps to reversibly change the electronic structure of Li_3PS_4.

https://dx.doi.org/10.1021/acs.chemrev.0c00101
Chem. Rev. XXXX, XXX, XXX−XXX

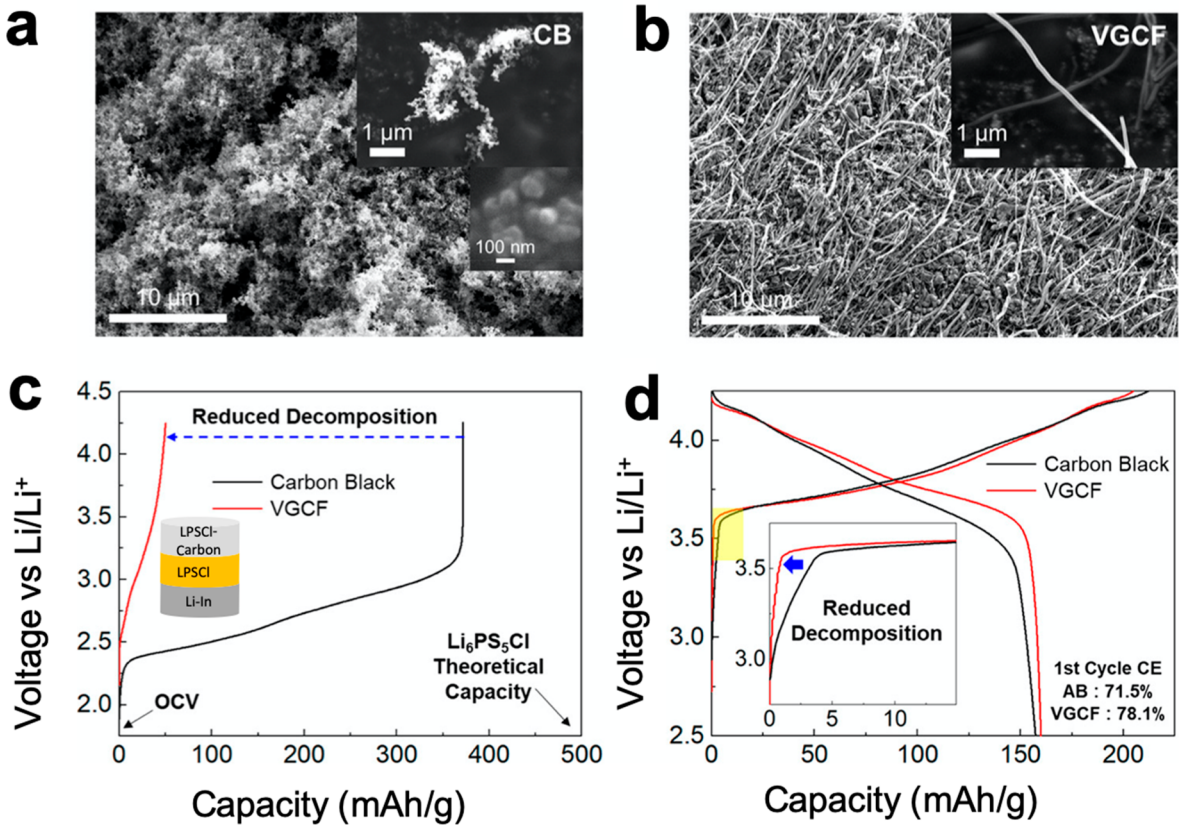

Figure 7. SEM images of (a) carbon black (CB) and (b) vapor-grown carbon fibers (VGCF) showing their different size and morphology. (c) Charge voltage profiles of Li−In | Li_6PS_5Cl | Li_6PS_5Cl−C cells using 30 wt % CB (surface area: ∼80 m^2/g) versus VGCF (surface area: ∼24 m^2/g). (d) Charge and discharge voltage profiles of Li−In | Li_6PS_5Cl | NCM811 cells using 1 wt % of CB versus VGCF. Reproduced with permission from ref 41. Copyright 2019 American Chemical Society.

Reversible decomposition of the sulfide-based SE LPSCl was also confirmed by Meng et al.; they showed complete reversibility of LPSCl within the window of 0−4 V versus Li/Li^+ (Figure 8a). XPS peaks of S and P_2S_5 appear after the oxidation of LPSCl at 4 V, resulting in an increased cathode charge transfer impedance by 2 orders of magnitude (Figure 8b,c). Upon discharging, the impedance reverts to a value close to the original LPSCl value and the parent PS_4^{3-} (LPSCl) peaks reappear (after discharge to 1.3 V).[41] They also demonstrated that LiCl forms after oxidative decomposition during the first cycle which does not participate in redox; only the PS_4^{3-} unit reversibly changes during the subsequent charge/discharge process. Further reduction to 0 V results in Li_3P and Li_2S at the interface (Figure 8b,c). It is interesting to note that the interface impedance at the fully discharged state is much lower than that at the fully charged state, implying that the cathode interfacial charge transfer resistance is the more significant consideration for ASSBs that comprise of sulfide-based SEs.

Of particular interest, the reversible kinetics of sulfide-based SEs lies within the operating voltage of a Li−S battery. For example, $Li_7P_3S_{11}$ (ball milled composite with conductive carbon) exhibits a reversible capacity of 225 mAh/g after 10 cycles (blue dots, Figure 9a), similar to the ball-milled composite mixture of Li_2S−$Li_7P_3S_{11}$ (1182 mAh/g, which exceeds the theoretical capacity of Li_2S) (red dots, Figure 9a).[72,73] In addition, the dQ/dV plot for $Li_7P_3S_{11}$ and the Li_2S−$Li_7P_3S_{11}$ composite have their corresponding redox peaks within the same voltage range (Figure 9b). This result signifies that $Li_7P_3S_{11}$ contributes to the extra capacity, as both processes operate within the same voltage range and thus would simultaneously participate in the redox process. This is quite a unique advantage of using sulfide-based SEs for an all-solid-state Li−S battery.

Overall, electrochemical decomposition of SE appears to occur with all the well-known SEs at wide operating voltage ranges. Controlling the decomposition kinetics of SEs is the key to construct a stable SEI/CEI, thereby enabling an ASSB with a high-voltage cathode and the Li metal anode. As new SEs continue to be discovered and evaluated, research emphasis should be placed not on achieving high ionic conductivity, but rather on improving SE electrochemical stability, controlling SE decomposition kinetics, and determining the nature of the decomposition products.

4. CATHODE−SE INTERFACE

Takada et al. reported that the rate-limiting step for a LPS-based ASSB (with LCO as the cathode and graphite as the anode) was charge transfer through the cathode; interestingly, cells with LEs show the opposite trend.[9] The higher cathode charge transfer impedance likely arises from inadequate physical contact, chemical reactions, electrochemical reactions, or a space-charge layer that forms or takes place at the interface. In this section, we will focus on the cathode−electrolyte interface and, particularly, the effect of chemical reactions and inadequate physical contact.[45,67,74−77]

4.1. Chemical Reaction

Chemical reactions arise from a chemical potential difference between cathode materials and SEs. This difference will be more

https://dx.doi.org/10.1021/acs.chemrev.0c00101
Chem. Rev. XXXX, XXX, XXX−XXX

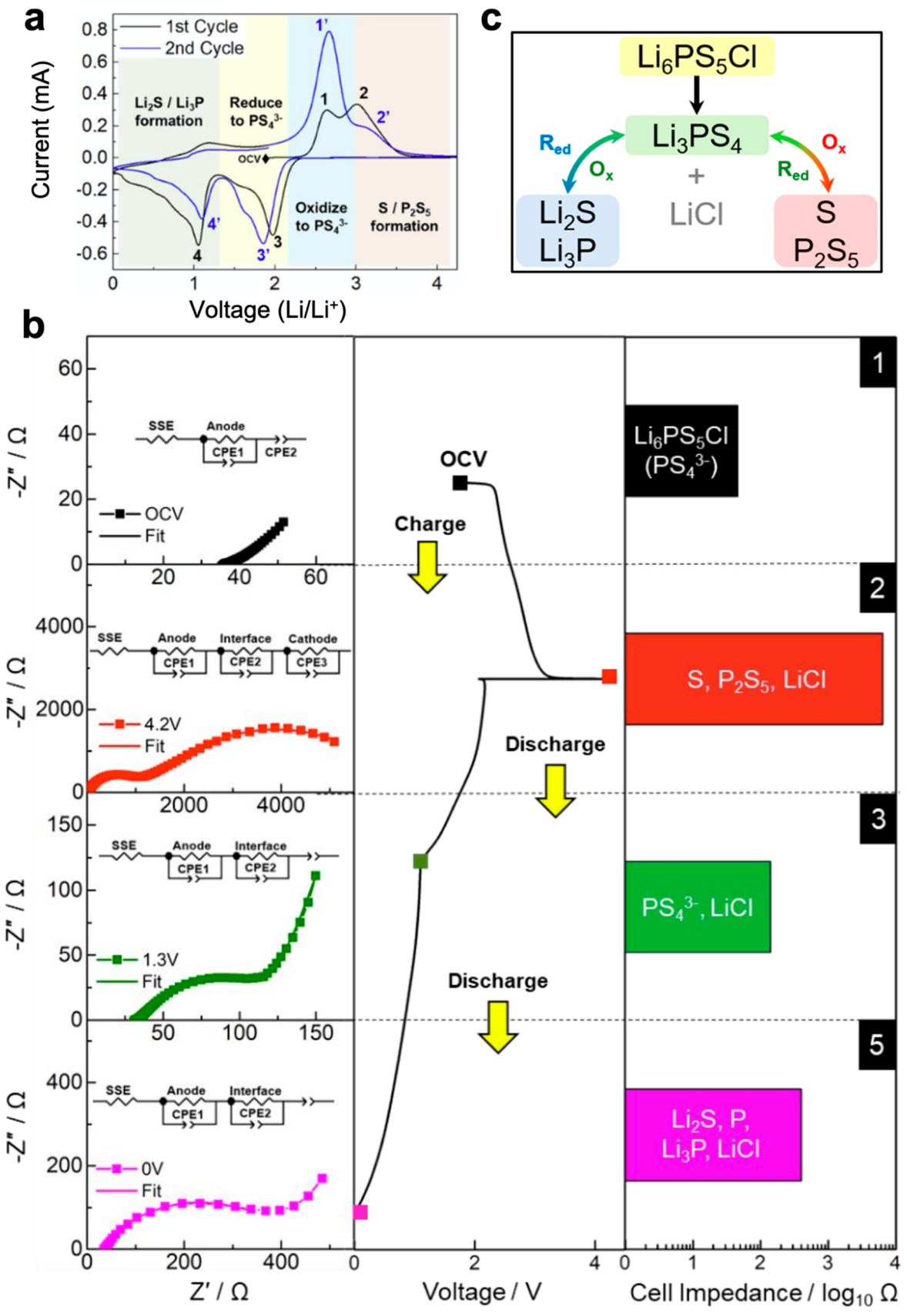

Figure 8. (a) Cyclic voltammograms for the initial two cycles of LPSCl-carbon composite within the voltage range of 0−4.2 V (vs Li/Li^+) at 100 μV/s starting from the OCV. (b) Nyquist plots at various cycling potentials of LPSCl-carbon composite representing the impedance changes (left). Normalized capacity versus voltage profiles are displayed for reference (middle). The bar graph represents relative differences in cell impedance at different oxidation or reduction states of Li_6PS_5Cl−carbon (right). (c) Schematic of details reversible oxidation and reduction pathway of Li_6PS_5Cl. Reproduced with permission from ref 41. Copyright 2019 American Chemical Society.

https://dx.doi.org/10.1021/acs.chemrev.0c00101
Chem. Rev. XXXX, XXX, XXX−XXX

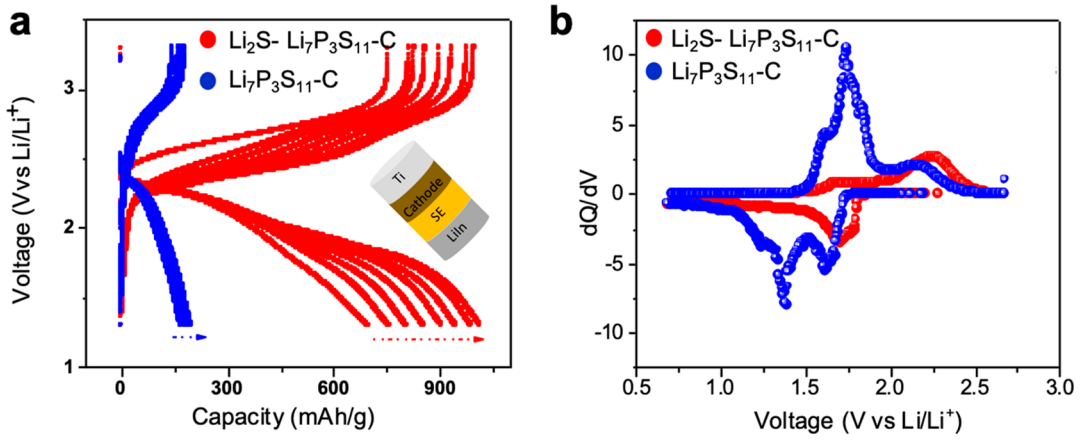

Figure 9. (a) Charge−discharge profile of $Li_7P_3S_{11}$−carbon (7:3 weight ratio) composite and Li_2S−$Li_7P_3S_{11}$−carbon composite (2.5:5:2.5), prepared using high-energy ball milling. The applied current density was 0.2 mA/cm^2 and the total loading was 7.5 mg/cm^2. The cell was fabricated with $Li_7P_3S_{11}$ as the SE layer and $Li_{0.5}In$ as the anode by applying a stack pressure of 370 MPa using Ti metal plungers as the current collectors (inset). (b) dQ/dV plot for both cathodes where their corresponding redox peaks are situated within the same voltage range (within 0.7 to 2.7 V vs Li/Li$^+$).

pronounced when electrochemical diffusion of Li ions occurs at the same time. This means that chemical reactions between cathode materials and SEs will become exacerbated during electrochemical cycling, especially at the charged state.

4.1.1. Thermodynamic and Kinetic Analysis by Computation. The chemical instability of sulfide-based SEs with oxide cathodes was primarily analyzed by computational methods.[11,30,78] A pseudobinary phase diagram with different compositional mixtures is usually established where all elements are equilibrated at the interface. The reaction energy of the phase equilibria is measured by the energy difference between the formation energy of reaction products and decomposition energy of the cathode and SEs, which is highly dependent on composition. For example, the decomposition energy of LCO reacting with both LGPS and Li_3PS_4 is −340 and −405 meV per atom, respectively, which signifies that LPS reacts more readily with LCO than LGPS (Figure 10).[11] Compared with pristine LCO, delithiated LCO shows a lower reaction energy with LPS and LGPS (−564 and −499 meV per atom), which indicates that the extent of interfacial reaction is also dependent on the state of charge. This difference is mainly because more of the cobalt is at a higher oxidation state (Co^{4+}), which has a greater tendency to react. As a result, Co_9S_8, Li_2SO_4, and Li_3PO_4 formed at the interface. A similar trend was noticed regardless of the transition metal (TM) layered oxide cathodes and sulfide SEs used, such as LPSCl and NCA.[51]

It is important to note that the interfaces between oxide-based SEs and oxide cathodes are quite stable compared to sulfide-based SEs; the reaction energy of the former is negligible and 2 orders of magnitude lower than the latter.[51] The phase equilibria decomposition energy between LLZO and LCO/$Li_{0.5}CoO_2$ is 1/53 meV per atom. It is interesting to notice that $Li_{0.5}CoO_2$ is one of the major reaction products when LCO reacts with oxide SEs. The oxidation state of Co in $Li_{0.5}CoO_2$ is Co^{4+} while it is usually reduced to Co^{2+} when it reacts with sulfide SEs. This is because the sulfide species is more polarizable, meaning it can more readily reduce the TM to a lower oxidation state whereas the opposite occurs if the charge density of the anion is increased. Consistent with this trend, the reaction energy is also lower for phosphate-based SEs such as LATP.[79] This result was verified experimentally by Yoshinari et al. as they found that NCM performed better with LATP in ASSBs (higher capacity and better cyclic retention than thiophosphate-based SEs at 60 °C, (Figure 11a)). The better performance of NCM/LATP coincides with a negligible increase in impedance after cycling compared to the NCM/LPS interface (Figure 11b). Although layered TM oxides are quite reactive with sulfide-based SEs, their reactivity with oxide polyanionic SEs is quite low. For example, Figure 12a shows the thermodynamic reaction energy (and the corresponding volume change) of several Na-ion battery electrodes (cathodes, Na metal, and the $Na_2Ti_3O_7$ anode) against one NASICON (oxide) electrolyte and several sulfide SEs.[80] A suitable selection of cathode, anode, and SE should be based on materials with the least reaction energy and minimal volume change. It is interesting to note that most of the transition metal oxides are chemically more reactive than the polyanionic cathodes $NaFePO_4$, $NaFePO_4F$, $Na_3V_2(PO_4)_3$, and $Na_3V_2(PO_4)_2F_3$ (when paired with NPS and NPSe). In general, oxide-based SEs show much higher chemical stability than sulfides whereas SbS_4-based SEs are chemically more stable than PS_4 and PSe_4-based SEs.[80,81]

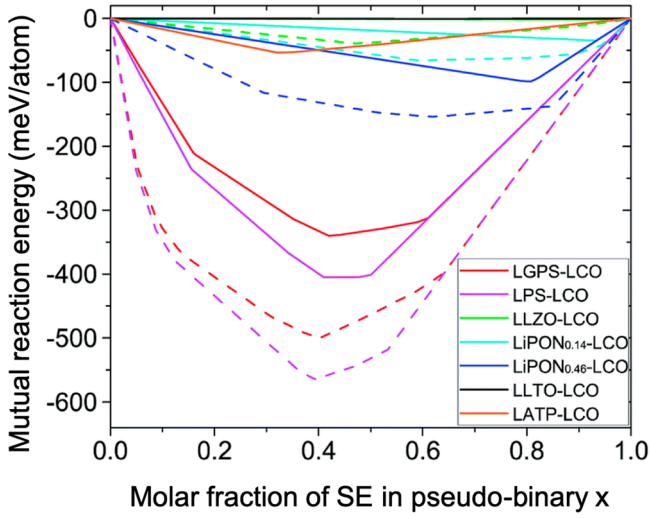

Figure 10. (a) Calculated mutual reaction energy of SE−LCO (solid lines) and SE−$L_{0.5}$CO (dashed lines) interfaces for several solid electrolytes such as LiPON, LLTO, LLZO, LPS, and LGPS. Reproduced with permission from ref 11. Copyright 2016 The Royal Society of Chemistry.

https://dx.doi.org/10.1021/acs.chemrev.0c00101
Chem. Rev. XXXX, XXX, XXX−XXX

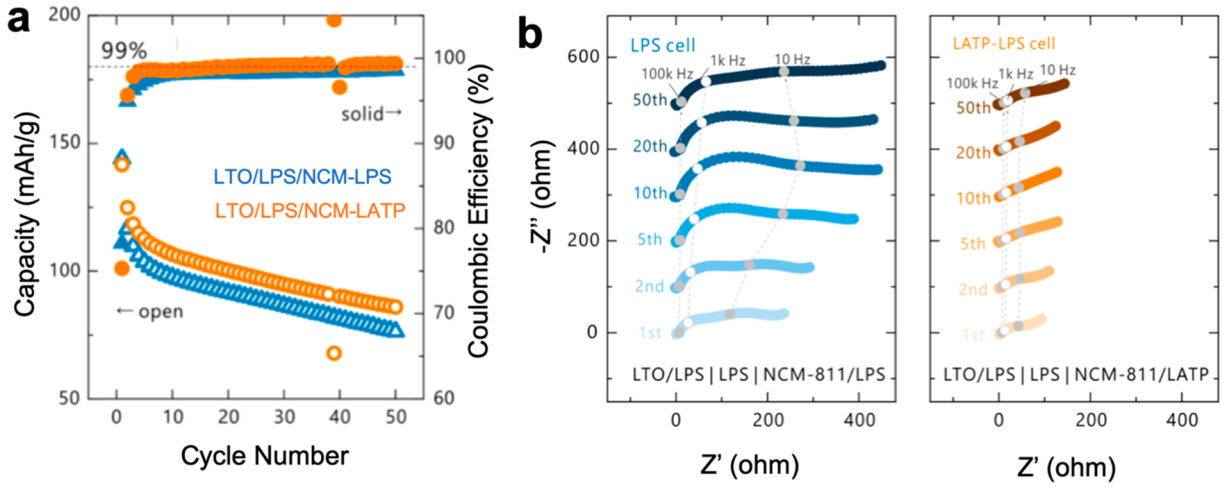

Figure 11. (a) Discharge capacity and Coulombic efficiency of LTO-LPS/LPS/LPS-NCM (orange) and LTO−LPS/LPS/LATP-NCM (blue) over 50 cycles. (b) Nyquist plots of the NCM-LPS cell and the (c) LATP-NCM cell after the 1st, 2nd, 5th, 10th, 20th, and 50th discharge at 150 °C. Reproduced with permission from ref 79. Copyright 2019 American Chemical Society.

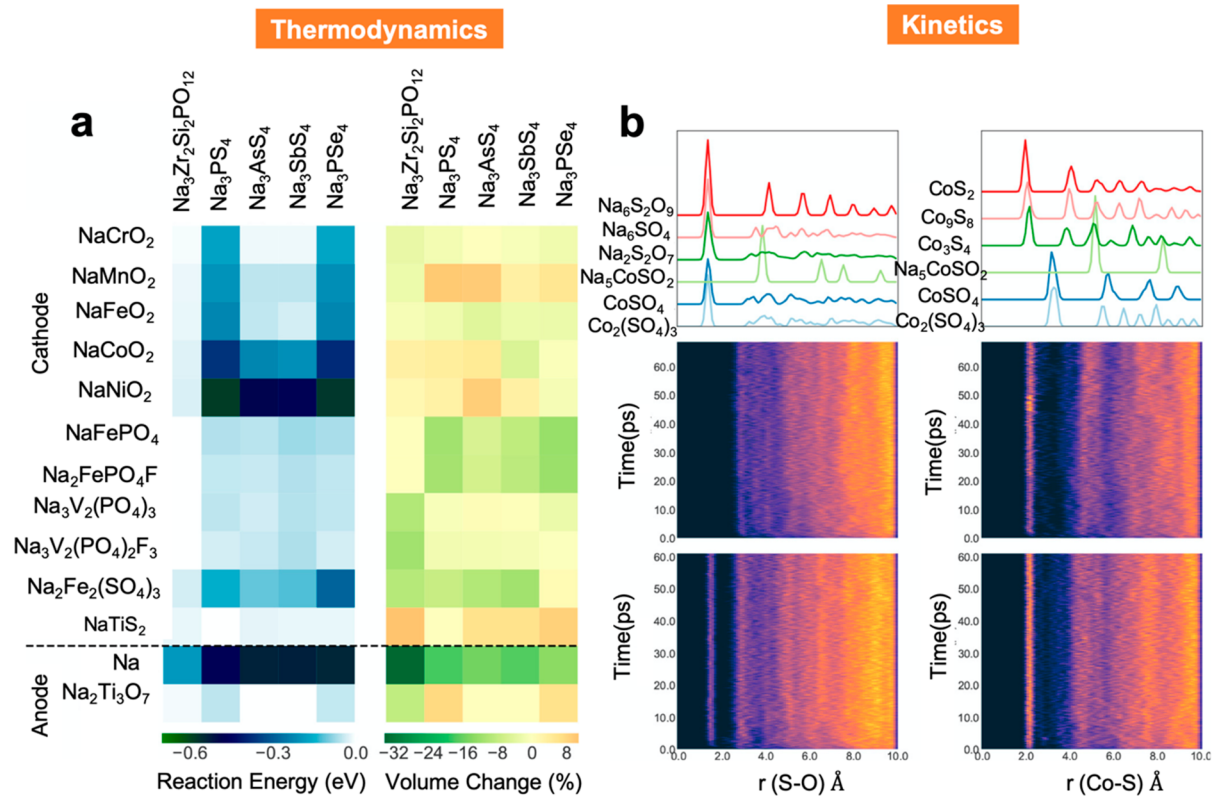

Figure 12. (a) Computed reaction energies (left) and volume changes (right) for several Na-ion electrode materials (in the discharged state) paired with SEs; (b) S−O and Co−S radial distribution functions of the cathode−SE interfaces with respect to AIMD simulation time (70 ps) for $NaCoO_2$−Na_3PS_4 and $Na_{0.5}CoO_2$−Na_3PS_4 interfaces. The S−O pair is instantaneously (and only) formed with the charged cathode, whereas the Co−S pair is found to form for both the charged and the discharged cathode. Reproduced with permission from ref 80. Copyright 2018 American Chemical Society.

However, it is important to note that the interfacial decomposition energy is calculated based on thermodynamics, which is not always in good agreement with experimental observations, where the interfaces are formed at RT. The decomposition energy calculation is more consistent when the composite mixture is heated at high temperatures to overcome the kinetic barrier limitation. Aside from thermodynamic calculations, the kinetic activation barriers for bond breaking and the diffusion limitation of atoms across the interface should also be taken into consideration. Although oxide-based SEs have a lower decomposition energy than sulfides, the cathodic interfacial resistance is sometimes larger for oxide SEs. This is due to the high-temperature annealing (previously mentioned to enhance the contact between oxide-based SEs and cathodes) that facilitates reaction kinetics. Ab initio Molecular Dynamics (AIMD) simulations is one of the computational methods to probe the kinetic reactivity at the interface. Tang et al. applied AIMD to study the reaction between $NaCoO_2$/$Na_{0.5}CoO_2$ and

https://dx.doi.org/10.1021/acs.chemrev.0c00101
Chem. Rev. XXXX, XXX, XXX−XXX

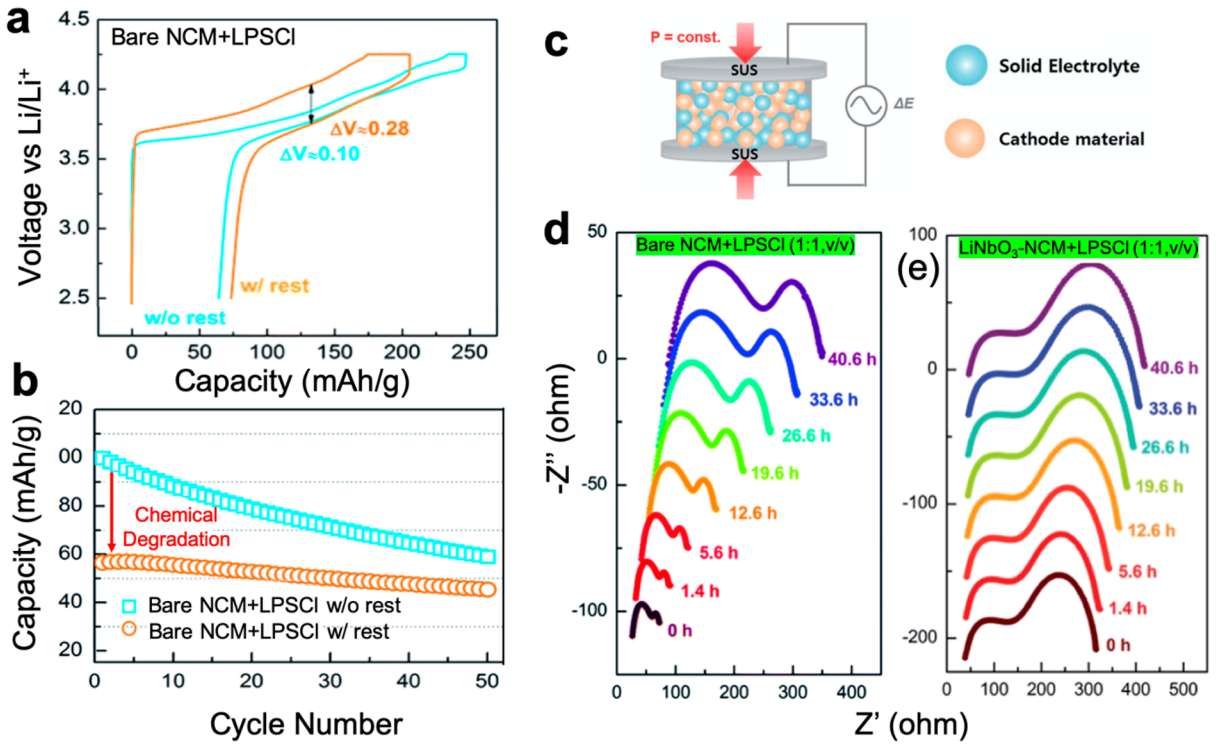

Figure 13. Effects of chemical instability at the cathode−SE interface on the electrochemical performance of ASSBs. (a) Solid state electrochemical profile of the first cycle of the fresh cell (without rest) and aged cell (with rest). The fresh cell showed a better capacity and lower polarization. (b) Capacity retention of bare NMC solid state cell with and without rest. (c) NCM was mixed with Li_6PS_5Cl and pelletized between two stainless steel plungers to measure the impedance as a function of time. (d) Impedance growth of the bare and (e) $LiNbO_3$-coated NMC-SSE cell with various dwell times at OCV. Reproduced with permission from ref 85. Copyright 2019 The Royal Society of Chemistry.

Na_3PS_4 along with the RDF approach to better understand the formation of interfacial products (Figure 12b). The results show that the Na−Na, S−O, P−O, and Co−S bonds form within the time scale of 60 ps. The Na−Na bond in NCO remains within the time scale for the bare NCO−NPS interface but vanishes for the charged NCO−NPS interface, which indicates that the charged cathode is more reactive than the discharged cathodes; for instance, the S−O bond forms at the charged state but not in the discharged state.[80] Banerjee et al. also used AIMD to study the NCA−LPSCl interface where the P−O bond forms along with the S−S, Ni−S, and Co−S bonds, agreeing well with the thermodynamic calculations.

4.1.2. Experimental Identification of Chemical Reactions. Chemical reactions were verified with several electrochemical techniques such as electrochemical charge/discharge profiles, impedance measurements, and GITT analysis.[82−84] Jung et al. fabricated a pellet made of a composite mixture containing NMC and Li_6PS_5Cl (with a 1:1 wt. ratio) and cycled one ASSB after resting for 48 h and another without any rest step. The cathode composite without rest exhibited a higher capacity with lower polarization (Figure 13a) but poorer capacity retention (Figure 13b).[85] This signifies an instantaneous chemical reaction between NMC and Li_6PS_5Cl even without applying any bias. To verify this, they measured impedance as a function of time without applying any bias voltage (Figure 13c,d). Both the bulk and grain boundary resistance increased by 400% in 48 h, as shown in Figure 13d. The bulk impedance increase can be due to the degradation of both the cathode and Li_6PS_5Cl, whereas interfacial impedance growth is due to formation of the CEI as an ion-blocking layer. Consequently, oxide cathodes with sulfide-based SEs exhibited significantly lower capacity due to the degraded cathode and increased interfacial resistance.

Understanding the chemical and physical properties of the interface is necessary because they can directly affect ASSB performance; having such knowledge will aid future composite electrode designs and interfacial engineering. Multiscale characterization has been applied to identify interfacial products, their spatial distribution, their ionic/electronic nature, and their effect on cell performance. Tatsumisago et al. conducted TEM and electron diffraction to observe long-range Co distribution at the bare cathode−SE interface and found that the interfacial layer is amorphous.[10] The amorphous nature may originate from the slow kinetics of interdiffusion between LCO and $Li_2S−P_2S_5$ during a long charging process. A similar observation was also made for LCO with $Li_{3.15}Ge_{0.15}P_{0.85}S_4$, where a thin amorphous layer was formed at the interface.[86] Surface-sensitive techniques such as XPS are useful to identify the interfacial products. For example, Banerjee et al. found PO^{3-}, SO^{3-}, and PSO^{-} as major interfacial products after cycling the NCA cathode with LPSCl SE.[51] This observation is in good agreement with DFT calculations.[86] Whether the interface that results from chemical reactions is passivated or not depends on the ionic and electronic conductivity of the SEI products. For example, Li_3PO_4 is an electronic insulator and an ionic conductor, allowing Li ions to transfer across the interface. On the other hand, TM sulfides are electronically conductive, which promotes the electrochemical decomposition of SE, resulting in a continuously growing interface that is detrimental to battery performance. This phenomenon is discussed in detail in a later section on long-term cycling stability.

https://dx.doi.org/10.1021/acs.chemrev.0c00101
Chem. Rev. XXXX, XXX, XXX−XXX

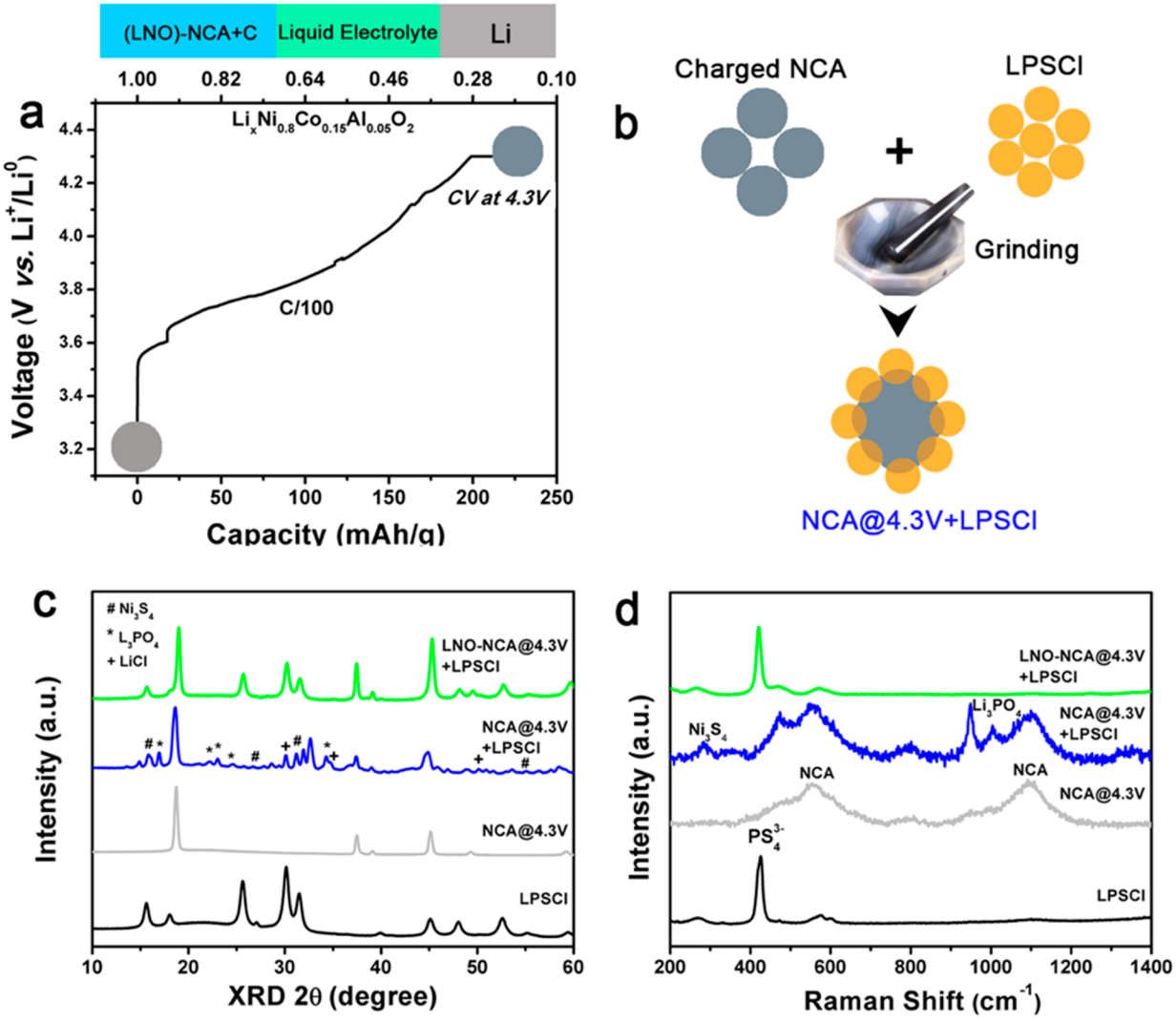

Figure 14. Characterization of the chemical reaction between LPSCl and NCA. (a) Potential curve of NCA charged to 4.3 V in a liquid cell; LNO-NCA exhibited a similar curve. (b) Schematic of sample mixture preparation. (c) XRD and (d) Raman spectra of each mixture at 4.3 V, compared to pristine LPSCl. Reproduced with permission from ref 51. Copyright 2019 American Chemical Society.

While there have been numerous studies on the cathode-electrolyte interface, most of these studies focus on interface after electrochemical cycling, which does not isolate the chemical reactions that occur at both the discharged and charged state; in other words, both the products from chemical reactions and electrochemical decomposition of SEs will be present. The resultant reaction products may also be different; for example, NiS, CoS, MnS, Li_2S, LiP_xCl_y, and LiCl were found to be the major products at the NMC−LPSCl interface at the discharged state, whereas $Mn_3(PO_4)_2$ or $Ni_3(PO_4)_2$, Li_3PO_4, PO_x, and SO_x ($2 < x < 3$) are detected after electrochemical cycling. These results indicate that electrochemical delithiation makes oxygen more reactive with P and S to form P−O and S−O bonds. Meng et al. succeeded in isolating interfacial chemical reactions from SE electrochemical decomposition reactions and identified the respective products at the pristine and charged states. They initially charged the NCA cathode to 4.3 V in a LE cell (Figure 14a) (as LEs do not decompose or react with NCA at 4.3 V), collected the charged NCA powder, and then mixed it with LPSCl (Figure 14b). Through this process, in terms of the chemical reaction between NCA and LPSCl, significant amounts of crystalline NiS, Li_3PO_4, and LiCl were detected by Raman and XRD at the charged state while their signals were much weaker at the pristine state (Figure 14c,d).[51] Figure 15a−c show a schematic of chemical and electrochemical reactions between an oxide cathode and sulfide solid electrolyte, where reaction kinetics is slow for the composite mixture (a relatively thinner interface even after a prolonged resting time), but more severe at the charged state (which forms a thicker interface). The thicker interface at the charged state arises from the occurrence of both chemical and electrochemical reactions. These results demonstrate the different mechanisms involved in the chemical reaction and electrochemical decomposition of SE, and their corresponding influence on the interfacial resistance and cell performance.

It is also important to realize that all of the sulfide-based SEs and charged cathodes are highly sensitive to the atmosphere,[87] so sample handling (such as isolating the sample from the cell), transport, and transfer into the measurement setup should be done in highly inert conditions. Even brief exposure may cause a difference in the measurement and batch-to-batch variation, which could lead to skewed interpretations of the interfacial reactions. It is also worth mentioning that sulfides are highly beam sensitive (electron, X-ray, and photon); beam-induced

https://dx.doi.org/10.1021/acs.chemrev.0c00101
Chem. Rev. XXXX, XXX, XXX−XXX

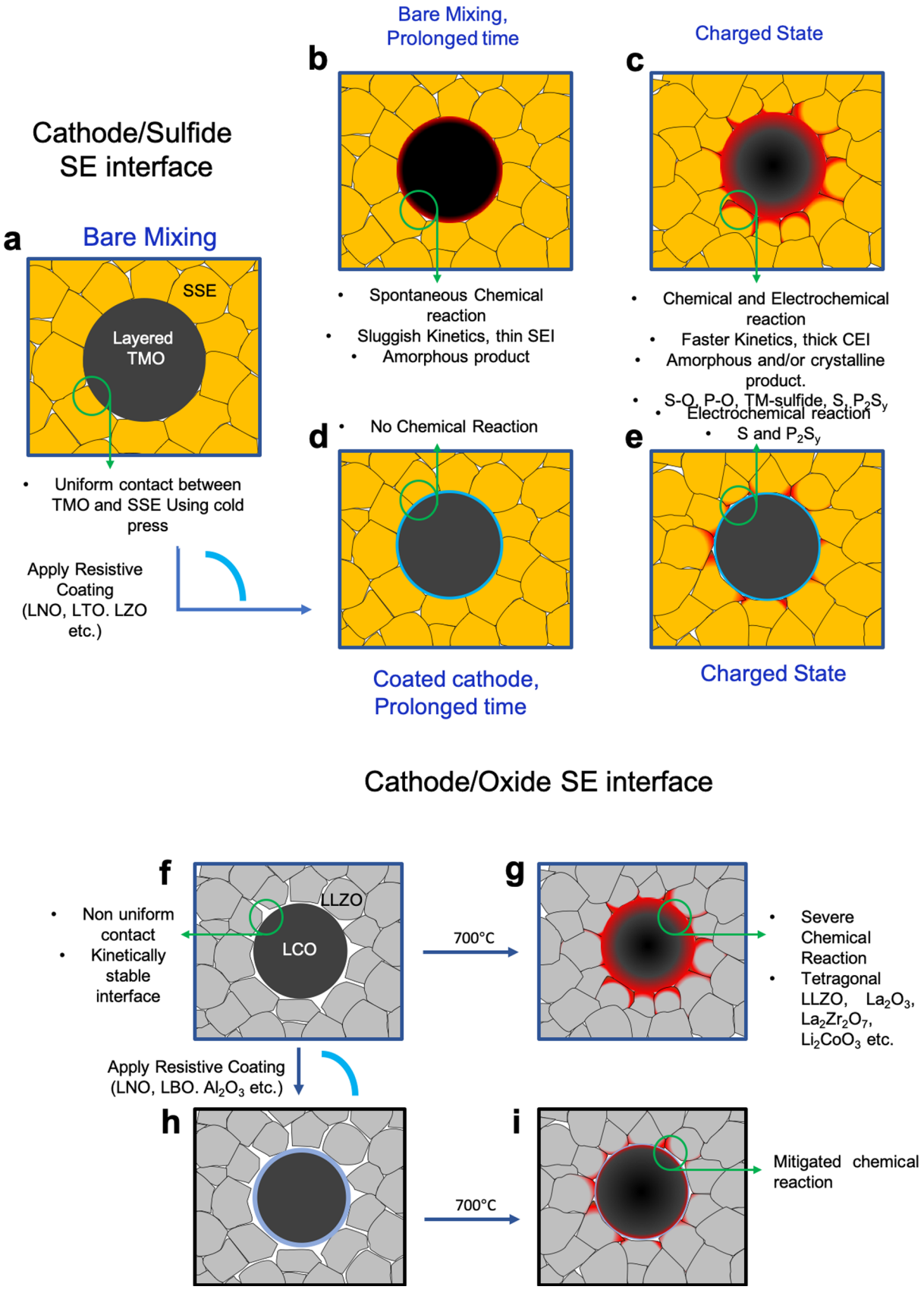

Figure 15. (a) Interfacial contact between uncoated TM layered oxides and sulfide SE is made by mixing and cold-pressing at >300 MPa. (b) Thermodynamically favorable and spontaneous chemical reaction occurs (red color) between uncoated TM layered oxides and SE interface over time. (c) Thicker CEI forms due to faster kinetics of the chemical reaction that occurs between TM layered oxide (at charged state) and SE, along with electrochemical decomposition of SE. (d) Thin conformal coating layer is applied to prevent chemical reactions; however, (e) an interface is still formed at the TM layered oxide−SE interface (at the charged state), which arises from electrochemical decomposition, (f) the kinetically stable LLZO

https://dx.doi.org/10.1021/acs.chemrev.0c00101
Chem. Rev. XXXX, XXX, XXX−XXX

Figure 15. continued

and LCO interface generates many interfacial gaps, (g) interfacial contacts are improved between LLZO and LCO by heating at high temperature, but severe chemical reactions occur at high temperature, generating unwanted side products at the interface. (h) Coating layer is applied on the LCO surface; (i) chemical reaction is mitigated for coated LCO when heated with LLZO.

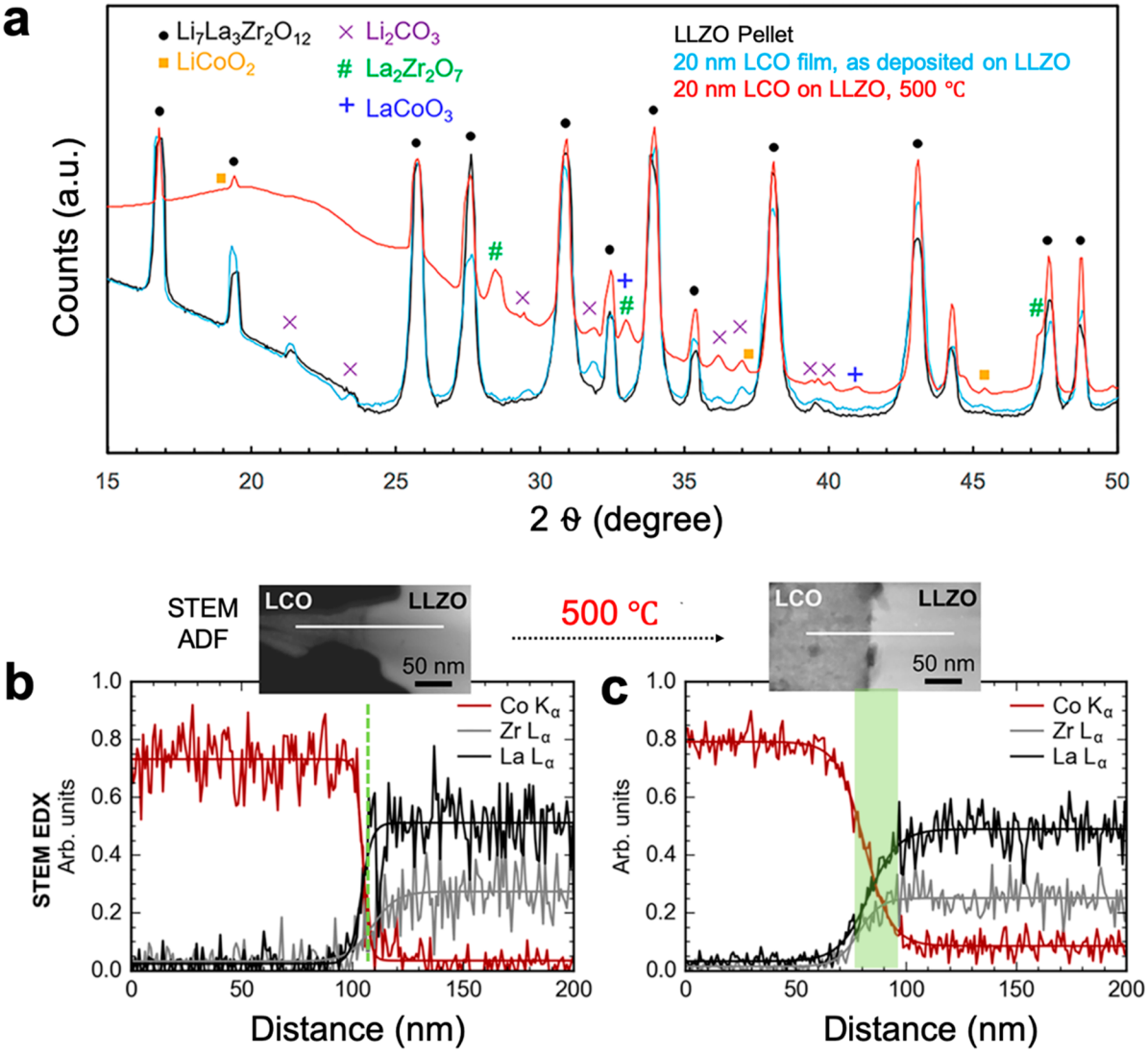

Figure 16. (a) XRD patterns of an LLZO pellet, LCO deposited on LLZO, and LCO−LLZO heated at 500 °C with the corresponding phases. FIB-milled sample of the LCO and LLZO interface (b) before and (c) after annealing with the corresponding EDX line scans (of Co, La, and Zr). Co, La, and Zr were shown to diffuse after annealing. Reproduced with permission from ref 91. Copyright 2018 American Chemical Society.

decomposition could also produce unexpected results. Thus, proper calibration and optimization of beam dosage and exposure time should be performed on samples before performing experiments.

According to DFT, the cathode interfacial chemical reaction is negligible for oxide-based SEs, but experimentally, it has been shown to be significant. Because of low elasticity and a lower surface energy (high crystallinity as well as having both ionic and covalent bond characteristics with a high bond dissociation energy), it is very difficult to form intimate contact between oxide SEs and an oxide cathode by merely hand mixing and pressing at RT (Figure 15f). Thus, high temperature (>700 °C) annealing is required to improve interfacial contact. However, such temperatures can initiate unwanted chemical reactions that can yield ion-blocking or electron-blocking layers that result in a high cathodic charge transfer resistance (Figure 15g).[88] Ogumi et al. performed CV on Li/LLZO/LCO thin films and observed broadened oxidation peaks of LCO, which is markedly different than typical LCO behavior with conventional LEs.[89] The poor performance is believed to originate from a chemical reaction at the interface; qualitatively, the color of LCO changed after annealing. Through TEM analysis using nanobeam diffraction, they identified the crystalline La_2CoO_3 phase at the interface which was predicted to be one of the major interfacial components through DFT calculations. Similar TEM observations of elemental diffusion across the interface were also found by Goodenough et al. in the mixed LCO/Al-doped LLZO cathode.[90] TOF-SIMS studies found that most of the elements (La, Zr, and Co) diffuse across ∼10 nm at the interface whereas Al diffuses everywhere. Such Al migration could cause a phase

https://dx.doi.org/10.1021/acs.chemrev.0c00101
Chem. Rev. XXXX, XXX, XXX−XXX

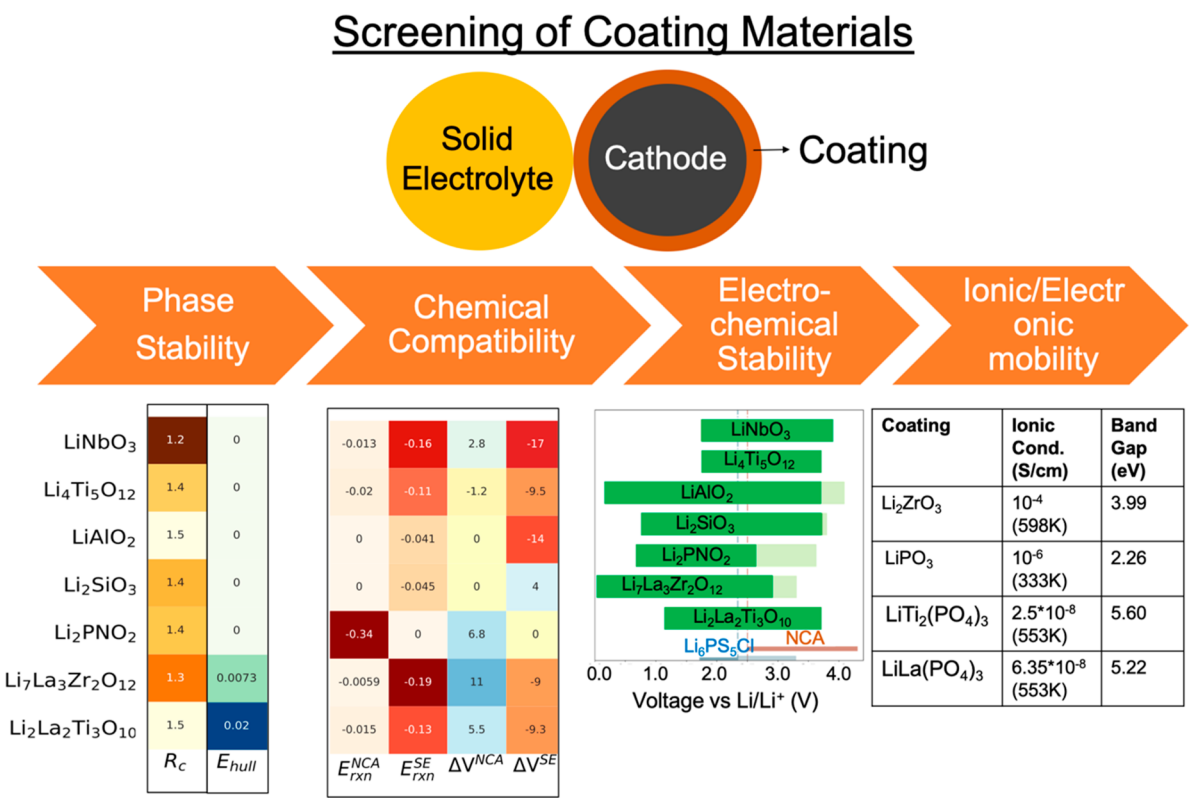

Figure 17. Necessary criteria for an effective cathode coating for ASSBs. Reproduced with permission from ref 51. Copyright 2019 American Chemical Society.

transition from cubic LLZO to tetragonal LLZO, which has a much lower ionic conductivity (10^{-7} S/cm). Thus, the presence of tetragonal LLZO can also increase the interfacial charge transfer resistance, hindering cycling performance.[90]

Although plenty of studies have been carried out on the LCO−LLZO interface, quantitative analysis remains minimal. Specifically, quantitative diffusion and phase transformation analyses can help to better design experiments to minimize interfacial resistance. For example, Vardar et al. explored the effect of annealing temperature and gas environments on the interface of a thin layer (<100 nm) of LCO deposited on top of a LLZO pellet.[91] The potential interfacial products were investigated with XPS, XRD, TEM, and XAS. The results show that the interfacial thickness is ∼20 nm for an annealing temperature of 250 °C and 100 nm for 500 °C. Li_2ZrO_7, $LaCoO_3$, and Li_2CO_3 were all found at the interface (using high-quality synchrotron XRD (Figure 16a)), resulting from interdiffusion of La and Co at high temperatures and the surface reacting with CO_2. Nevertheless, the Li_2CO_3 impurity was removed when the sample was heat-treated in an oxygen environment at 350 °C. Further interdiffusion was also verified by Vardar et al. where they found interdiffusion of Co, La, and Zr across the interface (via EDX line scan) after annealing the LLZO−LCO composite at 500 °C, though no interfacial elemental distribution was found without annealing.[91] These results indicate that optimizing the synthesis of SEs is essential to minimize the formation of impurities and thus reduce the interfacial resistance.

4.1.3. Space Charge Layer. The poor rate performance of ASSBs was also speculated to be due to a space charge effect at the cathode−SE interface. Both AIMD simulations and DFT calculations reveal that a space charge layer is expected to form when an oxide cathode is in contact with a sulfide SE.[92,93] As sulfides are more prone to oxidation than oxides, electrons can easily migrate from the sulfide SEs to the charged cathode.[94] In principle, Li ions will move away from this region to balance the charge, either toward the charged cathode by self-diffusion, or toward the anode under an applied charging voltage. Regardless, the end result is a Li-ion depletion layer. Experimentally, the existence of the space charge layer was hypothesized due to the observation of an additional oxidation slope in ASSBs during charging; if the depletion layer grew large enough to reach an electrode potential equal to that of the cathode, Li ions would then deintercalate from the cathode. Takada and Ohta et al. ascribed the limited rate performance of ASSBs to the formation of a space charge layer, which is closely related to vacancy formation and defect chemistry at the interface.[9,82,95,96] In other words, a localized electrostatic potential is produced at the cathode−SE interface, reducing the chemical potential at the SE interface, which ultimately results in a lower concentration of Li ions on the electrolyte side of the cathode−SE interface (compared to bulk SE). This suppresses Li-ion conduction across the interface.

Unfortunately, there has been no direct experimental observation of the space charge layer at the SE-oxide cathode interface, though experimental measurements have been attempted with LiPON and $LiCoO_2$. Such measurements employed an *in situ* Kelvin probe and electron holography experiments to measure the electrical potential distribution across the interface and Li depletion region.[97,98] Applying such techniques on thin film systems could elucidate the space charge layer phenomenon in ASSBs. While these proposed techniques can probe the local electrostatic potential across the interface,

https://dx.doi.org/10.1021/acs.chemrev.0c00101
Chem. Rev. XXXX, XXX, XXX−XXX

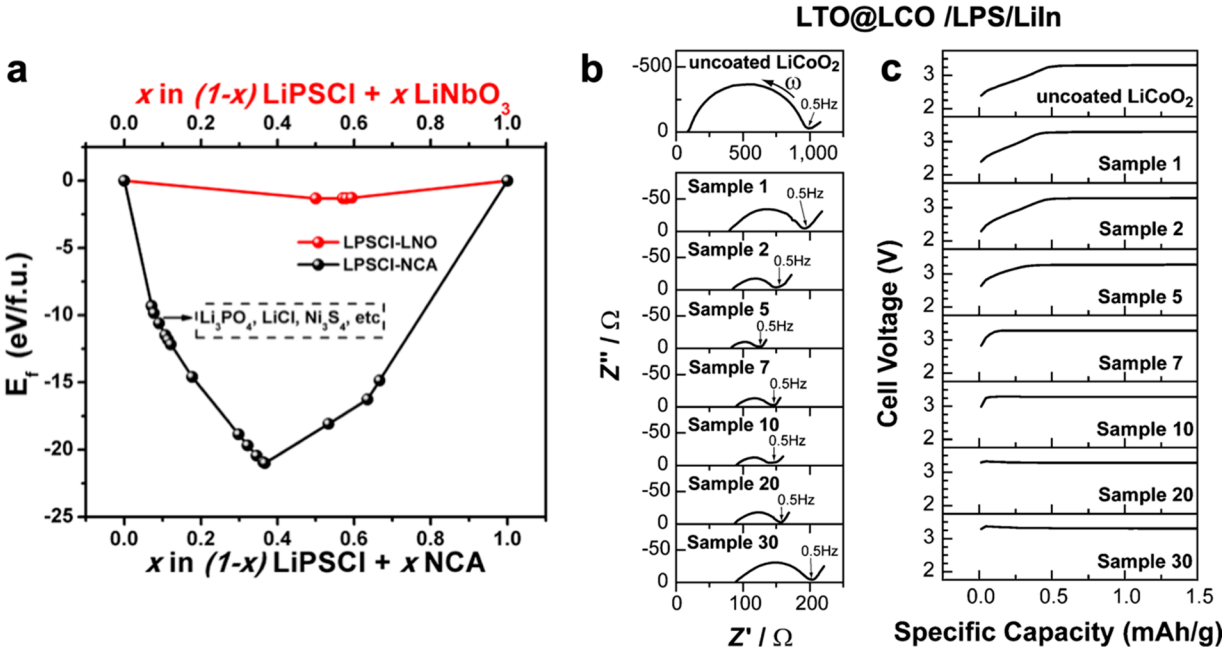

Figure 18. (a) Pseudobinary phase diagram of NCA−LPSCl and LNO−LPSCl. Reproduced with permission from ref 51. Copyright 2019 American Chemical Society. (b) Increasing thickness of LTO coating reduces the impedance and initial charging slope of LCO; the initial slope is hypothesized to be due to the space charge effect. Samples 1, 2, 3, 5, 7, 10, 20, and 30 corresponding to the LTO thickness in nm. (c) Voltage profiles illustrating the initial charging slope for the different LTO coating samples on LCO. Reproduced with permission from ref 83. 2006 Wiley-VCH Verlag.

the depletion layer has only been explained through numerical simulations so far.

4.1.4. Protective Coating Layer. Applying a conformal and chemically inert coating has proven to be effective at preventing chemical reactions between cathode materials and SEs, reducing the space charge layer effect, and lowering the interfacial resistance. For example, the addition of a $LiNbO_3$ layer (2 wt % Li-ion conductive and amorphous) on NCA drastically improves the CE and discharge capacity, reflected in not only lower cathodic charge transfer impedance,[51] but also in stable impedance values over long durations (Figure 13c−e). Similar results were observed for LTO-coated LCO; the cathode resistance decreased from 900 to 20 Ω.[51,82] In addition, the sloping nature at the initial state of charge, indicative of SE decomposition, is reduced, and as a result, there is a dramatic improvement in power density. A schematic of the effects of a coating layer on cathode particles on minimizing chemical and electrochemical reaction at the discharged and charged states was shown in Figure 15a, d, and e. It is important to note that the coating generates two new interfaces: (i) cathode-coating layer and (ii) SE-coating layer.

A suitable coating layer for ASSBs must have the following properties:

(1) Phase stability. The phase stability of coating materials is measured by the E_{hull} (in eV/atom); a lower E_{hull} means the coating is more thermodynamically stable. Figure 17 shows DFT calculations of phase stability for several coating materials.[51,99−101]

(2) Chemical compatibility. Chemical compatibility of coating materials with both the cathode and SE is measured by the decomposition energy in a pseudo binary phase diagram. Figure 17 shows a list of decomposition energies of coating materials (with NCA cathode and LPSCl SE). Typically, the coating materials are oxides due to a negligible or even zero decomposition energy. As shown in Figure 13a (with LPSCl), LiPON, $LiAlO_2$, and Li_2SiO_3 are the most stable whereas LNO, LTO, and LLZO are comparatively less stable.[51] Figure 17 shows the pseudo binary phase diagram of LNO−LPSCl and NCA−LPSCl for different compositions, and the decomposition energy for LNO−LPSCl is lower than for NCA−LPSCl.

(3) Electrochemical stability. A suitable coating material should be electrochemically stable within the operating voltage range of the cathodes. Thus, the transition metal redox band should be well-separated from the oxygen 2p band of the coating layer to avoid redox activity. Unfortunately, most of the oxide-based coating materials are not stable at voltages greater than 4 V versus Li/Li^+ as O^{2-}/O_2 redox will take place.[30,101] Thus, the most promising coating materials are fluorine-based as F^-/F_2 redox happens at very high voltages ($LiAlF_4$ is stable at voltages up to 5.7 ± 0.7 V vs Li^+/Li),[102] which means it can show stable cycling with 4.5 V NMC.

(4) Conductivity. An ionically conductive coating layer enables the transport of Li ions across the coating layer, which improves the rate performance of ASSBs. R_c, the diffusion channel radius (in Å), is an indicator of ionic diffusivity; generally, a larger R_c results in faster diffusion of Li ions through the coating (Figure 13a). $Li_2O−SiO_2$-coated cathodes and $Li_3BO_3−Li_2CO_3$ coated cathodes outperform the single-coated (with SiO_2 and Li_3BO_3) counterparts due to the higher ionic conductivity.[103] The electronic bandgap (E_g, in eV) is related to electronic conductivity; lower bandgap materials usually have high RT electronic conductivity. Highly electronically conductive coatings promote electrochemical decomposition of SEs (especially with sulfides that decompose at very low voltages), which results in increased cathode impedance. Thus, large band gap materials with high Li-ion conductivity are necessary to achieve better performance.

https://dx.doi.org/10.1021/acs.chemrev.0c00101
Chem. Rev. XXXX, XXX, XXX−XXX

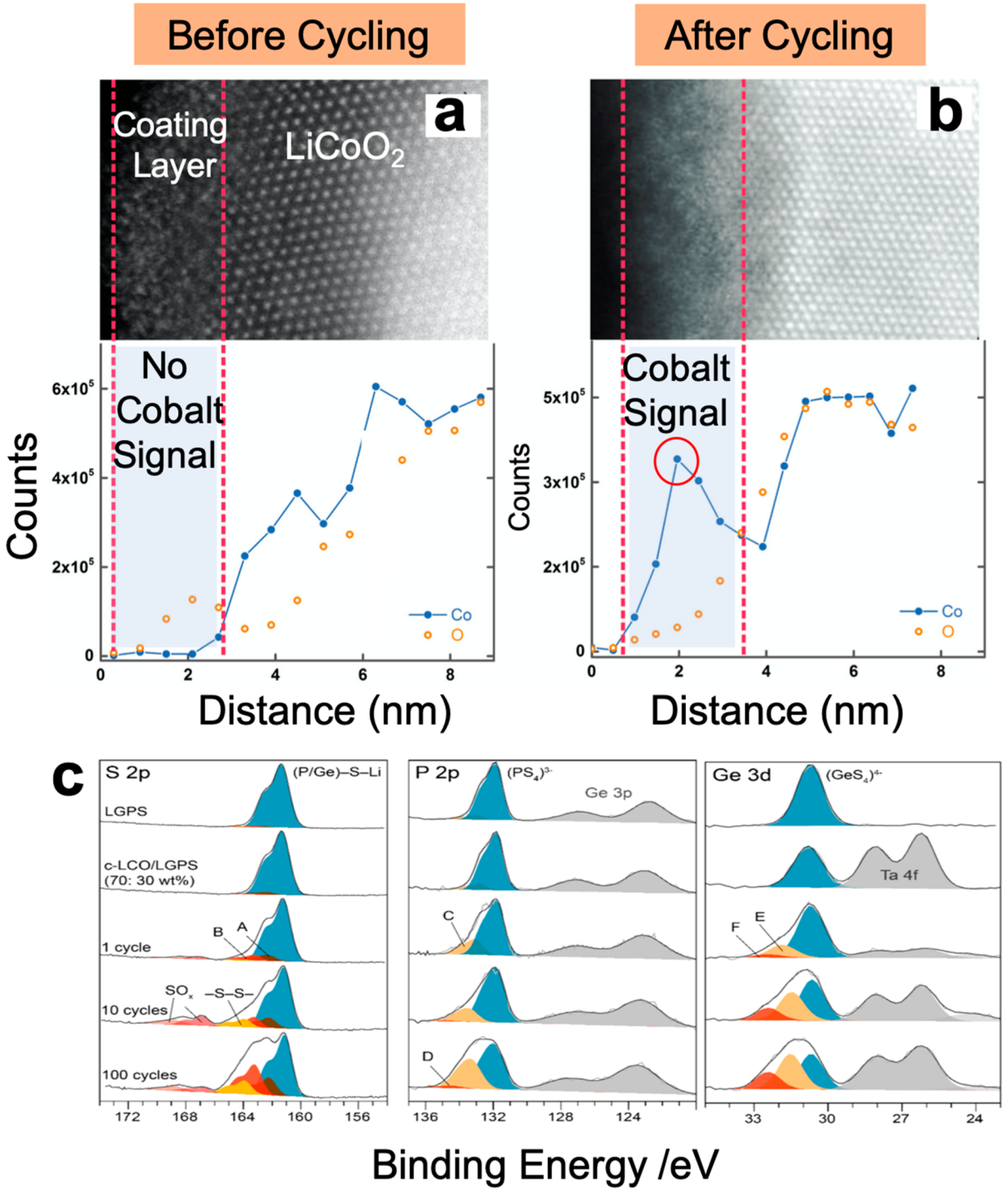

Figure 19. (a) High-resolution HAADF-STEM image of a pristine LNO-coated $LiCoO_2$ particle and (b) cycled (100 cycles) LNO-coated LCO particle ([211] zone axis) with the corresponding EELS line scan (bottom). For the pristine sample, no Co signal is seen in the LNO layer, indicating that no significant Co diffusion from the bulk $LiCoO_2$ into LNO occurs during the coating process. After 100 cycles, significant Co signal is observed in the LNO layer, signifying Co diffusion with cycling. (c) XPS spectra of the S 2p, P 2p, and Ge 3d regions were collected for pristine LGPS, pristine c-$LiCoO_2$/LGPS mixtures (stored for 3 months before measurement), and the cathode material after the first charge, 10th charge, and 100th charge, respectively. The new peaks that arose at higher binding energies indicate the oxidation of LGPS; the peak intensity increases as cycling proceeds, signifying that oxidation continues with cycling. Reproduced with permission from ref 127. Copyright 2018 American Chemical Society.

However, a balance must be struck as poor electronic conductivity of the coating would also block electronic pathways, hindering the rate performance of ASSBs.[99]

(5) Mechanical property. Cathode volume changes will induce strain on the coating layer. Similar to the mechanical property of the electrolyte, the elasticity of the coating layer is important to accommodate the strain, that is, plastic deformation without cracking. Usually a volume change of 10% and 30% (of the cathode) produces 1% and 10% strain, respectively, within the coating layer. LNO, the most common coating, is known for its high stiffness and is expected to form cracks rather

https://dx.doi.org/10.1021/acs.chemrev.0c00101
Chem. Rev. XXXX, XXX, XXX−XXX

than deform plastically.[104−106] Any cracks in the coating will make the cathode come into direct contact with SE, which will facilitate both chemical and electrochemical decomposition of the SE, degrading the battery performance. Amorphous coatings are beneficial as they can more easily deform elastically (compared to crystalline coatings) during the charge−discharge process.

Similar to the sulfide-based SEs, the interface between LCO and oxide-based SEs can be greatly improved by adding a thin coating layer before annealing. For example, interfacial resistance decreased from 2600 Ω/cm^2 to 150 Ω/cm^2 after the addition of a thin Nb layer in between LCO and LLZO.[107,108] In addition, CV on this setup shows sharp oxidation and reduction peaks with low polarization and high rate performance, similar to CV scans with LCO and LE. During heat treatment, Nb oxidizes to amorphous (or at most poorly crystalline) $LiNbO_3$ or $Li_3Nb_4O_6$ via Li diffusion from LLZO to Nb. Amorphous $LiNbO_3$ or $Li_3Nb_4O_6$ is known for its Li ion conductivity (10^{-6} S/cm at RT), which allows the transport of Li without significant resistance. The Nb layer also reduces the interfacial diffusion length from 100 to 20 nm which results in improved rate performance.[107] Another Li-ion conductive layer, Li_3BO_3 (LBO) was employed on LCO which avoids direct contact between LCO and LLZO, preventing chemical diffusion across LCO and LLZO.[109] The addition of LBO improved the capacity and CE from 35 mAh/g and 54% to 80 mAh/g and 84%, respectively. As another example, the addition of NbO_2 lowered the interfacial contact resistance between LATP and LCO by mitigating the irreversible phase change of LCO to Co_3O_4.[110]

The aforementioned coatings are also believed to eliminate the space charge layer. For example, Ohta et al. found that coating $Li_4Ti_5O_{12}$ on LCO reduces the extra slope that originates before charging, which is believed to be due to space charge layer formation.[83] With thiophosphate LPS and a certain thickness of LTO, the slope can be eliminated (Figure 18b).[83] The effect is also realized in impedance measurements and rate performance testing, as reducing this sloping capacity is directly reflected by a lowered LCO/LPS impedance (Figure 18c). However, aside from eliminating the space charge layer, there could be other explanations such as potentially slowed SE decomposition kinetics due to the electronically insulating coating on the LCO cathode (which has relatively higher electronic conduction), and as a result, the oxidation slope region of the SE decreases. However, these interpretations are still based on hypotheses as there is no direct clear evidence for such explanations.

Both binary and ternary coating materials have been applied on cathode materials to protect the interface, such as ZrO_2, Al_2O_3, and SiO_2.[86,111−114] Although they function as a chemically resistive layer, they do not have any ionic charge carriers to aid in interfacial ionic diffusion, so they need to be activated during cycling. In ASSBs, methods to activate the coating layer with charge carriers include: (i) electrochemical lithiation during charge/discharge processes, (ii) diffusion of Li from cathode to the coating layer during heat treatment (when fabricating the electrode), and (iii) surface impurities on the cathode, such as LiOH, Li_3CO_3, and Li_2O could react with coating materials.

Ternary oxides including Li_2SiO_3, $Li_4Ti_5O_{12}$ (LTO), $LiTaO_3$, $LiAlO_2$, Li_2O-ZrO_2, and $LiNbO_3$, are the most commonly used coating materials.[114−122] All of these are chemically and electrochemically stable, yielding better cycling performance with high-voltage cathodes. Although the electrochemical stability of these oxide materials is limited to 4 V, their low electronic conductivity (which leads to sluggish kinetics), may result in long cycle life without any significant capacity decay. LTO, $LiAlO_2$, and Li_2SiO_3 are known for the high ionic mobility of Li ions; Sakuda et al. showed that Li_2SiO_3 works better than SiO_2 (for high discharge capacity), signifying the importance of having charge carriers in the coating layer.[117] Similarly, amorphous LNO, a common coating material, has an ionic conductivity of 10^{-5} S/cm whereas crystalline LNO has an ionic conductivity of 10^{-11} S/cm.

Besides oxides, phosphate-based materials (in the NASICON family) have also been applied as protective coatings since they have high ionic mobility and thermodynamic stability with SEs and cathode materials.[123,124] Another potential type of coating material include halide-based SEs such as Li_3InCl_6 and Li_3YCl_6 since recently they were found to be stable with LCO.[48,125,126] Chloride-based SEs have shown significant electrochemical stability (4.2 V vs Li/Li^+) compared with other oxide-based coating materials. However, considering 5 V cathodes such as Li-rich layered oxides or spinel cathodes, coatings with even higher oxidation stability are required; in this case, fluoride-based SEs may be considered.

4.1.5. Long-Term Cycling Stability of Coating Layer. Without a coating layer, the thickness of a reactive interface layer can increase as cycling proceeds whereas a coated interface would not. This was shown through electrochemical cycling and impedance analysis. For example, a 0.7 wt % ZrO_2-coated NMC cell delivers a capacity of 120 mAh/g with 95% capacity retention while bare NMC exhibits a relatively lower capacity of 110 mAh/g with <30% capacity retention after 50 cycles.[115] Impedance analysis showed that the impedance of bare NMC increases from 600 to 1550 Ω/cm^2 while there is negligible change for the ZrO_2-coated cathodes.

Although coatings can improve cycle life, degradation can still occur, which can be a result of a chemical reaction or mechanical deformation of the coating layer. Even if a coating layer has negligible decomposition energy or sluggish chemical reactivity with SE and cathode, sluggish reactions can be pronounced over time after prolonged cycling. Woo et al. performed HAADF TEM imaging (with EDX line scanning) of LCO (after 33 cycles with LGPS) and found that the distribution of Co at the interface is greatly suppressed (from 35 to 17 nm) by the addition of 45 layers of Al_2O_3 (via ALD), though not completely suppressed.[82] Povey et al. showed that Al in Al_2O_3 diffuses into LCO after prolonged cycling. Additionally, Zhang et al. observed Co in the LNO layer (after 100 cycles) by EELS line scan (Figure 19a,b).[127] Co migration degrades LCO and the performance of the ASSB by making a local LCO interface with a Co-deficient phase. Similar observations were noticed by XPS, where new peaks appeared after 100 cycles belonging to Co−S, polysulfides ($-S^0-$), sulfite, and sulfate species for the LNO-coated LCO sample (Figure 19c).[127] Other evidence also demonstrates the continuous degradation of the coating layer and the formation of byproducts, though notably to a lesser degree than uncoated samples.[128]

One possible explanation for the continued CEI growth over prolonged cycling is based on the mechanical behavior of the coating layer and the CEI during volume changes associated with the formation of the CEI and cathode materials. Negative volume changes would generate voids at the interface whereas positive volume changes would induce stress into the electrodes. In addition, there is periodic stress with cycling, due to reversible

https://dx.doi.org/10.1021/acs.chemrev.0c00101
Chem. Rev. XXXX, XXX, XXX−XXX

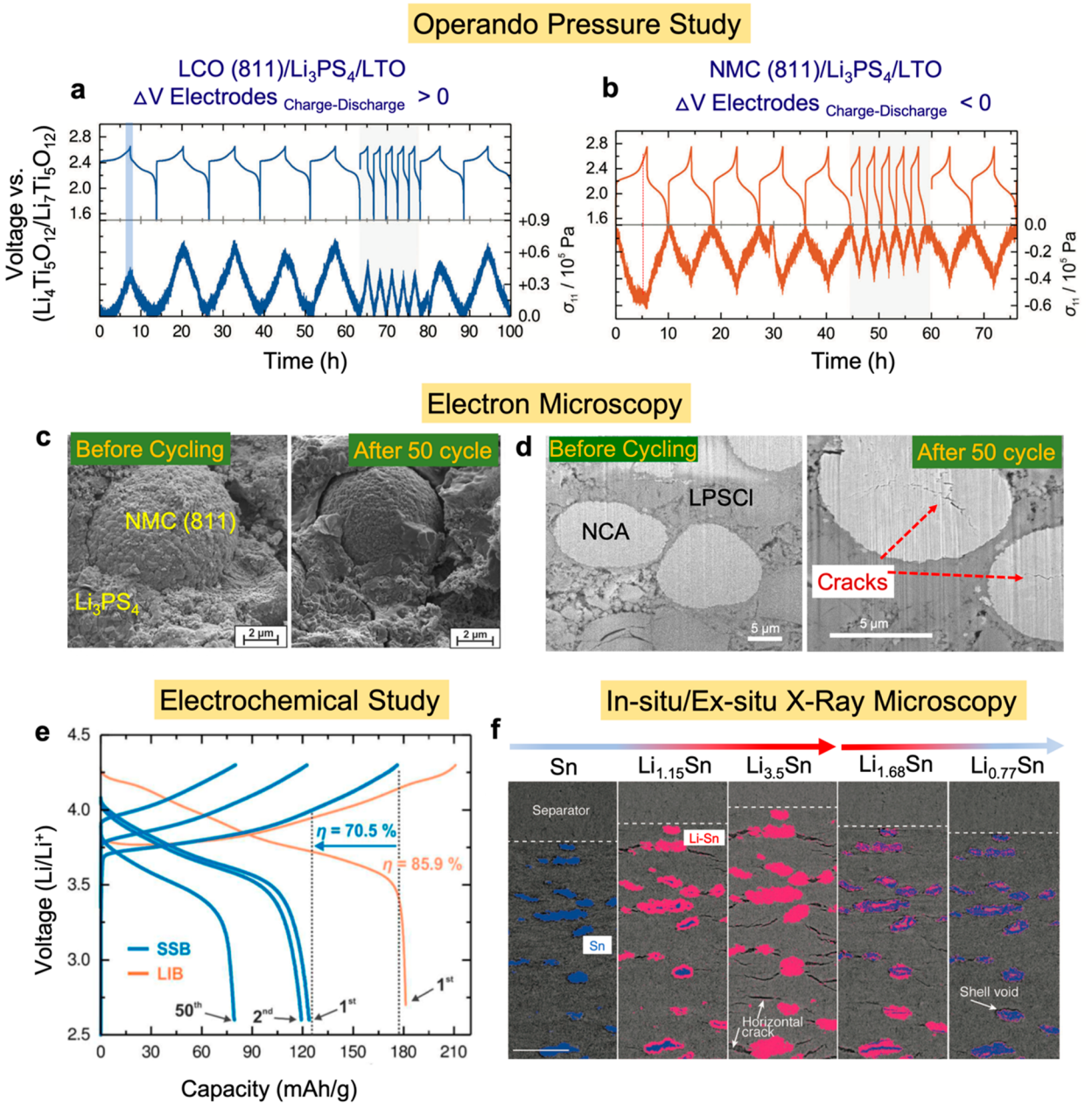

Figure 20. Schematic of mechanical changes that occur after ASSB cycling. (a) Operando monitoring of pressure change in ASSBs during charge/discharge and the corresponding pressure change for (a) LCO and (b) NMC811, where a positive volume change (expansion) and increase in pressure was noticed for LCO and a negative volume change (contraction) and decrease in pressure was noticed for NMC811. Reproduced with permission from ref 145. Copyright 2018 The Royal Society of Chemistry. (c) SEM image of the NMC811−Li_3PS_4 interface before cycling. Reproduced with permission from ref 75. Copyright 2017 American Chemical Society. (d) SEM images of focused ion beam-milled cross section of NCA and Li_6PS_5Cl interface before and after 50 cycles where intramolecular cracks were observed. (e) Observed low first cycle CE of a NMC−Li_3PS_4 ASSB, compared with carbonate-based LE. Reproduced with permission from ref 76. Copyright 2017 American Chemical Society. (f) Nano-CT of Sn anode cycling with glassy LPS SE and CT of the full solid-state pellet before and after cycling. Reproduced with permission from ref 148. Copyright 2019 Wiley-VCH Verlag.

volume changes of the cathode during lithiation and delithiation. Such stresses and voids may result in cracks, which can deform and expose the fresh SE to the cathode surface. This will initiate chemical and electrochemical decomposition and further increase the cathodic charge transfer resistance.

4.2. Mechanical Properties of SE

The mechanical properties of the SE are crucial with regards to the fabrication and performance of ASSBs. For example, electrode composites in ASSBs undergo high-temperature heat treatment or experience external pressure which deforms the electrode materials. However, the SE does not undergo volume change during cycling unless it participates in chemical or electrochemical decomposition. Lithiation/delithiation-induced phase transition, accompanied by volume change, leads to internal and external stress in the electrode and electrolyte. Such stress generates microcracks, lattice dislocations, and defects in the electrode as well as the electrode−SE interface. The extent of volume change of electrodes depends on the constituent phases and the operating voltage; intercalation materials undergo less

https://dx.doi.org/10.1021/acs.chemrev.0c00101
Chem. Rev. XXXX, XXX, XXX−XXX

volume change (less than 10%) whereas conversion or alloying electrodes experience significant volume change (50−400%) during cycling.[129−132] Thus, mechanical compatibility in alloying/conversion materials is of significant importance.[133,134]

Deformability is an essential aspect as it directly translates to the ability of the SEs to be densified. Typically, oxide-based SEs are very stiff and need high-temperature annealing to reduce the number of grain boundaries.[14] High-temperature annealing is energy intensive and not cost-effective; in addition, as stated before, it may cause undesirable side reactions with electrode materials. On the other hand, glass or ceramic sulfide-based SEs are more malleable and thus can be densified at RT by simple cold-pressing. From a mechanical and processing perspective, this makes them more promising in terms of generating a favorable interface with electrode materials.

The mechanism behind densification of SEs involves the diffusion of atoms and polyhedra; fast diffusion helps to easily merge grain boundaries. For Li_2S:P_2S_5-based SEs, Li-ions and PS_4^{3-} polyhedra can diffuse along the grain boundaries and fill the voids between the particles (provided that pressure is applied). This diffusion capability is based on the bond species and bond strength within the SE structure. Oxide-based glassy SEs (75% Li_2O:25% P_2O_5) are 2 orders of magnitude less deformable compared with the analogous sulfide glass (75% Li_2S:25% P_2S_5), due to the higher bond strength of Li−O and P−O bonds compared to Li−S and P−S bonds.[135,136] It is very interesting to note that the $75Na_2S{:}25P_2S_5$ glass has better deformability than $75Li_2S{:}25P_2S_5$; due to the larger size of the Na ion compared with Li, the interactions between Na^+ and PS_4^{3-} are weaker, leading to faster diffusion of PS_4^{3-} into the particle boundaries.[137] In general, materials having weak bond energies usually have lower glass transition temperatures and melting points. As Li_2S content increases in the Li_2S:P_2S_5 glass, the deformability decreases, shifting the glass transition temperature to a higher value, indicative of an increase in internal bond energy (Li_2S has an ionic bond nature while P_2S_5 is covalent).[136] Increasing the ionic nature of the electrolyte increases the bond energy which makes it stiffer, and as a result, the degrees of translational and rotational motion in the crystal are reduced. The deformability of SEs also depends on the crystallinity of the materials; a glassy structure has a high molar volume with isolated structures which helps for better diffusion and densification.

Another important property is the elastic modulus since volume changes occur during the charge−discharge process in ASSBs; repeated structural and volume changes experienced by electrodes during cycling can induce mechanical stress on SEs. If a SE has a high Young's Modulus, the SE cannot readily accommodate the induced stress and as a result, cracks can form at the interface. These cracks will lead to the increased interfacial contact resistance due to the reduced contact area between the electrode and electrolyte, which will slow reaction kinetics, lower the CE, and hinder rate performance. Typically, the Young's modulus of sulfide-based SEs is 18−25 GPa (1 order of magnitude lower than oxide-based SEs, 160−180 GPa). Such values can allow the SE to easily accommodate the stresses induced from cathode volume changes.[130,137−140]

The Young's modulus of the SE depends on its composition. As mentioned previously, increasing Li_2S content in Li_2S:P_2S_5 glasses increases the ionic bonding property of the SE, which in turn increases the Young's modulus (but will compromise the ionic conductivity).[140] It is important to note that these two are not always opposing effects; halide incorporation into LPS glass can reduce the Young's modulus of LPS while synergistically enhancing the ionic conductivity. The incorporation of iodine lowers the bond strength without changing the local coordination environment of PS_4, which translates into a lowered glass transition temperature and Young's modulus. Kato et al. showed that a ASSB with a Si anode and $70{-}(0.5Li_2S{:}0.5P_2S_5){:}30LiI$ glass SE exhibited 10% higher capacity, higher first cycle CE and better cyclic stability over 20 cycles than with $75Li_2S{:}25P_2S_5$ glass, even though they possess similar ionic conductivity (2.2×10^{-4} S/cm). The addition of LiI led to a decrease in the Young's modulus (of $Li_2S{-}P_2S_5$ glass) from 23 to 19 GPa resulting in better deformability and thus increased stress accommodation, enabling longer cycling.[140−142]

During cycling, dynamic stresses/strain leading to the formation of cracks/voids inside electrodes, SE, and electrode−SE interface are difficult to study quantitatively due to the buried nature of the interface. Koerver et al. showed that uncoated NMC-based ASSBs (with β-Li_3PS_4 SE) had a low first cycle CE of 70.5% compared with LE (85.9%) (Figure 20g). The low CE originates from chemical/electrochemical reactions occurring at the cathode−SE interface along with contact loss between the cathode and electrolyte during the first cycle.[75] Yu et al. demonstrated that merely retightening the cell cannot recover the capacity due to permanent delamination and contact loss between the cathode particles and SE.[143]

Koerver et al. correlated the volume change of active materials with different applied pressure using operando pressure monitoring of ASSBs.[144] By selecting particular anode or cathode materials, the degree of volume change can be measured and compared. For example, when LTO was used as an anode, which experiences almost zero volume change and induces minimal stress, any pressure changes can thus only originate from the volume change of cathode particles.[144] For example, cells with a LCO cathode and LTO anode experienced significant stress (+0.6 MPa) because the unit cell volume increases for LCO upon delithation. The reverse trend happens for the NMC/LTP-based ASSB as NMC811 shrinks during charging. Fortunately, the stress is relieved and reverts to the original state during discharging, which is beneficial for long-term cycling of the ASSBs. However, long-term cycling can still produce interfacial gaps between the cathode and SE (NMC/LPS, Figure 20c,d), which irreversibly increases interfacial charge transfer resistance and yields poor cycle life. In addition to the electrode material selection, operating stack pressure of ASSBs affects the performance during volume change.[144] Koerver et al. demonstrated an ASSB comprising of LCO and In metal (both of them have positive volume change) with a poor capacity of 11.4 mAh/g, a low first cycle CE of 77.4% (usually close to 90%), and low cyclic performance when no stack pressure was applied.[145] As seen by X-ray tomography, bending generated cracks at the edge of the charged (non-pressurized) ASSB, revealing the importance of external confinement (which evenly distributes pressure), to maintain the contact required for ionic and electrical conductivity between particles.[146,147]

X-ray tomography is a nondestructive and useful technique to observe *in situ* and *ex situ* changes in ASSBs. Wu et al. studied operando lithiation/delithiation dynamics of Sn particles with LPS SE including interfacial crack formation and propagation.[148] The difference in X-ray attenuation (due to different densities) helped to distinguish between Sn, lithiated Sn, LPS, and voids/cracks (Figure 20f). Using this technique, they made a few observations: (i) anisotropic expansion and contraction

https://dx.doi.org/10.1021/acs.chemrev.0c00101
Chem. Rev. XXXX, XXX, XXX−XXX

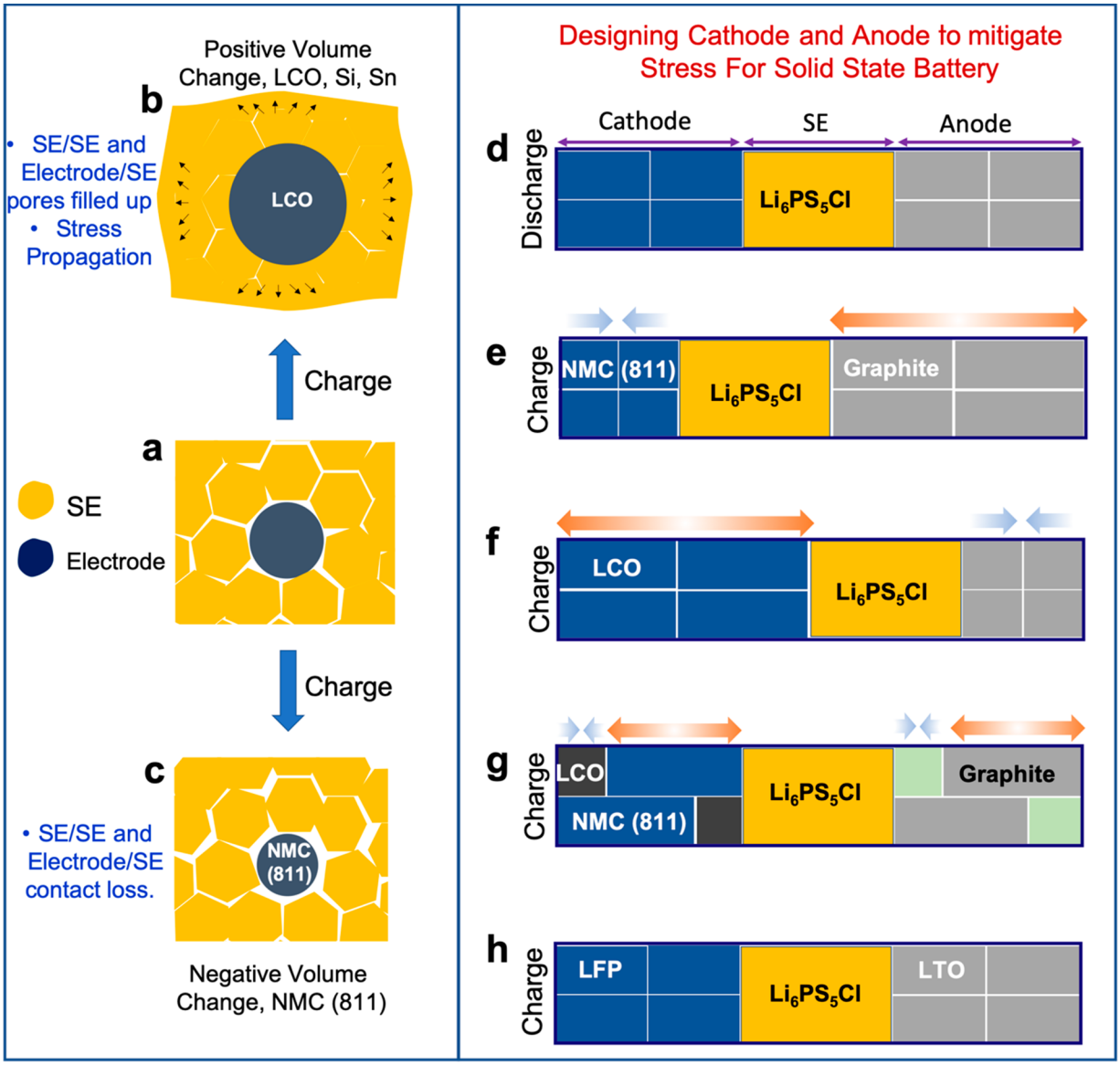

Figure 21. Schematic of mechanical changes that occur after ASSB cycling. (a) An electrode-SE interface develops if the SE is not fully dense and the electrode is not conformally covered with SE after cold pressing. (b) cathodes that experience positive volume change, such as LCO (up to 4.4 V), expand during charge which can fill cathode−SE and SE−SE gaps (reducing porosity), which induces stress into the SE that can possibly propagate through to the anode. (c) A negative volume change material such as NMC shrinks during charging which generates more gaps and increases electrode porosity. (d) A typical ASSB with cathode, anode, and SE at the discharged state. (e) An ASSB constructed where $\triangle V_{Cathode} < 0$, $\triangle V_{Anode} > 0$; the negative volume change of NMC is compensated by positive volume change of anode. (f) $\triangle V_{Cathode} > 0$, $\triangle V_{Anode} < 0$ where the positive volume change of LCO is compensated by the negative volume change of anode (g) $\triangle V_{Cathode\text{-}I} > 0$, $\triangle V_{Cathode\text{-}II} < 0$ $\triangle V_{Anode\text{-}I} < 0$, $\triangle V_{Anode\text{-}II} > 0$, a combination of cathodes (and anodes) where positive volume change of one cathode (anode) is compensated with one negative volume change of another cathode (anode). (h) Cathode and anode materials with negligible or no volume change after charging.

happens during lithiation and delithiation of Sn and some lithiated Sn becomes electrochemically disconnected, meaning it can no longer participate in the redox process, (ii) there is preferential interfacial crack formation and propagation through the bulk of the LPS SE which could be due to more compressive stresses at the interface, (iii) permanent cracks are present at the Sn−LPS interface after full delithiation which explains the low first cycle CE and poor capacity retention, and (iv) cracks in LPS that originate from volume expansion of Sn particles almost completely disappear after full delithiation, which could be due to the adequate elasticity of LPS to accommodate the volume change (8%) of the working composite electrode.[149]

Thus, the choice of cathode and anode materials for accommodating the mechanical stress created during cycling is essential for good ASSB cycling performance. The detailed schematic was shown in Figure 20a−c. In summary, there are a few possible ways to accommodate the induced stress such as (1) using a soft polymeric binder as a buffer material, (2) using a negative volume change material as the cathode and a positive volume change material as the anode (e.g., NMC811 as the cathode and graphite as the anode) and vice versa (Figure 21d−f), (3) using combinations of cathodes (or anodes) with both positive and negative volume change where the total positive volume change is compensated by equal total negative volume

https://dx.doi.org/10.1021/acs.chemrev.0c00101
Chem. Rev. XXXX, XXX, XXX−XXX

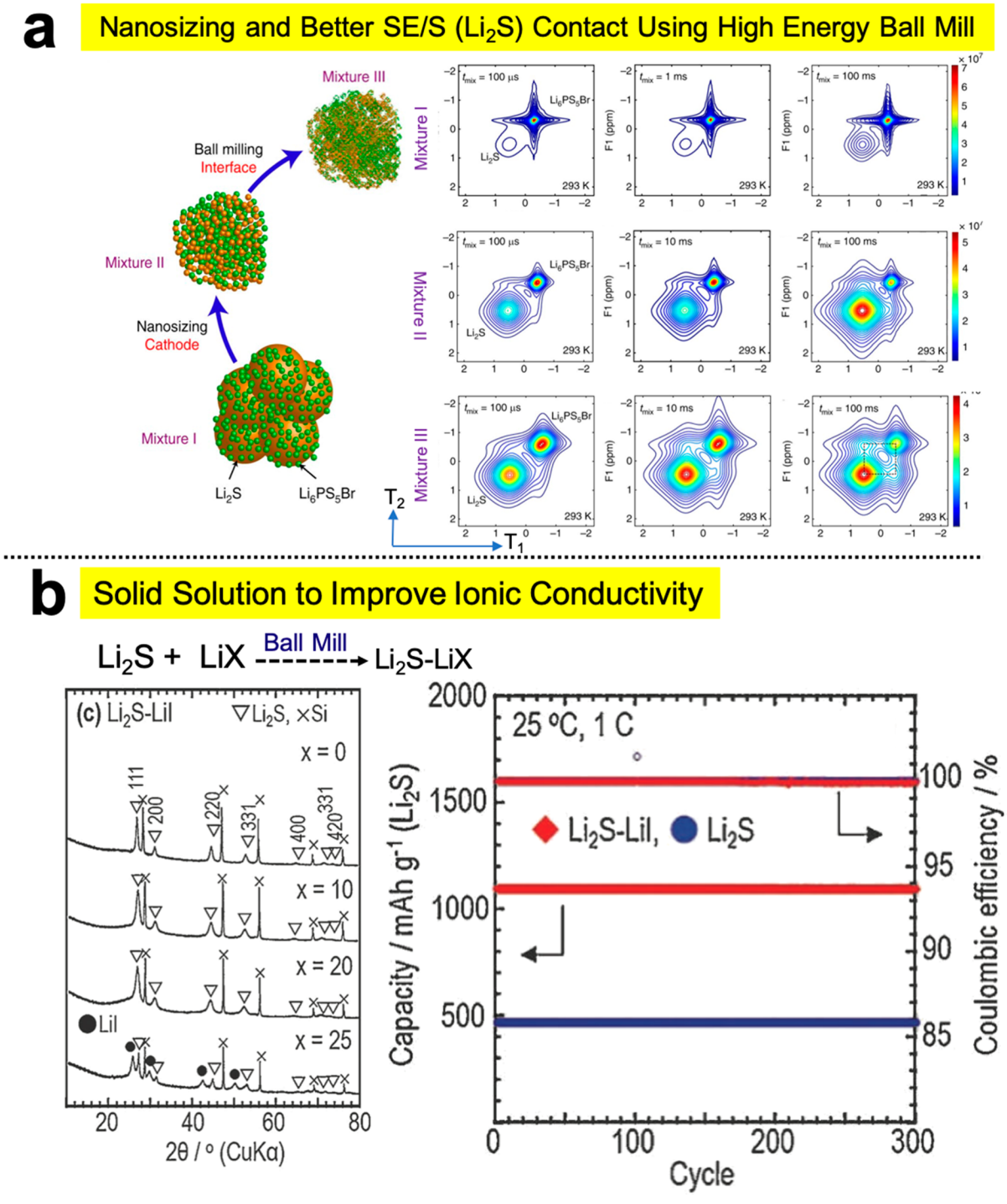

Figure 22. (a) Li_2S−Li_6PS_5Br composites were made by high-energy ball milling. Solid-state two-dimensional (2D) ^7Li−^7Li exchange spectra (2D-EXSY) measured at a ^7Li resonance frequency of 155.506 MHz with a spinning speed of 20 kHz for short (100 μs) to long mixing times (100 ms) at RT for different mixtures. Off-diagonal cross-peak intensity was observed only for mixtures III at t_{mix} = 10 ms, was most pronounced at t_{mix} = 100 ms, and represents Li-ion exchange from Li_2S to Li_6PS_5Br and vice versa.[171] (b) Ball-milling synthesis of a Li_2S−LiI solid solution and an all-solid-state Li−S battery operating at 25 °C with this Li_2S−LiI solid solution. Reproduced with permission from ref 174. Copyright 2015 Wiley-VCH Verlag.

change (Figure 21g), and (4) using electrodes with minimal or no volume change such as LTO or NMC532 (Figure 21h).

The mechanical properties of the SEI/CEI also have a large impact on ASSB cycling performance. The net volume change after formation of the SEI/CEI influences the interface structure. For example, NPS exhibits net positive volume change with Ni, Mn, and Co-based layered oxides, but has large negative volume change with Fe-based polyanionic cathodes such as $NaFePO_4$ and $NaFePO_4F$.[76] Positive volume change creates additional stress on the cathode particles and SE whereas negative volume change is expected to generate voids at the interface (Figure 12).[76] The mechanical properties of the CEI/SEI depend on their morphology, microstructure, and chemical composition. Currently, characterization to both qualitatively and quantitatively evaluate the mechanical properties of the CEI/SEI have not been carried out. This is because isolating such an interface is

https://dx.doi.org/10.1021/acs.chemrev.0c00101
Chem. Rev. XXXX, XXX, XXX−XXX

nontrivial. While *in situ* techniques are extensively used for LE battery interface characterization, applying such techniques in ASSBs is complex, and new, innovative approaches are needed to successfully carry out such characterization.

Finite element modeling was also employed to investigate the mechanical behavior at the interfaces.[150,151] Kinetic Monte Carlo was employed by Mukherjee et al. where they found that high-surface-area cathode particles reduce compressive stresses within the particles during lithiation and enhance electronic conduction pathways.[152−154] This result is good agreement with experimental observations by Strauss et al. where NMC with a smaller particle size exhibited better electrochemical performance than larger particles. Bucci et al. employed a cohesive zone model to simulate the damage evolution of cathode composites; fracture was prevented when the expansion of electrode particles is lower than 7.5% (on par for most Li-intercalating compounds) and the solid electrolyte's fracture energy is higher than 4 J/m^2.[150] These results indicate that although sulfide-based SEs are easily deformed to accommodate the volume change of the cathode, their low fracture energy (2.8 ± 1.8 J/m^2 for LPS glass) makes crack formation and propagation easier than oxide-based SEs. The results also indicate that alloying materials with high volume expansion (>50%) are suspected to generate more cracks than intercalation-based oxide cathodes.

4.3. SE−S (Li_2S) Interface

A Li−S battery comprising a Li-metal anode and S cathode is regarded as one of the most promising next-generation battery technologies as it consists of materials that are earth abundant, low cost, environmentally friendly, and can achieve a high theoretical specific capacity (1675 mAh/g). However, the Li−S battery system suffers from polysulfide (Li_2S_n, n = 3−8) dissolution and shuttling in conventional LEs, result in a lower energy efficiency and limited cycle life.[155,156] All-solid-state Li−S batteries are believed to eliminate the Li-polysulfide redox shuttle problem that has plagued conventional liquid Li−S battery systems for the past few decades. Additionally, passivating interfaces formed between SEs and metallic Li prevents continuous SEI formation which is the cause of the eventual consumption and depletion of LEs in conventional Li−S chemistries.[157−159]

There are four key challenges for all-solid-state Li−S batteries (Figure 17): (i) poor kinetics, (ii) low cathode capacity and utilization, (iii) low active loading in cathode composites, and (iv) Li metal dendrite growth.[160,161] Most of these problems are associated with interfacial charge (both ion and electron) transfer kinetics of S (or Li_2S) and SE. Compared with layered oxide cathodes, S/Li_2S cathodes have their own advantages and disadvantages. For example, Ceder et al. showed zero reaction energy between Li_2S and all of the sulfide-based SEs, making an extra protective coating layer unnecessary. Additionally, a nonreactive S−SE interface allows relatively more harsh processing conditions (brought upon by high-energy ball milling or high-temperature treatment) to make the cathode composite mixture (these methods are not recommended for layered cathodes). However, the S cathode experiences 80% volume expansion after full lithiation (<10% for layered oxide cathodes),[162−164] resulting in stress/strain generation, contact loss, low CE, low utilization of materials, and poor cyclic performance. Moreover, the S cathode is known for its very poor electronic and ionic conductivity (several orders of magnitude less than conventional oxide cathodes). Hence, large amounts of carbon and SE are required to synthesize cathode composites, which compromises the active material weight percentage and areal loading capacity. Multiple synthesis methods were explored to engineer the interface to gain new fundamental knowledge of the interface to enable performance improvements in ASSBs.

One suitable method to mitigate the interfacial issue is to reduce the particle size of S, Li_2S, and the SE by using high-energy ball milling, which will enhance the contact area between S/SE and S/carbon, decrease the diffusion length of Li, and improve charge transfer dynamics at the interface. To this end, Choi et al. compared three kinds of S, conductive carbon, and Li_2S−P_2S_5 composites made by hand mixing (using a mortar and pestle), ball milling, and secondary high-energy ball milling, respectively.[161,165−167] Secondary high-energy ball milled composites had the smallest particle size and the highest utilization of S cathode. Nagao et al. and Tatsumisago et al. performed ball milling at 155 °C where S (low-viscosity) mills into an ultrasmall particle size (<50 nm) and achieved a high capacity (1200 mAh/g) with full capacity retention after 40 cycles.[168,169] Suzuki et al. synthesized the S cathode in a liquid phase which increased the capacity to 2000 mAh/g and the cell had 75% capacity retention after 50 cycles.[72] Ultrafine particles (1−10 nm) of S (used to decorate SEs and carbon) was also made by a gas phase reaction followed by mechanical milling.[170] Furthermore, Yu et al. compared the spontaneous Li-ion transport across the Li_2S−Li_6PS_5Br interface (made by different milling conditions) by two-dimensional (2D) Li-ion exchange NMR (Figure 22a).[171] Their results show that ball milling is necessary to achieve faster Li-ion exchange across the interface and improve the kinetics for high utilization of Li_2S cathode. However, Li-ion interfacial charge transfer resistance increases from 1.5 Ω to 65 Ω after cycling due to contact loss, a result from high volumetric expansion/contraction during the charge and discharge processes.[171,172]

Hakari et al. developed Li_2S-LiX (X = Cl, Br, and I) solid solutions using high-energy ball milling which improved the ionic conductivity of the Li_2S electrode 2-fold.[173,174] The solid-solution composite with Li_2S:LiI (80:20 mol %) exhibited the maximum capacity of >1100 mAh/g (95% of theoretical capacity) at 0.5 C with extremely high rate performance (100% capacity retention after 2000 cycles at 2 C) (Figure 22b). Solution-based synthesis is also an effective way to improve the interfacial contact between SE and S.[175,176] Liang et al. made S-rich Li-polysulfidophosphate (Li_3PS_{4+n}) by dissolving Li_3PS_4 and S in tetrahydrofuran at RT.[177] The obtained polysulfidophosphate exhibited an ionic conductivity of 3×10^{-5} S/cm at RT, which is much higher than the pristine S/Li_3PS_4 mixture. The all-solid-state Li−S battery with the polysulfidophosphate SE had a capacity of 1272 mAh/g at 0.1 C and 100% capacity retention after 300 cycles. When the operating temperature was increased to 60 °C, the capacity was further increased to 1400 mAh/g along with extended cyclic stability.

Hayashi et al. added Cu metal into S cathode and improved the interfacial contact resistance;[160,178] the key reason for improvement is that Cu reacts with S to form the electrochemically active CuS, enabling better cycling. Additionally, Cu can help to improve the electronic conductivity at the interface for faster redox kinetics. ASSBs with the S−Cu cathode composite (with $80Li_2S$:$20P_2S_5$ glass-ceramic SE) showed excellent reversible capacity of ∼650 mAh/g (based on the weight of S and at a current density of 64 μA/cm^2) for up to 20 cycles.

In summary, the bottleneck of the all-solid-state Li−S battery is the high charge transfer resistance of the S−SE interface,

https://dx.doi.org/10.1021/acs.chemrev.0c00101
Chem. Rev. XXXX, XXX, XXX−XXX

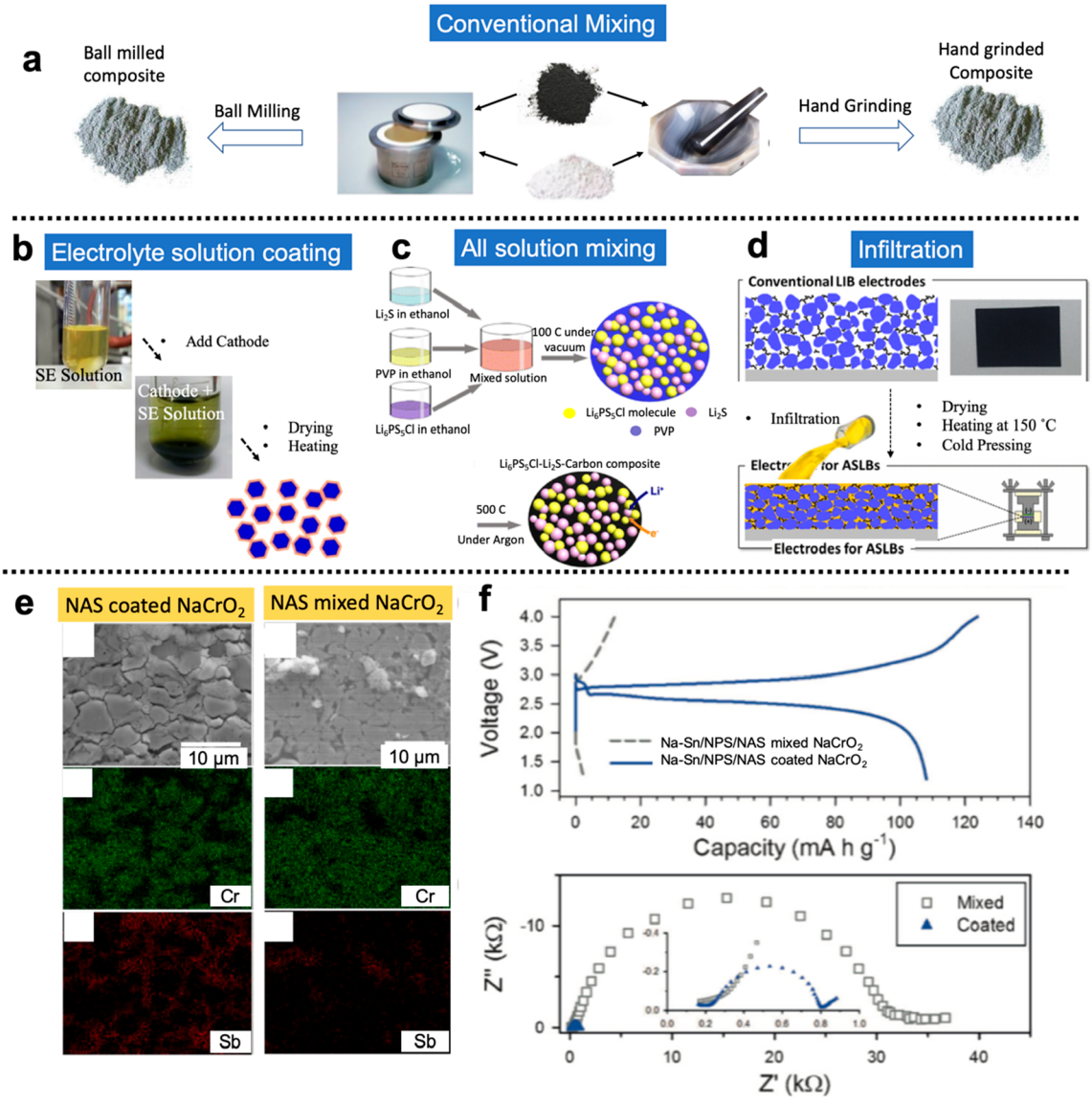

Figure 23. (a) Conventional process to make cathode composites by mixing the cathode and SE either by hand grinding with a mortar and pestle (top right) or ball milling (top left), (b) Schematic of the solution-processed conformal coating of SE on cathode particles. Reproduced with permission from ref 183. 2016 Wiley-VCH Verlag. (c) Schematic diagram of dissolving SE, cathode, and polymer all together to synthesize cathode-SE-carbon composite. Reproduced with permission from ref 176. Copyright 2016 American Chemical Society. (d) Schematic illustrating the infiltration of conventional LIB composite electrodes with solution-processable SEs. Reproduced with permission from ref 204. Copyright 2017 American Chemical Society. (e) FIB-milled cross sectional SEM images of NAS-coated and hand-mixed $NaCrO_2$, Cr (from cathode) and Sb (from SE) EDX images of coated and mixed electrode, respectively, where a more homogeneous and conformal distribution of SE is found for the coated electrode. (f) Charge–discharge profile and Nyquist plot for the coated and mixed electrode. Reproduced with permission from ref 188. Copyright 2016 Wiley-VCH Verlag.

which is highly dependent on the synthesis method of the SE. Although tremendous progress has been made over the last few decades, most of the literature reports high capacity and good cyclic retention only with relatively low areal loading. To achieve the goal of 4 mAh/cm^2 capacity for a > 400 Wh/kg energy-density battery pack, a fundamental understanding of interfacial charge transfer along with novel synthesis methods are paramount to improve the contact between SE-S and S-carbon.

4.4. Conformal Interface

For a practical high-energy ASSB, the SE amount used in ASSBs should be as low as possible since they are electrochemically inactive materials. Conventional hand mixing is insufficient to achieve intimate conformal contact between the electrode and SE particles. Although ball milling is much better for mixing, it can sometimes cause a chemical reaction between materials. To guarantee intimate contact between the SE and electrode materials, a high weight (or volume) percentage of SE is used in the composite, which limits the kinetics and reduces the pack/cell-level energy density. Unfortunately, synthesis, processability, and environmental sensitivity of most SEs means this issue is not easily overcome.[179]

One strategy to achieve a conformal cathode–SE interface with a low percentage of SE is by using PLD to deposit the SE onto the cathode surface.[180−182] However, the cost and vacuum requirement of PLD limits its application for large-scale processability of ASSBs. Alternatively, Jung et al. implemented a solution process to coat the SE onto the cathode by first dissolving the SE in a solvent followed by the addition of cathode materials (Figure 23b).[183] The method was applied to

https://dx.doi.org/10.1021/acs.chemrev.0c00101
Chem. Rev. XXXX, XXX, XXX−XXX

Li_4SnS_4:LiI SE; drying at 200 °C resulted in a less-crystalline material with better deformability and higher conductivity compared to the crystalline phase produced during high-temperature processing.[183,184] The major advantages of the solution-processed Li_4SnS_4:LiI SE coating are (i) the coated electrode had a lower porosity (7%) compared to conventional hand-mixed cathodes (12%), (ii) the surface coverage of the solution-coated $LiCoO_2$ electrode (81%) is 2.6-times higher than that of the hand-mixed electrode (31%), and (iii) the cathode charge transfer impedance is reduced by half in the case of the coated electrode, improving the kinetics (the coated electrode showed 83.3% of theoretical capacity at 1 C, whereas a conventional mixing process showed only 46.0%. Similar observations were made for the Na-based sulfide superionic conductor Na_3SbS_4.[185−188] A solution-processed conformal coating of Na_3SbS_4 (10^{-3} S/cm at RT) on $NaCrO_2$ delivered the theoretical capacity of $NaCrO_2$ at 0.1 C whereas conventional hand mixing showed negligible capacity. Furthermore, the difference between hand mixing and solution processing is reflected by an order of magnitude difference in the cathodic charge transfer resistance (Figure 23f).[188] Figure 23e shows the FIB-milled SEM cross-sectional images of NAS-coated and NAS-mixed $NaCrO_2$. NAS was found to homogeneously coat the $NaCrO_2$ with EDX (Cr and Sb), whereas segregation of NAS (and thus nonuniform mixing) was found for the hand-mixed electrode.

Solution-processed SE coatings on cathodes are not limited to SEs containing Sn and Sb.[189−191] LPSCl has been used as a solution-processed (ethanol-based) coating on cathode particles with moderate ionic conductivity (10^{-4} S/cm at RT).[192−195] Furthermore, high-temperature treatment (550 °C) raises the conductivity back to the theoretical value (10^{-3} S/cm).[195,196] However, high-temperature treatment can promote chemical reactions, so optimization of the heating temperature is necessary to achieve high conductivity without compromising the chemical stability of the interface and dependent rate performance of the ASSB. Ethanol-processed LPSCl coatings were applied to various cathode materials (LCO, NMC, and NCA)[193] where significant improvements in rate performance were noticed compared with conventional mixing processes.

However, one limitation of solution processing is the difficulty with incorporating carbon as a conductive additive, since most carbon materials are insoluble. Han et al. modified the coating process by using PVP as the carbon source (along with Li_2S cathode and LPSCl dissolved in ethanol) followed by drying (Figure 23c).[176] PVP is carbonized after heating to a relatively low temperature (300 °C), ensuring a homogeneous coating and distribution of Li_2S, carbon, and LPSCl, resulting in a reversible capacity of 830 mAh/g (71% utilization of Li_2S; at 50 mA/g for 60 cycles at RT even at a high Li_2S loading of ∼3.6 mg/cm^2), much greater than that achieved by conventional hand-mixed processing.[176] Such *in situ* synthesis of other sulfide-based SEs (together with the cathode material) was also applied for several transition metal sulfides such as Co_9S_8, Fe_3S_4, $Fe_{1-x}S$, and MoS_2. This type of process is primarily applied for metal sulfides rather than oxide cathodes because metal sulfides have lower thermodynamic reaction energies than oxides.[197−202] Another advantage of solution processing is the ability to stabilize highly ionically conductive metastable phases at relatively low temperatures, such as β-Li_3PS_4 (1.6×10^{-4} S/cm at RT).[203]

The solution process was further modified by Jung et al. as they used the conventional casting process (cathode on aluminum foil, outside the glovebox). This was followed by the addition of LPSCl solution in inert conditions. The solution infiltrated into the composite to form a homogeneous coating. Subsequent cold-pressing resulted in a uniform coating, ultimately not only reducing the SE wt %, but also improving the kinetics of charge transfer (Figure 23d).[204,205] The LPSCl-infiltrated $LiCoO_2$ and graphite electrodes exhibited capacities of 141 and 364 mAh/g, respectively, at 0.1 C and 30 °C, which are much higher than the values achieved with conventional dry-mixed and slurry-mixed electrodes.[204]

Very recently, a dry impact-blending process (known as "hybridizing") was used for conformal coatings; NCM cathode and Na_2SO_4 SE were used as the model compounds.[206] SEM images show the conformal coating of Na_2SO_4 on NCM, and cross-sectional SEM images reveal a continuous and homogeneous coating with evenly distributed NCM and Na_2SO_4 throughout the electrode. The advantages of this process are as follows: it does not use a solvent (which could possibly be toxic if methanol or hydrazine are used), it is a simpler process which makes it more cost-effective, and it is material-independent (can be used with any SE or cathode). However, this process still needs to be further evaluated via electrochemical cell performance and by using a highly conductive solid electrolyte.

Sun at al. synthesized Li_3InCl_6 (with a high ionic conductivity of 10^{-3} S/cm) by dissolving LiCl and $InCl_3$ into water followed by heat-treating at 200 °C.[125] Such a process shows that halides can be easily applied as conformal coatings on cathode materials. Chloride-based SEs could be very effective in the future considering their ease of processability, low cost, and low toxicity. Moreover, chloride-based SEs are stable in air[126] and do not require an additional protective coating layer when using certain oxide cathodes (see Figure 24).[48]

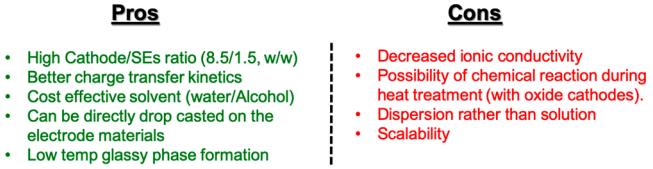

Figure 24. Pros and cons of solution-processed coating methods.

4.5. Hybrid Interface

Although a solution-processed coating decreases the electrode−SE charge transfer resistance, the rate performance of ASSBs is still limited compared to LE, mainly due to an atomically nonwetted interface. A wetted interface is only possible through the chemical reaction between two solid surfaces, but such a chemical reaction contributes additional interfacial impedance and thus does not enable good cycling performance. Additionally, the incorporation of binder and conductive carbon also blocks Li-ion transfer across the interface (Figure 25a). There are three possible effective strategies to mitigate such a problem by using additional ion-conducting substances.

1. Adding a few drops of LE is a very effective way to wet the SE−cathode interface, as the LE fills all the gaps for better ionic charge transfer across the interface. It was found that LE is almost essential to wet the LLZO−LCO interface for ASSB cycling, as there is a high surface energy mismatch between layered LCO and LLZO. Additionally, LLZO cannot be solution-processed at low temperatures to achieve a conformal coating.[207] Although it is believed that all LEs are stable with LLZO, sulfide-based SEs are

https://dx.doi.org/10.1021/acs.chemrev.0c00101
Chem. Rev. XXXX, XXX, XXX−XXX

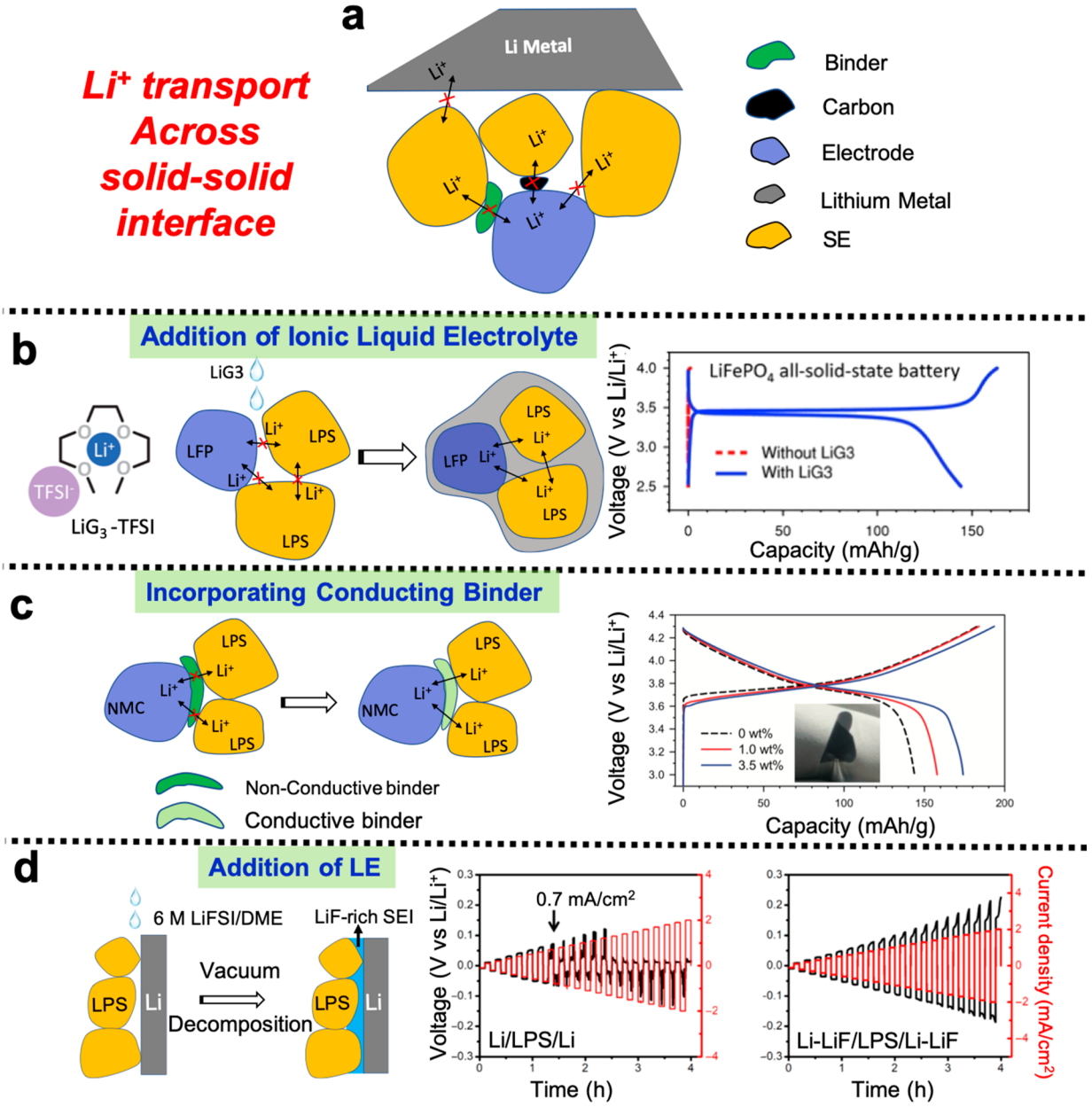

Figure 25. (a) Schematic of several solid−solid interfaces in an ASSB that limit Li-ion transfer due to imperfect contact, insulating binder, and conductive carbon. (b) Structure of glyme and LiG_3−TFSI (solvated IL) and schematic of LiG_3 drop-cast onto LPS−LFP to wet the interface for better Li-ion transport accompanied by charge−discharge voltage profiles of $LiFePO_4$/Li−In all-solid-state cells with and without LiG_3 at 0.1 C (17 mAg^{-1}) at 30 °C. Reproduced with permission from ref 208. Copyright 2015 Wiley-VCH Verlag. (c) Schematic of incorporating an ionically conductive polymeric binder between the cathode and SE for better ion transport across the interface (compared with an insulating binder that hinders ionic motion) and first cycle charge−discharge voltage profiles of NCM/Li−In ASSB with and without LiG_3-NBR binder at 30 °C at 0.1 C. Reproduced with permission from ref 209. Copyright 2019 Wiley-VCH Verlag. (d) Schematic illustration of the formation of an LiF-rich SEI layer between Li metal and LPS with the addition of 6 M LiFSI/DME. Galvanostatic lithium plating and stripping of Li/LPS/Li and Li-LiF/LPS/LiF-Li symmetric cells.[210]

very reactive with LEs (as the high-charge density P^{5+} is prone to nucleophilic attack). For example, Yang Oh et al. have shown that only solvated ionic liquids (IL, made with triglyme and LiTFSI) is stable with Li_3PS_4 ($Li(G_3)$-TFSI, 1:1 molar ratio) as bare triglyme or excess triglyme dissolves and degrades LPS (Figure 25b).[208] With ($Li(G_3)$-TFSI (solvated IL), all of the triglyme molecules are used to chelate with Li-ion, leaving no free triglyme to react with LPS. The theoretical capacity of LFP was realized with the LPS-LiG_3(TFSI)-based composite, whereas barely any capacity was found for only LPS (Figure 25c).

2. Yang Oh et al. applied a conductive binder comprising nitrile rubber (NBR) mixed with $Li(G_3)$-TFSI.[209] The mechanical flexibility of a polymer electrolyte not only helps as a binder, but it also helps to wet the interface without blocking Li-ion transfer and can possibly act as a mechanical buffer layer to accommodate the stress induced by electrode volume change. The addition of 3.5 wt % conductive binder enhanced the first cycle CE of

https://dx.doi.org/10.1021/acs.chemrev.0c00101
Chem. Rev. XXXX, XXX, XXX−XXX

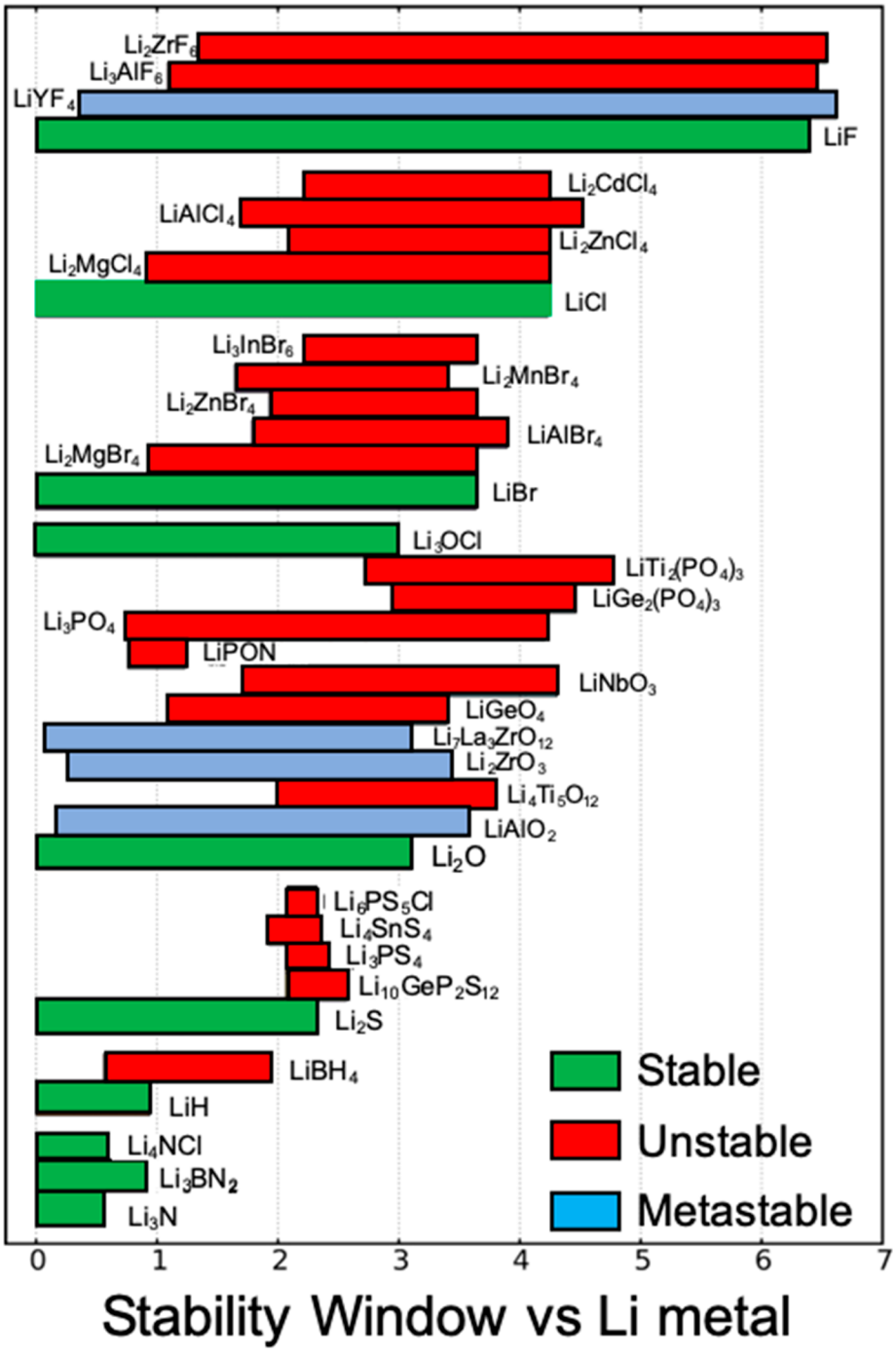

Figure 26. Electrochemical stability of several SEs. (Red) Thermodynamically favorable decomposition energy (unstable with Li metal), where reductive decomposition occurs at voltages >0.5 V versus Li/Li^+; (green) thermodynamically unfavorable decomposition energy (stable with Li metal), where there is no decomposition at 0 V; (blue) low decomposition energy (kinetically stable with Li metal) where decomposition occurs close to 0 V. Reproduced with permission from ref 30. Copyright 2016 American Chemical Society.

NCM electrode with a higher discharge capacity than the bare electrolyte without any binder (Figure 25c).

3. The wettability of SE with Li metal is a very critical problem, since a nonwetted interface can result in selective Li metal deposition, which generates hot spots for dendrite growth, leading to cell failure. Fan et al. have drop-casted a high molar concentration LE between Li metal and LPS which instantaneously decomposes to form a LiF-rich artificial SEI (Figure 25d).[210] The LiF-rich SEI not only fills the gap between Li metal and SE but also acts as an ionic conductor enabling a homogeneous flux of Li ions, therefore preventing dendrite growth. This LiF-rich SEI survives during 2 mA/cm^2 plating and stripping, whereas the interface between bare LPS and Li metal experiences dendrite growth at an applied current density of 0.5 mA/cm^2 (Figure 25d).

Although the addition of Li-ion conducting substances enhances the performance of ASSBs, the practicality of such a process is questionable. For example, (1) SE is already much denser than LE, so the addition of extra LE could compromise

https://dx.doi.org/10.1021/acs.chemrev.0c00101
Chem. Rev. XXXX, XXX, XXX−XXX

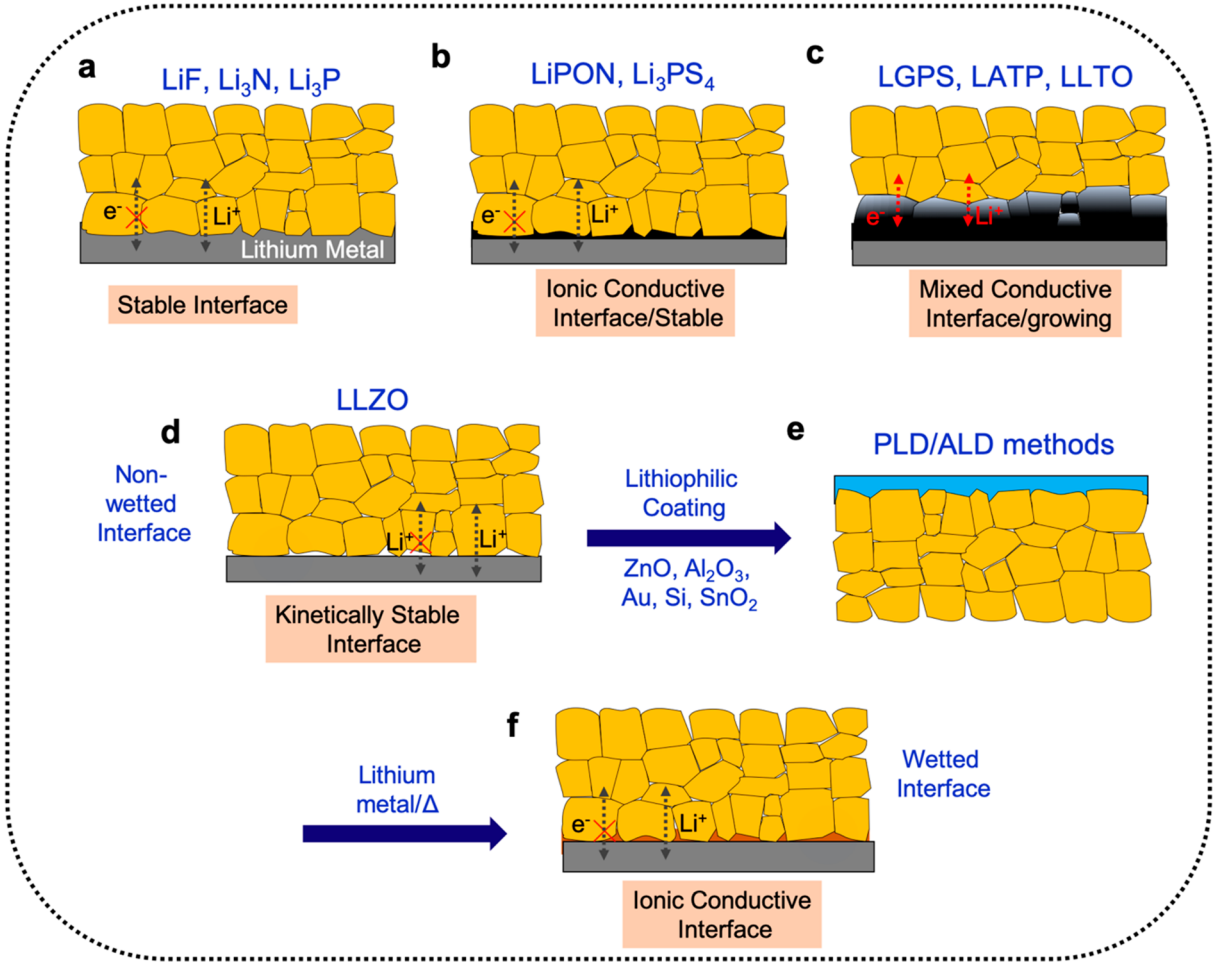

Figure 27. (a) Binary oxides, such as LiX (X = Cl^-, Br^-, I^-, or F^-), Li_3P, Li_3N etc. are stable with Li metal and exhibit no instantaneous chemical decomposition, thus forming a stable interface. (b) Solid electrolytes which instantly decompose upon contact with Li metal to form an ionically conductive interface, which remains stable after formation. (c) SE, which decomposes upon contact with Li metal to form a mixed conductive interface, which grows continuously, eventually resulting in cell shorting. (d) SEs such as LLZO are kinetically stable with Li metal and do not wet with Li metal due to a surface energy mismatch, which results in interfacial gaps between LLZO and Li metal. (e) Additional lithophilic coatings are applied on LLZO surface by PLD or ALD followed by (f) heating with Li metal. The lithophilic coating is activated by heating in inert conditions (Argon atmosphere) where diffusion and chemical reaction between the lithophilic layer and Li metal occurs to form a stable, ionically conductive interface.

the energy density, (2) additional problems associated with the cathode−LE interface could arise, for example, metal dissolution, (3) due to the fluidic nature of LE, there is a possibility of a small amount of LE settling underneath the battery pack, leaving the top side dry, (4) the long-term mechanical property of SEI or gel-like SE under stack pressure is questionable, and (5) fabrication difficulties related to handling LEs.

Over the last ten years, there have been significant improvements on cathode−SE interface modifications and characterization, namely in protective coatings that dramatically improve electrochemical performance. However, there are still fundamental questions that need to be answered, such as what the mechanisms are behind SEI formation, the chemical composition, and its specific role in ASSBs. Future research should focus on developing or exploring new characterization methods for the interface. Thorough electrochemical analyses, previously established for conventional LE-based cells, should be conducted to study the ASSBs, such as temperature-dependent impedance measurements, charge-transfer kinetics, and impedance measurements at different states of charge. Such analyses, coupled with collaboration between experimental and computational work, a necessary to more fully understand ASSB interfacial phenomena. This will surely bolster current efforts to screen and design electrode−SE interfaces to better understand and enable next-generation ASSB technologies.

5. ANODE INTERFACE

One of the reasons behind the growing interest in SEs is the potential application of the high-capacity Li metal anode, which would increase the energy density of the ASSB by at least 20%. It is well-known that Li metal is very electropositive and reactive, which means it will spontaneously react with most SEs at RT, forming a SEI. Chemical, mechanical, and electronic properties of this interphase are crucial for determining the long-term electrochemical behavior and viability of ASSBs.

5.1. Chemical Reaction

There are three main types of interfaces that exist depending on the reactivity of the SE with Li metal:[37]

1. Thermodynamically unstable interface/high decomposition energy at RT.
2. Kinetically stable SE with very low thermodynamic decomposition energy.

https://dx.doi.org/10.1021/acs.chemrev.0c00101
Chem. Rev. XXXX, XXX, XXX−XXX

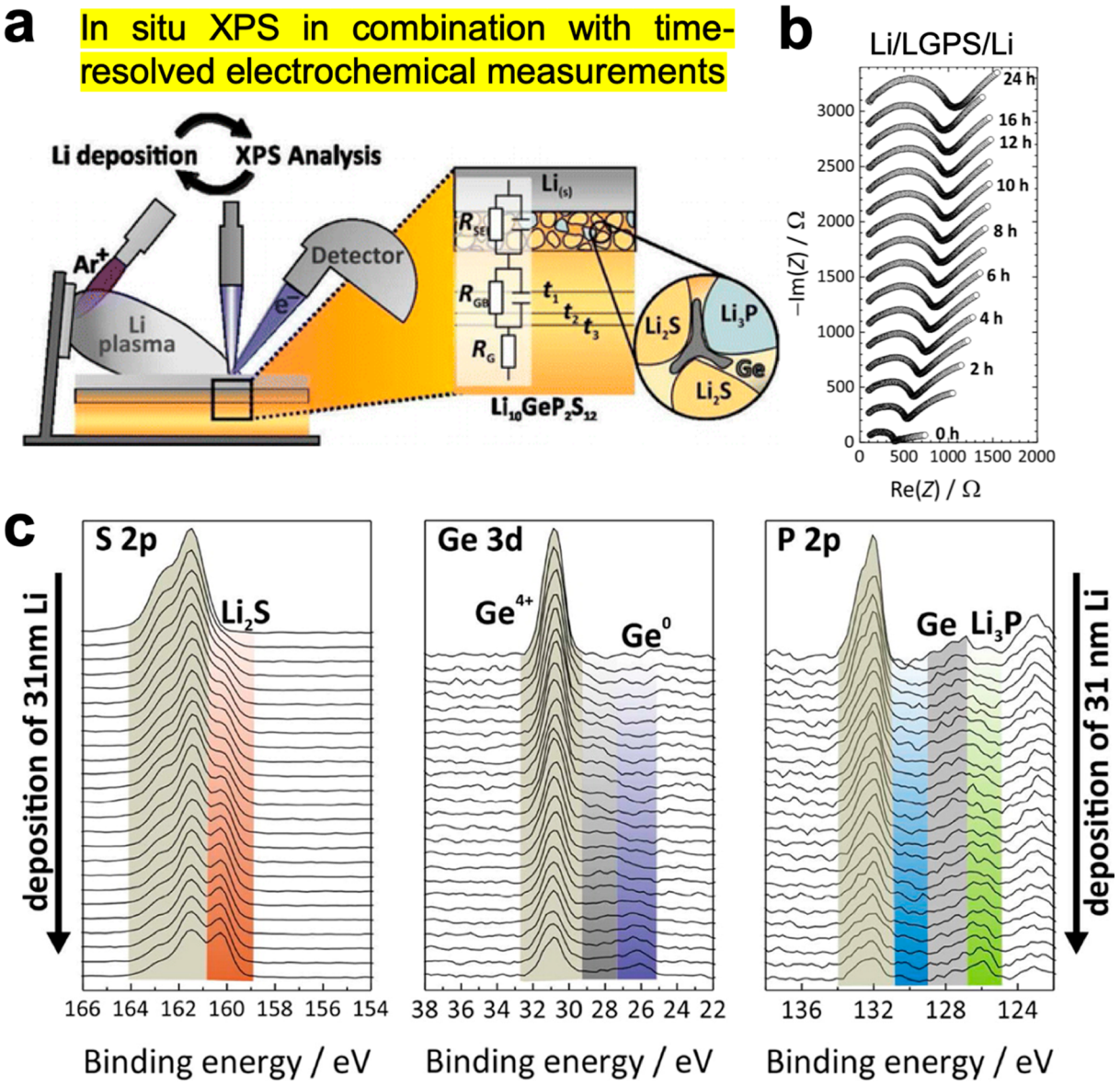

Figure 28. (a) Experimental setup for *in situ* XPS measurements of the interaction between LGPS with evaporated Li. (b) Impedance of the Li/LGPS/Li symmetric cell, which shows impedance increasing with time. (c) S 2p, P 2p, and Ga 3d XPS spectra of a $Li_{10}GeP_2S_{12}$ sample as the amount of deposited Li metal increases (from top to bottom). The formation of new species is colored and labeled, showing the decomposition of the original SE phase to form Li_3P, Li_2S, and LiGe alloy. The decomposition proceeds as more Li metal is deposited. Reproduced with permission from ref 333. Copyright 2016 American Chemical Society.

3. Thermodynamically stable interface with no decomposition energy.

Most binary ionic conductors are chemically stable with Li metal as no decomposition occurs at 0 V (Figure 26, green bars). For the ternary and quaternary ionic conductors, the stability against Li metal depends on the formation energy of their corresponding binary decomposition products. For example, Li_6PS_5Cl decomposes to form Li_2S, Li_3P, and LiCl (with a negative or favorable formation energy). The anodic stability of such conductors increases as the electronegativity of their anions increases. For example, the average stability of ionic conductors (against Li metal) is higher for fluorides compared to chlorides, and higher for chlorides compared to bromides. There is another kind of SE which is kinetically stable with Li (Figure 26, blue bars), which will be discussed in more detail later in this section.

Depending on the reactivity with Li metal and the properties of the SEI, the interface can be categorized into three types (Figure 27). (1) A chemically stable interface with no SEI layer, allowing efficient Li-ion transfer from Li metal to SE (Figure 27a). (2) An ionically conductive but electronically insulating interphase, where at least one of the SEI components is ionically conductive and is stable once formed (Figure 27b). (3) A mixed conducting interface where both ionically and electronically conductive materials are present. This interface is not stable and will continue to grow during cycling, which means the interfacial resistance will continue to increase (Figure 27c).

The highly ionically conductive LGPS SE was found to decompose when in contact with Li metal, because the SE has a favorable decomposition energy of energy of −1.2 eV/atom.[11] The products at the interface were predicted to be Li_2S (an insulator), Li_3P (an ionic conductor), and Li−Ge alloys

https://dx.doi.org/10.1021/acs.chemrev.0c00101
Chem. Rev. XXXX, XXX, XXX−XXX

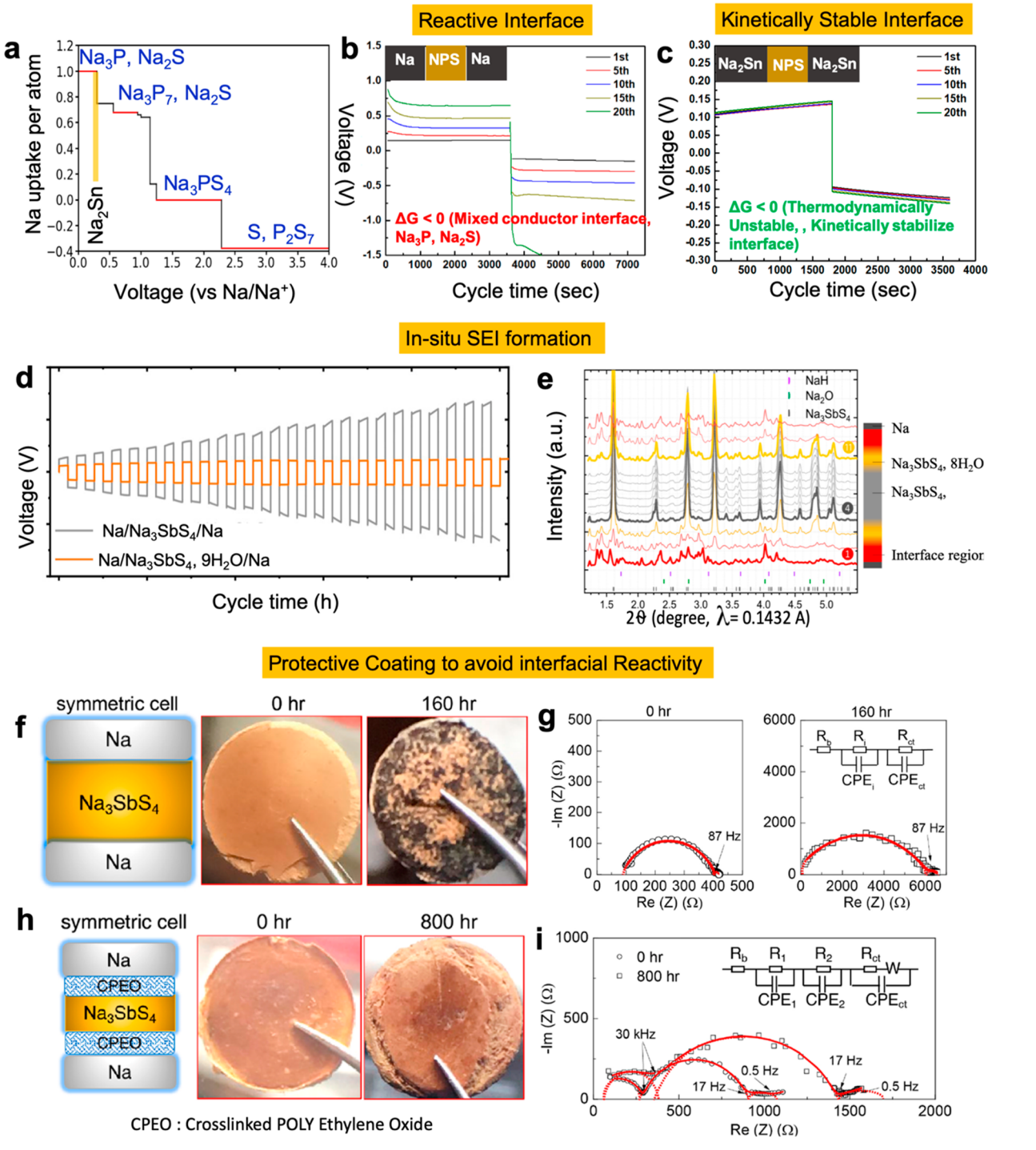

Figure 29. (a) Grand potential diagram of Na_3PS_4 (NPS) showing that NPS is thermodynamically unstable with Na_2Sn alloy (0.3 V vs Na/Na^+), marked with a yellow line (inset), (b) Plating and stripping of $Na/Na_3PS_4/Na$, which shows a gradual and steady voltage increase resulting from a growing interface due to spontaneous chemical reactions to form a mixed-conducting SEI (Na_3P is an electronic conductor), (c) Plating and stripping of Na−Sn 2:1 (0.3 V vs Na/Na^+) with Na_3PS_4, showing a kinetically stable interface, (d) Plating and stripping of Na with NAS and hydrated NAS, and (e) Synchrotron XRD depth profiling of $Na/NAS.9H_2O/Na$ symmetric cell (along the vertical axis) where each XRD pattern represents one layer of the schematic illustration on the right marked by multiple colors. Reproduced with permission from ref 222. Copyright 2019 Cell Press. (f) Another example of a spontaneous reaction; plating and stripping of a $Na/Na_3SbS_4/Na$ symmetric cell resulted in a black-colored SEI product. (g) The impedance increased by more than an order of magnitude after 160 h (cell at rest). (h) Applying CPEO (which is stable with Na) on both sides of NAS to avoid direct contact between Na metal and NAS. The chemical reaction is avoided as no black color was found after the NAS pellet was removed, resulting in (i) no significant increase in impedance after 800 h (cell at rest). Reproduced with permission from ref.[225] Copyright 2019 American Chemical Society.

(electronic conductors), collectively making the interphase a MIEC. These species were verified experimentally via XPS by Wenzel et al., where they performed *in situ* XPS with deposition of Li metal on top of the LGPS surface, where the signal intensities of Li−Ge alloy, Li_3P, and Li_2S all increased with increasing thickness of deposited Li (Figure 28a,c).[211] Li−Ge in

https://dx.doi.org/10.1021/acs.chemrev.0c00101
Chem. Rev. XXXX, XXX, XXX−XXX

contact with SE enables the continued decomposition of LGPS, which gradually increases the anode interfacial impedance and eventually contributes to cell failure (Figure 28b). The same principles apply for Si-, Sb-, Sn-, and As-based SEs, as they all form an electronically conductive alloy with Li at RT. Similarly, Ti- and Ge-based NASICON SEs react with Li metal at RT, where Ti^{4+} gets reduced to (the electronically conductive) Ti^{3+}, Ge^{4+} reduces to Li−Ge alloy, and Ta^{5+} to Ta^{4+}.[212] Hartmann et al. suggested that the formation of a mixed-conducting phase by reacting Li metal with LAGP makes such a dynamic growing interface. Therefore, these electrolytes are not suitable for application in an ASSB with a Li metal anode. On the contrary, enthalpy calculations show that Sc-, Y-, Ca-, Be-, Mg-, and La-oxides could be stable with a metallic Li metal anode.

Only phosphorus-based sulfide SEs are known to be relatively stable with Li metal since the expected decomposition products of these electrolytes, (Li_2S, Li_3P, and LiX (X = Cl, Br, I)) are insulating materials that are thermodynamically stable with Li metal.[11] LPS (glass or glass ceramic, with composition ratios ranging from 70:30 to 80:20 of Li_2S:P_2S_5) and argyrodite-based SEs (Li_6PS_5X, X= Cl, Br, and I) have been proven to form a stable interface and promote a long cycle life.[213] The interface stability is attributed to the absence of any electronically conducting species, allowing the interphase to self-passivate. Tatsumisago et al. showed that although the impedance of the LPS glass electrolyte increases by almost 40% after 24 h when in contact with Li metal, subsequent increases in impedance were negligible (<10% over the next 500 h).[214] Using the Warner diffusion-controlled solid-state reaction model, Wenzel et al. showed that the kinetics of interfacial impedance growth is lower for $Li_7P_3S_{11}$ and Li_6PS_5Cl in comparison with LGPS. In other words, LPS- or LPSX-based SEs can act as a thin protective layer between Li metal and LGPS.[59]

Since most SEs are unstable with Li metal, there are few reports on the fabrication of ASSBs with Li metal as the anode. Alternatively, anodes such as indium metal or Li−In alloy (3 wt % Li) have been used in ASSBs and they have been shown to operate at a high current density without any growth of dendritic Li. Tatsumisago et al. showed that Li dendrites can grow through the voids of LPS when a current density of 0.075 mA/cm^2 is applied. However, when $Li_{0.5}In$ is used as the anode, the applied current density can be increased to the order of 1 mA/cm^2 without any dendritic growth.[214] However, these findings remain controversial as there are other reports of using Li metal at current densities greater than 0.5 mA/cm^2.[215,216] Dehnen et al. showed that there is no increase in impedance of the electrolyte Li_6PS_5I for the first 17 h, contradicting the findings from Janek et al., where significant interfacial growth rates were observed even when using the same materials.[213,217] This perceived inconsistency among these reports possibly arises from differences in cell fabrication, such as differences in applied pressure as well as the source of Li and amount of the Li used.

Although a few SEs exhibit very high ionic conductivity, their practicality for application in an ASSB is still limited, mainly due to the formation of a MIEC interface. There are multiple ways to avoid such an interface to apply such highly ionically conductive SEs for practical battery applications. For example, Na_3PS_4 (NPS) is not stable with Na metal according to the grand potential diagram, as Na_3P, an electronic conductor, forms at the interface (Figure 29a). This results in a steadily increasing polarization as plating and stripping proceeds for an Na/NPS/Na symmetric cell (Figure 29b). However, by using a Na−Sn alloy (Na−Sn 2:1, 0.3 V vs Na/Na$^+$) as an alternative to Na metal, stable plating and stripping was observed without any change in polarization for 40 h (Figure 29c). This result is an example of a kinetically stabilized NPS interface, and most ASSBs with NPS as an SE use Na−Sn alloys as the anode to achieve longer cycling.

Another effective way to apply such reactive SEs in ASSBs without compromising the high ionic conductivity is to employ a thin barrier layer between the SE and Li (or Na) metal. The necessary criteria of such a layer is that it must be thermodynamically stable with both the Li (or Na) metal and SEs, ionically conductive, electronically insulating, and mechanically ductile for effective contact between SE and Li metal. A highly ionically conductive coating helps to promote ion diffusion at high current densities to deposit metal underneath the coating layer without a dramatic increase in polarization. To this end, several protective layers have been applied to the metal interface to improve the metal-based ASSBs. For example, *in situ*-formed $LiHPO_4$ on Li metal (by reacting Li with H_3PO_4 and THF) allows for LGPS/LCO ASSBs to run over 500 cycles with more than 86% capacity retention.[218] Sahu et al. stabilized the highly ionically conductive $Li_{3.833}Sn_{0.833}As_{0.166}S$ with Li metal by using a $3LiBH_4$:LiI thin layer (drop-casted with THF solvent).[219] Other protective inorganic oxide coatings include ZnO, Al_2O_3, $LiSiS_x$, and hybrid SEs. Some of these coatings can stabilize Li metal even in dry room conditions.[220,221] Tian et al. found that $Na_3SbS_4 \times H_2O$ is stable with Na metal due to the formation of a passivation layer containing NaH and Na_2O (formed by Na metal reacting with the water, Figure 29d), which can be used to protect the NAS, resulting in prolonged and more stable plating and stripping in a Na symmetric cell (Figure 29e).[222] However, applying such coatings on a larger scale is challenging since it requires additional processing and will increase costs.

As before, mechanical properties also play an important role in determining the performance of the coatings since Li metal effectively undergoes an infinite volume change during cycling, which will produce a large amount of stress in the coating layer. The oxide coatings, (such as ZnO and Al_2O_3) known for their high Young's Modulus (indicating their stiff nature), cannot easily accommodate the large stresses induced by Li metal deposition; thus, cracks will form. Such cracks will act as hot spots for Li dendrite nucleation and growth that will eventually short the cell. Mechanically, polymers or hybrid coating layers outperform oxides in accommodating the induced stress as they have more suitable mechanical properties such as lower stiffness.[223,224] To demonstrate this point, Na_3SbS_4 (NAS) can be used as an example. NAS is unstable with Na metal, spontaneously reacting to form a black-colored SEI (Figure 29f), which is due to the formation of the electronically conductive Na_3Sb alloy, resulting in a 2 orders of magnitude growth in impedance for a Na/NAS/Na symmetric cell after 160h at rest (without any cycling) (Figure 29g). Incorporating cross-linked PEO (CPEO) between NAS and Na metal mitigated this chemical reaction as no black-colored SEI was seen after disassembling the cell (Figure 29h). The change in impedance was much less drastic, as observed by a Na/CPEO/NAS/CPEO/Na symmetric cell after 400 h at rest (Figure 29i).[225]

The disadvantage of polymer electrolytes is that they usually have low ionic conductivity and a low transference number (0.2−0.5) at RT, which results in rapid anion depletion at the Li metal interface, exacerbating an uneven distribution of electric field, in turn promoting the nucleation of Li dendrites (especially

https://dx.doi.org/10.1021/acs.chemrev.0c00101
Chem. Rev. XXXX, XXX, XXX−XXX

at high current density).[226,227] Goodenough et al. introduced a new flexible polymer on LATP in a sandwich geometry (polymer/LATP/polymer) which does not allow anions to pass through, therefore preventing the depletion of anions at the Li metal interface.[226] These cells demonstrated a CE of 99.9% and a cycle life of 640 cycles at RT. Sputtering-based deposition of LiPON has also been used as a protective layer on LATP because it forms a passivation layer (by reacting with Li metal); LiPON itself is also known for mitigating dendrites.[228] However, most of these coating processes are expensive as they involve multistep fabrication procedures.

A few ionic conductors, particularly oxides such as LLZO and $LiAlO_2$ decompose close to 0 V versus Li/Li^+. Such ionic conductors are known to be kinetically stable due to a high activation barrier required to break the metal−oxygen bonds, leading to the formation of binary oxides, Li_2O, and metal-oxides. In general, a kinetically stable interface means there is a low decomposition energy of SE with Li metal. Regarding sulfide SEs, various substitutions have been made to passivate, or kinetically stabilize, the interface with Li metal without an additional protective layer. For example, oxygen substitution into LGPS not only improved the ionic conductivity (8.43×10^{-2} S/cm for $Li_{10}GeP_2S_{11.7}O_{0.3}$ compared to 1.12×10^{-2} S/cm for LGPS) but also stabilized the interface with Li metal.[229] Similar observations were noticed for oxygen-substituted LPSBr ($Li_6PS_{4.7}O_{0.3}Br$).[230] Besides oxygen, metal-sulfide doping (such as the MoS_2-modified $Li_2S-P_2S_5$ glass ceramic, $Li_7P_{2.9}S_{10.85}Mo_{0.01}$) showed a lower interfacial resistance with Li metal than $Li_7P_3S_{11}$.[231] $Li_{3.06}P_{0.98}Zn_{0.02}S_{3.98}O_{0.02}$ has been synthesized by doping Li_3PS_4 with ZnO, which was also shown to have better stability with Li metal (demonstrated 81% capacity retention after 100 cycles compared to 35% for bare Li_3PS_4).[232] Although it is hypothesized that suitable elemental substitution kinetically stabilizes the Li metal interface, long cycle life (>1000 cycles) with such modified SEs still remains a question. High temperature cycling and molecular dynamics-based simulations are required to identify the limits of the kinetics.

A thermodynamically stable interface is formed when there is no negative decomposition energy between Li metal and SEs. Binary SEs are known to form such a thermodynamically stable interface (Li_2S, Li_3P, Li_3N, LiCl, LiF, etc.). In binary ionic conductors, the anions are in their fully reduced state (X^-, S^{2-}, N^{3-}, P^{3-}, O^{2-}), so no further reduction occurs, which is why they are stable with Li metal anode and at 0 V. Li_3N and Li_3P are known to be good ionic conductors at RT (10^{-4}-6×10^{-3} S/cm, depending on synthesis conditions, crystallinity, and doping)[233] but possess very poor oxidation stability, which prohibits their use in practical ASSBs. However, Li_3N was useful instead as a thin protective coating layer on Li metal to mitigate interfacial parasitic reactions and prevent dendrite growth.[234−237] Moreover, LiCl and LiF are known for their high oxidation stability but ultralow ionic conductivity at RT.[238,239] A thin LiF layer formed *in situ* or *ex situ* is promising as a way to protect Li metal in both SE- and LE-based batteries.

5.2. Anode Physical Contact

Although oxide-based SEs exhibit a high ionic conductivity in the range of 10^{-4}−10^{-3} S/cm at RT, the interfacial charge transfer resistance with Li metal is significantly larger and the critical current density (CCD) for dendrite formation is less than 0.5 mA/cm^2, hindering their application in ASSBs with Li metal.[240−243] This problem fundamentally arises from contact between SE and Li metal. Because of the low voltage reduction stability of LLZO (0.05 V vs Li/Li^+), which makes it kinetically stable with Li metal at RT), it is difficult to maintain intimate contact even with an applied constant pressure; small gaps form as a result. The size and distribution of these gaps depends on the mechanical properties and surface microstructure of SEs as well as the applied stack pressure during fabrication and cycling. Such insufficient contact has two major impacts on the cycling of ASSBs: (1) inhomogeneous contact increases charge transfer resistance with Li metal by at least an order of magnitude;[244−247] (2) the inhomogeneous current distribution at the Li metal−SE interface will act as "hot spots" for Li dendrite nucleation during plating and stripping.

The most common process to enhance the surface wettability of Li metal is by using a thin lithophilic coating between the SE and Li metal; in other words, these materials must be reactive with Li metal. ALD, MLD, and PLD can be used to deposit a thin layer of lithophilic materials on top of the SE (Figure 27d−f). The major criteria for such a coating is (i) the coating should be stable with the SE; (ii) the coating should have a high Li-diffusivity so that deposited Li can diffuse easily from the SE to the Li metal interface; (iii) the coating should not change in volume during the charge−discharge process; (iv) the coating should be thin (low mass) enough such that it should not significantly sacrifice the energy density of the ASSBs. Several lithophilic coatings (including metals, metal-oxides, metal-nitrides) have been used to modify the SE surface to reduce the interfacial resistance.[207,248] Lu et al. used a thin (10 nm) amorphous Si layer on top of Ca- and Nb-doped LLZO (using PECVD), which reacts with Li to form a Li−Si alloy. Such a process reduced the interfacial resistance from 925 Ω/cm^2 to 127 Ω/cm^2, a 7-times decrease. The high diffusivity of Li in the Li−Si alloy ($D_{Li+} \approx 10^{-12}$ m^2/s) allows for plating and stripping at a current density of 0.2 mA/cm^2 for over 200 h without any significant polarization changes.[236,249] The reaction energy between LLZO and Li−Si alloys is also quite low, which ensures kinetic stabilization of the interface. Several other metals (Ge, Au, Mg, Al, etc.)[250−252] and salts have been used for such lithophilic coatings. Fu et al. noticed that the coating thickness matters; a 5−10 nm Mg coating on LLZO lowered the contact resistance whereas increasing thickness to 100 nm increased the contact resistance.[253] Although such inorganic coatings have been used to improve the surface wettability, they usually require high-cost processing and have scalability problems.

Furthermore, mechanically deformable materials such as ionic liquids, polymers, or gel-based interfacial coatings have been used to further decrease contact resistance between LLZO and Li metal.[254−260] Zhang et al. introduced a highly conductive PVDF-HFP-based porous gel polymer electrolyte (5×10^{-4} S/cm at RT) and decreased the Li−LLZO interface resistance from 1400 to 214 Ω cm^2 which enabled long, stable, and dendrite-free cycling (0.12 mA/cm^2) of ASSBs.[255] However, the disadvantage of such gel polymer electrolytes is that the long-term cycling stability and mechanical properties highly depend on the amount of LE inside the polymer matrix. Moreover, the CCD for dendrite prevention is also limited when applying such soft materials at the interface, drops far below the requirement for EV applications (10 mA/cm^2). Further increasing the stiffness of polymer film by the addition of fillers such as SiO_2, TiO_2, $BaTiO_3$, LLZO, and Al_2O_3 etc. could improve the CCD.

Although coatings can significantly enhance Li plating and stripping at a higher current density, the CCD is still much lower than what is required for practical applications. Further

https://dx.doi.org/10.1021/acs.chemrev.0c00101
Chem. Rev. XXXX, XXX, XXX−XXX

Table 1. Summary of Anode Protection Layers and Their Effects on Cell Performance

anode	SE	protection layer	current density (mA/cm^2)	time (h)	electrode	performance (temp/rate/capacity retention/no. of cycles)	ref
Li	$Li_{10}GeP_2S_{12}$	LiH_2PO_4	0.1	950	TiS_2	RT/0.1C/86.7%/500	218
Li−In	$Li_{10}GeP_2S_{12}$	Li_3PS_4	60 mA/g		TiS_2	30 °C/20C/rate testing/100%	59
Li	$Li_{10}SnP_2S_{12}$	aglucone	0.1	166	$LiCoO_2$	55 °C/1C/50%/150	269
Li	$Li_{10}GeP_2S_{12}$	$Li_3P_{0.98}Sb_{0.02}S_{3.95}O_{0.05}$	0.1−1	500	$LiCoO_2$	RT/0.1C/78.6%/50	270
Li	$Li_{10}GeP_2S_{12}$	1 M LiTFSI in DOL/DME	0.1	1600	TiS_2	RT/0.1 mA cm^{-2}/91.7%/200	271
Li	$Li_7P_3S_{11}$	LiF	0.5	400	$LiCoO_2$	RT/0.1 mA cm^{-2}/96.8%/200	272
Li	$Li_{10}SnP_2S_{12}$	1.5 M LiTFSI/Pyr_{13}TFSI	0.038	1000	$LiFePO_4$	RT/0.1C/84.7%/30	273
Li	$Li_{10}GeP_2S_{12}$	$Li_{3+3x}P_{1-x}Zn_xS_{4-x}O_x$			$LiCoO_2$	RT/0.1C/81%/100	232
Li	$Li_7P_3S_{11}$	$Li_xAl_{(2-x/3)}O_3$/Si					274
Li	$Li_{10}GeP_2S_{12}$	1 M LiTFSI/Pyr_{13}TFSI	0.038	1200	S	RT/0.083 mA/82.6%/50	275
Li	Li_3PS_4	Li_xSiS_x	0.5	2000	$LiCoO_2$	RT/0.13 mA cm^{-2}/94%/100	276
Li	$Li_{1.3}Al_{0.3}Ti_{1.7}(PO_4)_3$	Al_2O_3	0.01	600			220
Li	$Li_{1.3}Al_{0.3}Ti_{1.7}(PO_4)_3$	ZnO	0.2	1000	$LiFePO_4$	RT/0.1C/99%/200	221
Li	$Li_{10}GeP_2S_{12}$	succinonitrile in 1 M LiTFSI	0.13	250	$LiFePO_4$	RT/0.1C/99%/120	277
Li	$Li_{10}GeP_2S_{12}$	7 M LiTFSI electrolyte with TTE	OCV	50		negligible impedance increase after adding LE compared to bare LGPS	278
Li	$Li_7P_3S_{11}$	Li_3N			Li_2S	RT/45%/120	235
Li	$Li_{3.833}Sn_{0.833}As_{0.166}S_4$	3 M $LiBH_4$·LiI in THF	0.1	1200			219

enhancement will need a deeper mechanistic understanding of the wetting behavior of the SE−anode interface and interfacial charge transfer resistance. Several studies showed that surface impurities play a key role on the wetting behavior of LLZO with Li metal. Intrinsically, LLZO forms carbonates and hydroxides at the interface by reacting with air.[261−266] The conductivity of LLZO drops in humid air from 6.46×10^{-4} S/cm to 3.62×10^{-4} S/cm, which originates from LiOH (Li exchange with protons) and Li_2CO_3 (reaction with CO_2) at the interface. The presence of LiOH and Li_2CO_3 impurities acts as a shell on the LLZO particle and plays a crucial role on surface chemistry and wettability.[267] It is possible to reduce the interfacial resistance between lithium and LLZO to 2 Ω/cm^2 (a value close to LE) with clean, LiOH and Li_2CO_3 surfaces, and to enable cycling a Li metal symmetric cell at 0.3 mA/cm^2 over several hundreds of hours without any shorting (see Table 1).[268]

5.3. Mechanical Effects

Recently, it has been realized that understanding the mechanical properties of SEs and Li is critical for increasing the CCD and enabling ASSBs without any dendritic growth of Li.[279−281] There are three main mechanical properties of SEs and Li that are related to the dendritic growth of Li.[14,282] They are

(1) Elastic behavior of the SE. The Young's modulus of the SE depends on the crystal structure and is independent of grain size and grain orientation. It is typically measured by indentation and the aquatic impulse method. The Young's modulus can be converted into the shear modulus (G) by the equation $G = E/2(1 + \nu)$ where G is the shear modulus and ν is Poisson's ratio.

(2) Plastic behavior of solids, or their hardness (H), which is a measure of the resistance to deformation. Deformation of SEs can happen during ASSB fabrication, by dynamic volume change of the cathode/anode during charging and discharging, and during Li growth inside voids, pores, and grain boundaries. Hardness is measured with micro-indentation (Vickers indenter, with loads typically ranging from 1 to 10 N with indent impressions as large as 20 μm for a polycrystalline solid) and nanoindentation (1 to 500 μN with indent impressions ≤1 μm in a single grain or single crystalline material).

(3) Fracture toughness is the capability of a material containing a crack to resist fracture, which is related to crystal structure, bonding, and microstructure. It is an important property for SEs since rapid fracture could occur during cell assembly or battery operation.

For the bare SE, Li plating happens at the electrode−SE interface, which then propagates along grain boundaries.[283−285] The deposited Li metal at the grain boundary interfaces increases the local electric field and promotes further Li deposition. Such deposition induces stress on SEs which increases as local current density increases. This stress can induce cracks in SEs (which are expected to propagate since grain boundaries have a lower yield strength than the bulk). However, there is a possibility that the stress created by the deposited Li can be alleviated instead of resulting in cracking within the SE. This process will depend on the stack pressure during cycling and the mechanical properties of SEs, as these directly affect the dendrite growth kinetics.

The Monroe−Newman criteria, which is applied to the polymer and Li metal interface, states that to mitigate dendrite growth through the SE, an effective SE must have a shear modulus (G) twice that of Li metal.[286−288] Considering the isotropic and polycrystalline nature of Li, the G_{Li} is ∼4 GPa. According to the Monroe−Newman criteria, the G_{SE} should thus be more than 8 GPa to prevent dendrite formation. Most of the oxide SEs have values of G in the range of 40−60 GPa, ten-times higher than Li metal. Thus, practically, oxide SEs are stiff enough to prevent dendrites. However, dendrite growth is still observed with an applied current density of 0.5 mA/cm^2. Considering other electrolytes such as glassy LPS, $G_{glassy\ LPS}$ is relatively low (7.1 ± 0.3 GPa), which signifies that dendrite growth is more likely to occur within sulfide SEs than oxides.

The Monroe−Newman criteria and other existing models are not applicable to polycrystalline materials as they do not consider microstructural inhomogeneity;[288,289] thus, it is more appropriate to consider the mechanical properties of the grain boundaries rather than the bulk since dendrite growth primarily

https://dx.doi.org/10.1021/acs.chemrev.0c00101
Chem. Rev. XXXX, XXX, XXX−XXX

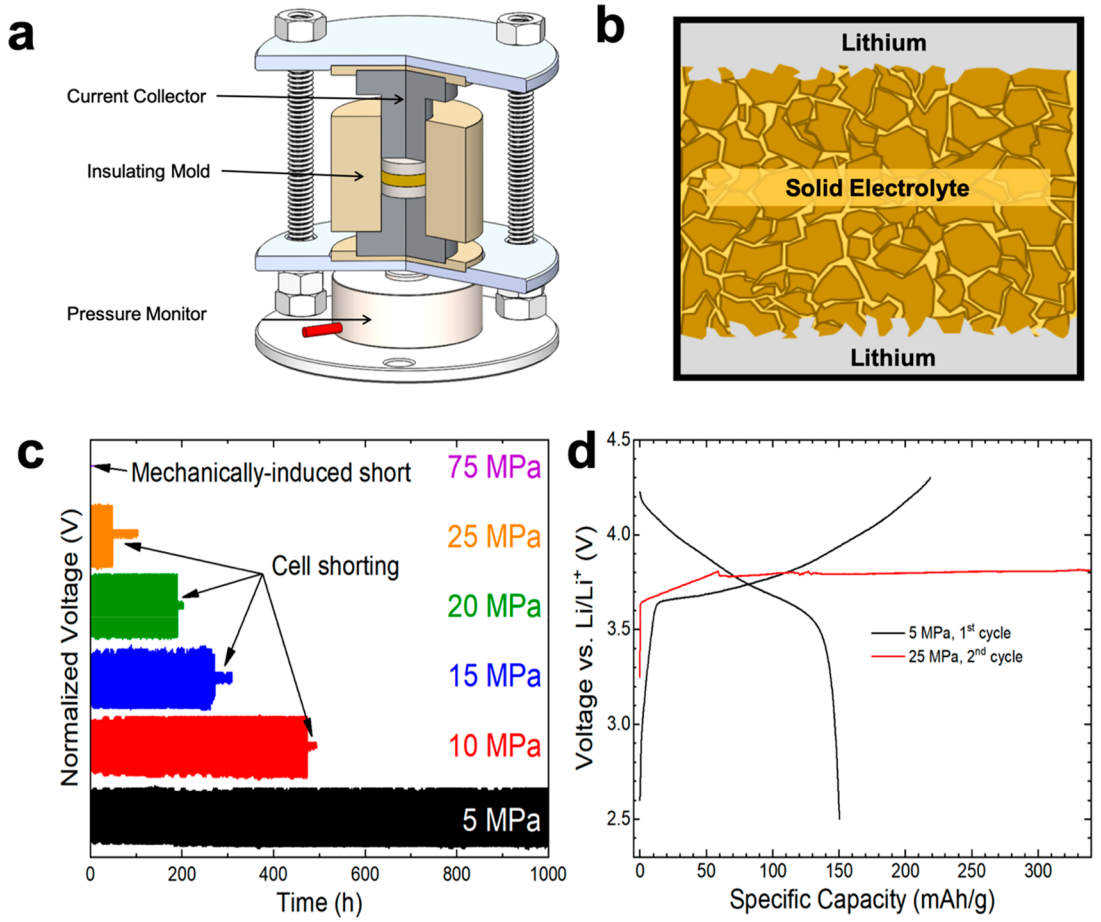

Figure 30. (a) Schematic of the load-cell setup to monitor pressure in an ASSB. (b) Schematic of the Li/LPSCl/Li symmetric cell. (c) Plating and stripping for the Li/LPSCl/Li symmetric cell for different applied stack pressures with an applied current density of 0.075 mA/cm^2. Reducing the stack pressure increased the plating and stripping time. (d) Charge/discharge profile of the NCA-LPSCl cathode composite (with Li metal anode) for an applied stack pressure of 5 and 25 MPa; the 5 MPa cell runs but the 25 MPa cell exhibited shorting. Reproduced with permission from ref 146. Copyright 2019 Wiley-VCH Verlag.

occurs along grain boundaries. Because of the high surface energy of grain boundaries, their stiffness can be 20−60% lower than the bulk. Seigel et al. performed MD simulations on tilt and twist grain boundaries and found that the shear modulus at grain boundaries is 50% less than the bulk.[290] Sakamoto et al. suggested that the elastic property of Li metal is highly dependent on crystal plane orientation (from 1.5 GPa (111) to 11 GPa (100)). This value is lower than the Monroe−Newman criterion for prevention of dendrite growth and explains a possible reason for dendritic growth in oxide-based SEs along grain boundaries.

The low yield strength of Li means that applied pressure (also called stack pressure) is also a major variable for consideration.[280] Li metal nucleation, deposition, growth inside SEs, and texture are highly dependent on the applied pressure. In addition, the low activation energy for self-diffusion in solid Li (50 kJ mol^{-1}) indicates that significant Li creep will occur at RT. There are two main creep mechanisms in a metal: diffusional creep and power-law creep. Diffusional creep occurs at very low stresses as atoms diffuse along grain boundaries, and is characterized by a linear relationship between stress and strain rate. Power-law creep dominates over diffusional creep at higher stresses, owing to its higher-order dependence on stress.

Doux et al. carried out a systematic study on the effect of stack pressure on Li dendrite formation (Figure 30).[146] A LPSCl pellet was made via cold-pressing resulting in a relative density of 87%, meaning there is interconnected porosity so dendrite growth may be observed. Initially, the pellet was pressed at 25 MPa (much higher than the yield strength of Li, 0.8 MPa) to mechanically wet the Li−LPSCl interface. If a Li metal symmetric cell was constructed at a very high pressure of 75 MPa, the cell immediately mechanically shorted even before applying current, due to power law Li metal creeping by dislocation climb at RT.[280,291] X-ray nanocomputed tomography (Nano-CT) images show that the SE layer ruptures at such a high pressure. At lower pressures, it was found that the time it took for the cell to short strictly depended on the applied stack pressure. A stack pressure of 10 MPa takes ∼5-times as long to short the cell than 25 MPa. It is believed that higher pressures increase the Li creep along the grain boundaries in the LPSCl pellet, forming a 1D-like dendritic structure. New Li will then plate due to the high electric field associated with the high surface-area structure. This promotes dendrite growth, which was verified with Nano-CT experiments. If 5 MPa is used, the symmetric cell did not exhibit any shorting. It is believed that although 5 MPa is still higher than the yield strength of Li, the pressure is insufficient to make Li creep inside the LPSCl pellet, thus resulting in homogeneous deposition of Li during plating and stripping. This was supported by the Nano-CT images.

https://dx.doi.org/10.1021/acs.chemrev.0c00101
Chem. Rev. XXXX, XXX, XXX−XXX

Correlating a relatively high current density (1 mA/cm^2) with stack pressure was conducted by Kasemchainan et al. in three electrode configurations, where the effect of plating and stripping kinetics on stack pressure and current density can be selectively monitored.[292] They have proposed three diffusion mechanisms that regulate lithium plating and stripping, such as J_{Li}^+ migration (the flux for Li ion migration from Li metal to SE, which depends on applied current density), J_{Li} diffusion (the flux for self-diffusion of Li atoms inside Li metal, which is constant at constant temperature and pressure), and J_{Li}^+ creep (the flux for Li metal creep, which depends on applied stack pressure). These three mechanisms are shown in Figure 31.

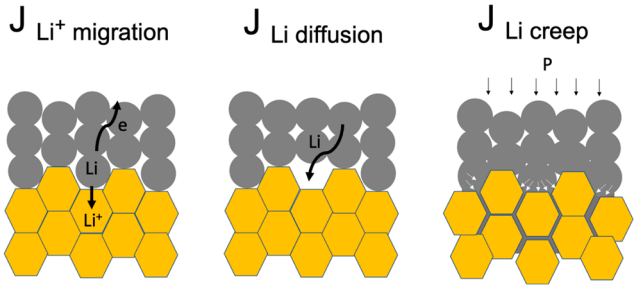

Figure 31. (a) Schematics of Li-ion migration from Li metal into SE during stripping. (b) Vacancy-induced Li-ion diffusion. (c) Li metal creep (by applying uniaxial stack pressure).

At a low stack pressure of 0.5 MPa, (lower than the yield strength of Li so creep is not expected), the plating polarization decreases (which is due to pore filling) whereas during stripping, polarization increases, since there is a loss of contact due to the formation of voids. These further limit the contact area between SE and Li metal, thereby increasing the cell resistance until the cell fails. Using a relatively higher pressure of 3 MPa resulted in smoother plating whereas stripping polarization still increased; voids still formed due to selective-area stripping. Void formation thus mainly dominates at low pressures and high current density, where Li-ion diffusion dominates over vacancy-induced Li self-diffusion along with pressure-induced creeping diffusion (J_{Li} diffusion + J_{Li} creep < J_{Li+} migration) (Figure 32).[293] As mentioned previously, voids will limit contact between Li metal and LPSCl, creating hot spots for Li deposition and dendritic growth along grain boundaries. At 7 MPa, no polarization changes were observed until after 100 cycles (J_{Li} diffusion + J_{Li} creep = J_{Li+} migration). However, increasing the current density to 2 mA/cm^2 caused the cell to short since once again the kinetics of ion migration dominated over creeping and internal vacancy-induced self-diffusion.[294] Similarly, void formation was also noticed on LLZO and other SEs.[294−296] This observation describes the limitation of applied current density and how it relates to stack pressure (regardless of the pellet porosity). Further optimization of stack pressure is required to be able to increase the applied current density to enable ASSB technology for EV applications. It is important to note that SEs, which are more deformable, amorphous, or are able to be pelletized with higher relative density should increase the CCD as it would decrease the number of creeping sites within the SE, allowing for more homogeneous plating and stripping.

Compared with Li metal, alloy-based anodes usually work very well at high pressures (even at pressures >75 MPa) and they usually do not exhibit any signature of dendrite growth. First, the yield strength of most alloys is much higher than Li, which means that there will be no creep inside the SE. Additionally, the alloying kinetics of most metals is expected to be highly thermodynamically favorable. Their faster kinetics and their very high self-diffusion coefficient will dominate over plating kinetics, so dendrite growth is avoided. It is also worth mentioning that alloys used as a counter electrode have a much higher N/P ratio such that it is more difficult for alloys get fully saturated with Li metal (for subsequent Li metal growth).

There are other hypotheses based on the effects of grain boundary size and their micro-orientation on the CCD.[284,297] Although uniform contact between Li metal and the SE is important for homogeneous nucleation, the density and interconnectivity of pores governs the growth kinetics of dendrites.[298] It is important to note that there are contrary observations with regards to grain size and CCD; Sakamoto et al. made LLZO samples with different grain sizes (with equal Li metal interfacial resistance and density) to isolate the grain size effect on CCD. They found that the CCD increases significantly with increasing grain size; as the grain size increased from 5 to 600 mm, the CCD increased from 0.3 to 0.6 mA cm^{-2}.[299] This high increase in current density is attributed to the increasing effective contact area between Li metal and the grains rather than between Li metal and grain boundaries. As grain size increases, there is a reduction in hot spots for Li nucleation and dendritic growth. However, Cheng et al. showed that the CCD increases when the grain size is reduced; they attributed this to the larger relative area fraction of grain boundaries at the Li−LLZO interface. Cheng et al., using SEM and high-spatial-resolution Auger spectroscopy, showed that metallic Li preferentially propagates along grain boundaries when the CCD is exceeded in hot-pressed LLZO and suggested that elimination of grain boundaries from polycrystalline LLZO could increase the CCD.[283,300] However, the atomic-scale orientation of the grains is also unknown. A high-temperature synthesis would be expected to form the lowest-disordered grain orientation whereas for a low-temperature synthesis, a more disordered grain structure is expected.[301−303] Thus, the synthesis temperature and the grain boundary structure would have a direct effect on the mechanical behavior at the SE−anode interface. Also, at the grain boundary and surface, LiOH and Li_2CO_3 contamination is quite common for LLZO which may also drastically change the mechanical behavior at the interface.

Grain boundary conductivity is important with regards to the nucleation and penetration of dendrites through the SE.[286] Even if uniform contact is made, for materials with higher grain boundary conductivity, Li tends to accumulate in nearby grain boundaries faster than grains, which means Li will further penetrate along grain boundaries of SEs and ultimately limit the CCD. However, there is also controversy regarding the grain boundary ionic conductivity, namely whether it is higher or lower than the grains. Several reports on grain boundary conductivity both experimentally and theoretically show that grain boundary conductivity is the bottleneck for achieving high ionic conductivity in LLZO. Some reports state an equal conductivity with an activation energy between the grain and grain boundaries, while others show a high grain boundary conductivity. The main question is whether a high grain boundary conductivity contributes to hot spot formation at nearby grain boundaries or grains. For example, Ga−LLZO has a higher grain boundary conductivity (2.4×10^{-3} S/cm) than Al−LLZO (2.4×10^{-4} S/cm), but Ga−LLZO can tolerate higher current densities than Al−LLZO. Federico et al. studied the nature of dendrites using TOF-SIMS and found Al and Li at the

https://dx.doi.org/10.1021/acs.chemrev.0c00101
Chem. Rev. XXXX, XXX, XXX−XXX

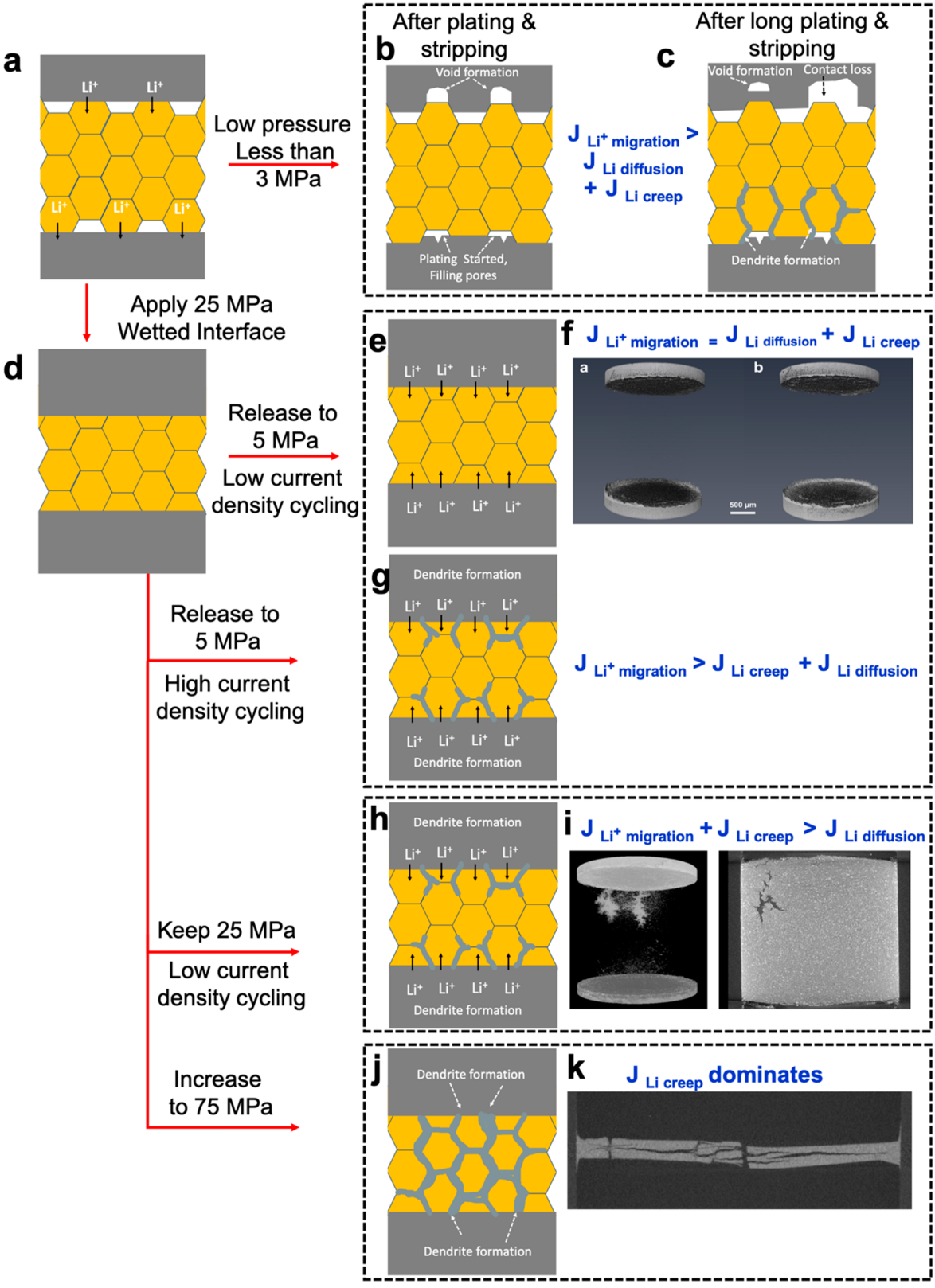

Figure 32. (a) Schematic of Li metal placed on both sides of a SE pellet. Many gaps are present if the applied pressure is <3 MPa. (b) Li plating and stripping at <3 MPa where significant void formation occurs on the stripping side (top right) and Li deposition on the plating side (bottom) fills the pores. (c) Isolated void formation and contact losses occur on the stripping side whereas selective area Li metal deposition (promoting dendrite growth) at the plating side over prolonged plating and stripping. (d) The interface is mechanically wetted with 25 MPa. (e) Afterward, if a 5 MPa stack pressure is used, uniform plating and stripping occurs at 0.075 mA/cm^2 (a low current) without any Li metal dendrite growth. (f) Verification with Nano-CT where no cracks were found between two plungers (Li metal is not visible by Nano-CT). (g) Even at a low stack pressure of 5 MPa, dendrite growth take place if the current density is more than 0.1 mA/cm^2. (h) If a 25 MPa stack pressure is kept, further dendrite growth takes place at a low current density of 0.075 mA/cm^2. (i) Cracks were found in Nano-CT, which are caused by Li metal dendrite growth. (j) High stack pressure of 75 MPa

https://dx.doi.org/10.1021/acs.chemrev.0c00101
Chem. Rev. XXXX, XXX, XXX−XXX

Figure 32. continued

will instantaneously mechanically short the cell without any applied current; confirmed with (k) nano-CT measurement where multiple cracks were found and the electrolyte pellet was fully broken. Reproduced with permission from ref 146. Copyright 2019 Wiley-VCH Verlag.

grain boundary of Al-LLZO whereas only Li was found at the Ga−LLZO interface.[304] The chemical species/composition at the interface could affect the mechanical behavior at the grain boundaries of LLZO, thus affecting the dendrite growth rate. Furthermore, their observation was similar with Pallab et al. as they found the preferable growth of dendrites at grain boundaries even though the grain boundary conductivity was 2 orders of magnitude less than bulk grains.[289] They calculated that induced stress (where the stress could be from external stack pressure or Li nucleation-induced pressure) changes electrochemical potential significantly, in turn locally increasing the current density at grain boundaries, promoting preferential Li deposition. As more Li is deposited, more stress is generated, increasing the deposition kinetics until ultimately the cell shorts.

5.4. Comparison of Anode Interfaces/Interphases between Liquid and Solid Electrolytes

Li metal is the ultimate anode choice (in both LE and SE systems) to achieve high energy density batteries. While sharing many similarities, the differences about existing problems and optimization requirements/strategies between the two systems are worth mentioning. A discussion of SEI on the Li surface in LEs and SEs will be compared from the perspective of SEI properties, coating strategies, dendrite growth, and research status. Our aim is that such a side-by-side comparison could potentially shed light on complementary effective strategies for ASSB design improvement.

5.4.1. Spontaneously Formed Interphases. Since Li/Li^+ has one of the most negative electrochemical potentials, Li metal is thermodynamically unstable in almost all organic solvents and SEs with high ionic conductivity. Therefore, a SEI will readily form on Li metal surfaces upon contact and under electrochemical conditions. In organic LEs, the SEI continuously evolves by electrolyte decomposition until its thickness exceeds that of the electron tunneling regime and solvent penetration. A passivating SEI layer is the key to enabling the operation of Li metal under a strong reductive environment by allowing ionic conduction while blocking electronic conduction.[24] The well-recognized SEI species formed in organic LEs, including lithium oxides (Li_2O), lithium fluoride (LiF), and lithium carbonates (Li_2CO_3, $ROCO_2Li$, and $RCOO_2Li$ (where R is an organic group related to the solvent)), are all electrical insulators.[305] For SEs, there are two types of SEI as previously discussed: the first type is ionically conductive but electronically insulating, which has similar thermodynamic and kinetic properties to LEs, and the second type contains both ionically and electronically conductive components. This second type of thermodynamically unstable SEI will continuously grow during battery operation, increasing the interfacial resistance.

In LE systems, it was previously widely accepted that continuous SEI formation during cycling causes low CE in Li metal batteries.[306] Recent advances, namely the introduction of the Titration Gas Chromatography (TGC) characterization method for batteries, allows for accurate quantification of Li metal failure products. It was found that inactive Li (isolated metallic Li) is the primary cause of capacity loss, while SEI formation only contributed a small portion of the total capacity loss.[307] Although both the SEI and the isolated metallic Li accumulate upon cycling, the amount of isolated metallic Li significantly dominates when the CE is around 90%. This quantitative result indicates that the continuous SEI formation does not directly contribute to most of the capacity loss, but rather the SEI's structure, components, spatial distribution, mechanical properties, and degree of homogeneity play roles on governing the morphology of the deposited Li, which then determines how much metallic Li will be trapped (and become electrochemically inactive). Moreover, the continuous formation of SEI consumes LE, leading to cell failure due to electrolyte depletion.[308] It is therefore particularly important to make the as-formed SEI reversible after a full cycle, but this solution remains elusive. So far, three types of spontaneously formed SEI structure models in different electrolytes have been reported: the Mosaic model[309] (heterogeneous distribution of SEI components), the Multitype model[246] (e.g., an outer Li_2O layer and inner amorphous layer) and the recently reported Monolithic model[310] (a homogeneous amorphous layer). Generally, a more homogeneous SEI (structure and components) will result in better cycling performance, indicating a correlation between SEI properties and cyclability. However, there is still a lack of direct and clear evidence to determine the cyclability of the SEI layers and in turn, how to enhance this characteristic.

5.4.2. Artificial Interfaces. In both LEs and SEs, using a thermodynamically stable coating layer, otherwise known as an artificial SEI, is commonly considered as an effective way to improve the cyclability of Li metal. This protective layer should be stable with Li metal to diminish side reactions and electrolyte decomposition, possess high ionic conductivity and minimal electronic conductivity, have strong mechanical properties to prevent dendrite propagation, and high elasticity to sustain volume expansion.[311,312] Apart from these properties, specific properties are required in LE and SE systems separately. For LEs, it is particularly important that the coating layer is pinhole-free to avoid liquid penetration; pinholes will defeat the purpose of the artificial SEI and allow for Li corrosion to take place. For SEs, the physical contact between Li metal and SE remains problematic, requiring the artificial SEI to provide conformal contact between the Li metal and SE to avoid small gaps and voids.

Xu et al. thoroughly summarized the recent progress of designing an artificial SEI for Li metal protection in LE systems, including a variety of coating methods (solution casting, doctor blading, spin coating, CVD, PVD, chemical pretreatment, etc.) and different materials (organics, inorganics and hybrid organic−inorganics).[312] Even though all of the reported strategies have shown improved electrochemical performance compared to bare Li, only a few of them could satisfy most of the requirements (especially pinhole-free) and achieve a CE higher than 99%. For instance, Liu et al. reported a double-layer artificial SEI made of nanodiamonds and graphene oxide with ultrastrong mechanical properties, which enhanced defect tolerance and promoted a uniform ion flux.[313] An average CE (over 10 cycles) for the DND-polymer electrodes was as high as 99.4% at 1 mA/cm^2 and 99.2% at 2 mA/cm^2 (with an areal capacity of 2 mAh/cm^2). Gu et al. used an electrochemical polishing method followed by galvanostatic plating pretreat-

https://dx.doi.org/10.1021/acs.chemrev.0c00101
Chem. Rev. XXXX, XXX, XXX−XXX

Table 2. Comparison of Properties Regarding the Li Metal Anode in Liquid Electrolyte and Solid Electrolyte Systems

	liquid electrolyte	solid electrolyte
spontaneously formed SEI	Li^+ conductive/e^- insulating	Li^+ conductive/e^- insulating sometimes e^- conductive
artificial SEI	Li^+ conductive/e^- insulating	Li^+ conductive/e^- insulating
	thermodynamically stable	thermodynamically stable
	high Young's modulus and elastic	high Young's modulus and elastic
	lithophilic	lithophilic
	pinhole-free (to avoid liquid penetration)	conformal contact with Li metal and SE
Li dendrite	no dendrite-caused short circuit	dendrite growth causes short circuit.
	morphology affected by 1. electrolyte, 2. current density, 3. temperature, 4. pressure	possibly affected by 1. current density, 2. stacking pressure causes Li creep, 3. grain boundary conductivity
cyclability	Coulombic efficiency up to 99.4% at moderate current density (0.5 mA/cm^2)	cyclable at very low current density (0.075 mA/cm^2) with optimized stacking pressure[146]
		cyclable up to 300 cycles with limited excess of electrolyte and Li metal[310]
current research status	to push the efficiency to >99.99%	to pursue better understanding of dendrite growth mechanism and avoid dendrite growth under normal operating conditions
	to quantitatively understand the failure mechanism	

ments to generate an ultrasmooth, inorganic−organic-inorganic multilayer SEI at alkali metal surfaces.[314] In 1 M LiFTSI in DME/DOL electrolyte without additives, they achieved an average CE of 99% (at 2 mA/cm^2 and 1 mAh/cm^2) for 200 cycles in Cu||Li coin cells.

5.4.3. Li Dendrites. In LEs, under normal operating conditions with moderate current density (whether in coin cells or pouch cells), sharp dendrites that cause direct cell short circuits are rarely observed.[315] The failure model of Li metal in LE cells has been proven to be the continuous formation of inactive Li that causes either electrolyte depletion or Li metal depletion.[316,317] In SEs, there is Li dendrite growth that causes cell shorting. The possible causes include the applied current density, the applied stack pressure (that can cause Li creep), and grain boundary conductivity.

Following classical crystal growth theory, Li deposition in LE is mostly governed by the chemical environment (solvent, salt, salt concentration, additives, etc.) and electrochemical conditions (current density etc.).[318] The morphology of the deposited Li is largely determined by the chemical composition, structure, and mechanical properties of the SEI layers, which in turn is determined by electrolyte properties. For instances, in carbonate-based electrolytes, the Li deposits exhibit a whisker/mossy-like morphology with a high electrode porosity; in other electrolytes such as high-concentration or localized high-concentration ether-based electrolytes, Li deposits are much denser with a large granule size of several μm. In ether-based electrolytes with the $LiNO_3$ additive, the Li deposits have a unique spherical morphology. Temperature and stack pressure have also been reported as important factors that influence the Li morphology. Wang et al. reported that Li particles grow larger at 60 °C compared at 20 °C with an average CE of 99.3% (in ether-based electrolyte).[319] Dahn et al. reported that when increasing the pouch cell stack pressure to 1200 kPa, the Li deposits become very closely packed and the cell cycling stability remarkably improved (50 cycles in an anode-free cell with almost no capacity drop using 0.6 M LiDFOB + 0.6 M $LiBF_4$ in FEC + DEC, 1:2 vol. ratio).[320] They ascribe that the increased pressure improves the cycling performance in two ways: (1) it helps to reduce the isolated metallic Li amount, and (2) it minimizes the Li surface area so that less active Li is consumed to form SEI (although the conclusion needs to be further investigated quantitatively).

In terms of research progress, Li metal cyclability in LE has made significant progress in recent years primarily due to the advancement of electrolytes, which not only prevented dendrite growth issues but also enabled a CE of up to 99%. Yet, a commercially viable Li metal battery with a cell-level energy density higher than 500 Wh/kg requires the Li metal cycling efficiency to be as high as 99.98% (to achieve 1000 cycles with 80% of capacity retention).[321] This requires future research to pursue more in-depth understanding of the failure mechanism and to quantitatively analyze the capacity loss. In SE systems, the field faces more challenging issues; recent progress has successfully made Li metal cyclable with optimized stacking pressure, but at a very low current density of 0.075 mA/cm^2.[146] In SEs, higher efficiency has not been discussed yet; there still a long way to go to achieve highly efficient Li cycling in SE under typical battery operating conditions. Research efforts urgently need to focus on the systematic understanding of the dendrite growth mechanism. For SEs, well-controlled and standardized experimental conditions are crucially needed so that appropriate comparisons can be made between reports (see Table 2).

6. ADVANCED CHARACTERIZATION TECHNIQUES

Engineering the interface requires a full understanding of the interfaces in ASSBs, including the composition and distribution of species present, electronic/ionic properties, and their evolution during cycling. As mentioned before, the buried nature of the interface brings much difficulty in deconvoluting, probing, and identifying chemical species. Thus, existing characterization tools must be adapted and new advanced techniques developed and customized to reach and probe the elusive interface. In this section, we will review the typical characterization tools widely used for solid-state interfaces, explain their merits and weaknesses, and suggest other potentially useful techniques, especially *in situ* methods.

6.1. Computation

First-principles calculations enable bypassing physical barriers to reveal atomic interactions at the interface. They are useful to estimate the thermodynamic stability and kinetic behavior. The electrochemical window of electrolytes and their stability with other ASSB components (cathode, anode, and coating) can be predicted as well as the corresponding reaction products, which have been proven to reasonably agree with some of the experimental measurements. The general principles behind the various first-principles approaches can be categorized into three approaches: Approach 1 is the fast diffusion of an alkali ion in a SE, Approach 2 is multispecies equilibrium between two

https://dx.doi.org/10.1021/acs.chemrev.0c00101
Chem. Rev. XXXX, XXX, XXX−XXX

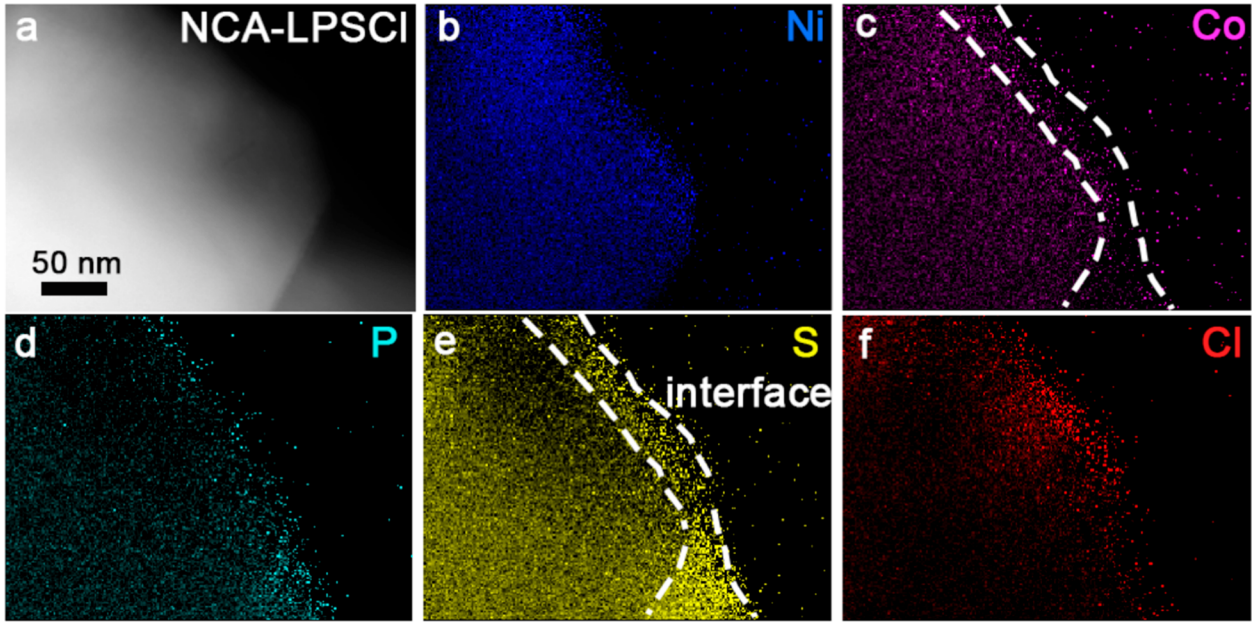

Figure 33. Cryo-STEM mapping of the NCA−LPSCl interface. Reproduced with permission from ref 52. Copyright 2019 American Chemical Society.

materials, and Approach 3 is explicit interface simulation by finite-temperature *ab initio* molecular dynamics (AIMD).[80] Approach 1 gives the predicted electrochemical window of various SEs, most of which are narrow and thus susceptible to decomposition when the operating voltage extends beyond this window. Approach 2 calculates the thermodynamic energy or the driving force/reaction pathways of two reacted materials and constructs their phase diagram as an indicator for their chemical stability or instability. Approach 3 provides a kinetic interface model and reveals the most realistic picture of interfacial reactivity. It should be noted that all three approaches have limitations and the best results are obtained by combining the predictions from all of them.

The largest benefit of computational evaluation is the high-throughput capability based on utilizing large-scale materials databases which allows for time-efficient screening of batches of interfaces. Mo and co-workers compared the electrochemical stability window of $Li_{10}GeP_2S_{12}$ (LGPS), garnet $Li_7La_3Zr_2O_{12}$ (LLZO), $Li_{0.33}La_{0.56}TiO_3$ (LLTO), NASICON-type $Li_{1.3}Al_{0.3}Ti_{1.7}(PO_4)_3$ (LATP), and LiPON, and found that garnet LLZO shows the lowest reduction potential of 0.05 V, while LATP has the highest oxidation potential of 4.31 V.[11,52] Most of these turn out to be thermodynamically unstable with $LiCoO_2$ (LCO), especially the sulfide-based electrolytes, which are neither chemically nor electrochemically stable. Coating the cathode with relatively inert materials helps to stabilize the interface and mitigate unwanted reactions. Xiao et al. employed a computational framework to evaluate and screen Li-containing materials as cathode coatings in terms of phase stability, electrochemical and chemical stability, and ionic conductivity. They pointed out that polyanionic oxide coatings offer the best combination of the aforementioned properties, their results show that these offer great promise for improved performance.[99] On the anode side, Zhu et al. studied the intrinsic thermodynamic stability of materials against Li metal as a function of cation and anion chemistry. They found that metallic and metalloid cations are usually reduced at low potentials and possibly form the detrimental MIEC interface, while nonmetal anions such as O, N, F, P, Cl, Br, and I are generally compatible with Li metal and form passivating interfaces. Notably, nitride anion chemistry has the highest stability against Li metal and nitrogen-rich interfaces can be made by using nitrogen-containing materials on the Li metal anode.[322]

Ultimately, computational results can provide essential predictions and guidelines for screening, designing, and matching materials to form a stable interface on both the cathode and anode sides. It is worth noting that although some of the calculated results have been proven to line up with experimental findings, computational methods are usually performed at relatively small cell sizes and short time scales, which are far from practical operating conditions. This requires experimental verification by various diagnostic tools with a wide detection range with regards to energy, spatial resolution, and temporal resolution.

6.2. Electron Microscopy (EM) Techniques

EM enables direct visualization of the interface at the nano- and microscale, which delivers important information on the morphology, structure, elemental distribution and electric potential by combining imaging, diffraction, and spectroscopy.[10,98,323] A prerequisite for EM is to prepare a thin (a few nm-thick) cross-section slice or lamella with the interface intact from the buried mixture. This requires delicate work by the focused ion beam (FIB).[324] The first cross-section observation was made by Brazier et al. on the $LiCoO_2/Li_2O-V_2O_5-SiO_2/SnO$ nanobattery, which showed the internal diffusion of Co, Si, and V at the cathode and anode interfaces respectively after multiple cycles.[324] Similarly, Sakuda et al. observed the mutual diffusion of Co, P, and S at the interface between $LiCoO_2$ and $Li_2S-P_2S_5$, over a region as thick as 50 nm. Notably, a Li_2SiO_3 coating on $LiCoO_2$ was shown to be effective in suppressing the Co-diffusion and reduce the interfacial layer to 30 nm in thickness.[10] The presence of such a thick interface would drastically increase the resistance to Li-ion transfer and charge transfer, resulting in an increased voltage hysteresis of the cell. Using quantitative electron holography, Yamamoto et al. were able to observe the potential distribution across $LiCoO_2/Li_{1+x+y}Al_yTi_{2-y}Si_xP_{3-x}O_{12}$ and found a steep potential drop and a

https://dx.doi.org/10.1021/acs.chemrev.0c00101
Chem. Rev. XXXX, XXX, XXX−XXX

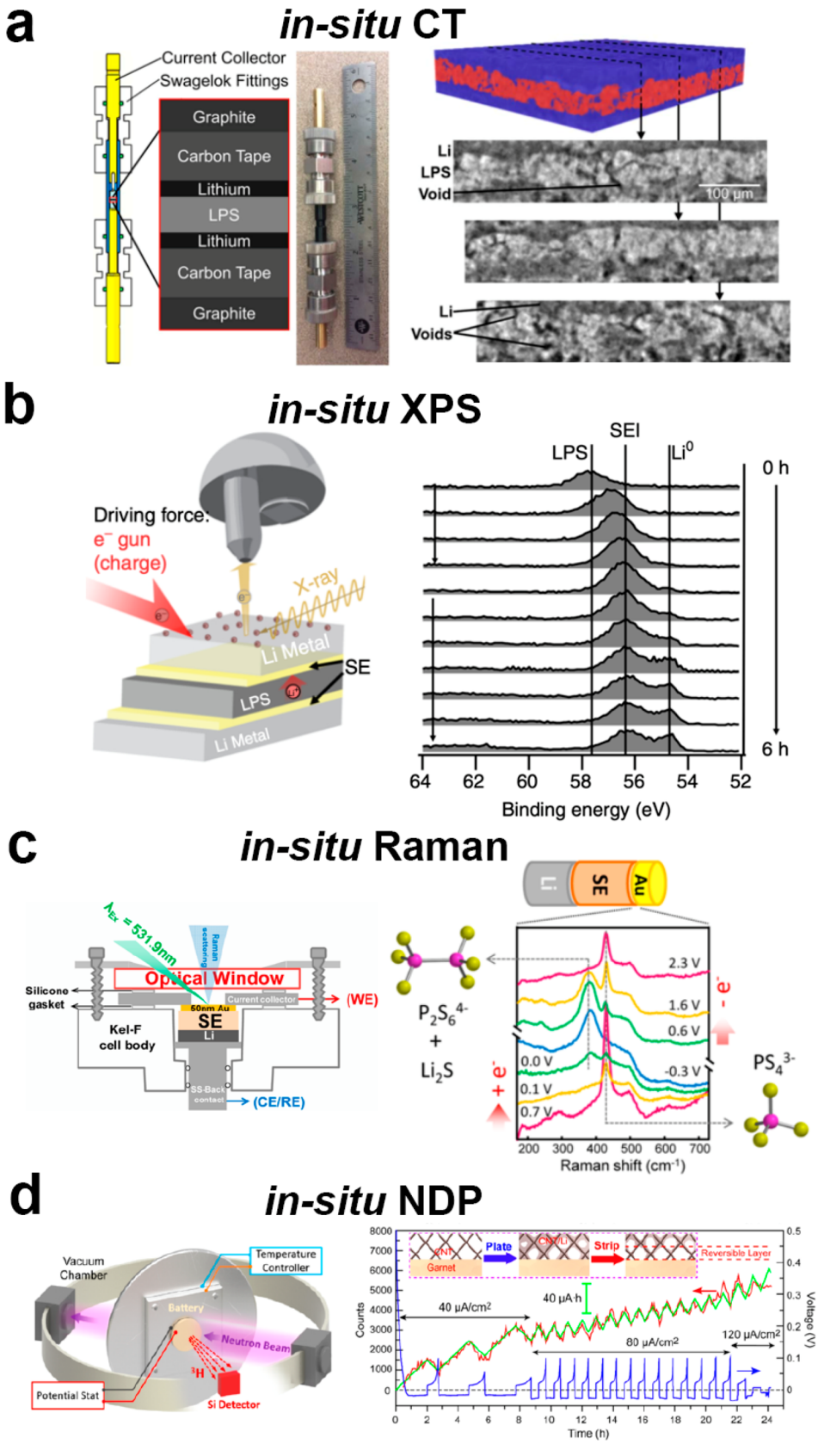

Figure 34. *In situ* characterization setup and results for interfacial diagnosis; (a) *in situ* CT.[329] Reproduced with permission from ref 329. Copyright 2018 IOP Publishing. (b) *In situ* XPS,[334] (c) *in situ* Raman. Reproduced with permission from ref 336. Copyright 2017 American Chemical Society. (d) *In situ* NDP Reproduced with permission from ref 340. Copyright 2017 American Chemical Society.

https://dx.doi.org/10.1021/acs.chemrev.0c00101
Chem. Rev. XXXX, XXX, XXX−XXX

gradually extended slope owing to the formation of an electrical double layer near the interface.[98]

Considering that *ex situ* experiments typically have prolonged time relaxation, potential air exposure, and other factors that could interfere or alter the sample properties, *in situ* observation is preferred and even necessary to retain a pristine interface while under evaluation. Wang et al. conducted *in situ* scanning transmission electron microscopy (STEM) coupled with electron energy loss spectroscopy (EELS) and uncovered the unique interfacial phenomena between $LiCoO_2$ and LiPON; this interface is composed of disordered Li_2O and CoO decomposed from $LiCoO_2$.[323]

It is worth mentioning that both SEs and Li metal are extremely sensitive to the beam used in the microscope, and cryogenic protection has been shown to be essential to minimize any potential beam damage and to preserve the intrinsic sample properties.[325] Lee et al. demonstrated the capability of cryo-FIB to prepare a relatively clean lamella for TEM and also carried out STEM at cryogenic temperatures (cryo-STEM) on the NCA−LPSCl interface after cycling (Figure 33).[326] Co and S were shown to segregate at the NCA−LPSCl interface and a $LiNbO_3$ coating inhibited this reaction between NCA and LPSCl.[327] For the future exploration by EM, combining cryogenic protection and *in situ* observation should be considered to avoid any potential sample damage during simultaneous probing of dynamic interfacial evolution at the nano- or even atomic-scale.

6.3. Transmission X-ray Microscopy (TXM), X-ray Computed Tomography (CT), Time-of-Flight Secondary Ion Mass Spectrometry (TOF-SIMS), and Atomic Force Microscopy (AFM)

While EM techniques are sensitive to the localized fine structure, a larger picture of the interface requires looking at the microstructure; this is vital because of the heterogeneous nature of the interface. To achieve this, other microscopic techniques with various capabilities are complementary and indispensable, such as TXM, CT, AFM, and TOF-SIMS.

On the basis of X-ray absorption, TXM and CT can provide three-dimensional (3D) reconstructed volumes of interfaces at μm resolutions. With these techniques, Harry et al. disclosed the presence of heterogeneities in the Li/polymer (polystyrene-block-poly(ethylene oxide))/Li cell and found Li dendrites not only at the Li−polymer interface but also in the subsurface of the Li electrode; the latter is a surprising and important find.[328] The formation and propagation of Li metal within the Li_3PS_4 SE was also revealed by Seitzman et al. using *in situ* synchrotron-based X-ray tomography (Figure 34a).[329] Both TXM and CT are nondestructive and enable the determination of the porosity, tortuosity, and even elemental heterogeneities of the interface. One of the challenges is the difficulty in differentiating Li, a light element, and voids, since both have very low X-ray absorption and thus a low image contrast.

This issue can be addressed by TOF-SIMS and the newly developed windowless energy-dispersive X-ray spectroscopy (EDS). Windowless EDS is sufficiently sensitive to observe the 54 eV Li Kα X-ray, which is very intense for pure Li metal but much weaker for Li compounds.[329] While EDS offers 2D elemental distribution, TOF-SIMS enables 3D elemental maps, as demonstrated by Park et al. with the $LiCoO_2$−LLZO interface.[90] Minor cross-diffusion occurs at the interface, where Co diffuses into LLZO and Zr/La diffuses into $LiCoO_2$.[90]

Charge transfer across the interface can be estimated by AFM. AFM is useful to measure the potential image of the cross-sectional interface using peak force tapping mode. The average potential of $Li_{1.4}Al_{0.4}Ti_{1.6}(PO_4)_3$ (LATP)-coated Li-$Ni_{0.6}Co_{0.2}Mn_{0.2}O_2$ (L-NCM) was determined to be 0.214 V, lower than that of bare NCM, confirming a weakened space-charge layer (SCL) by introducing a Li-ion-conducting buffer layer.[330] Compared with other technologies for SCL detection, AFM interfacial potential measurements exhibit unique advantages such as flexible operation, facile sample preparation, and high sensitivity to potential fluctuations.[92,331,332]

6.4. X-ray Absorption Spectroscopy (XAS), X-ray Photoelectron Spectroscopy (XPS), and Raman Spectroscopy

Chemical and electrochemical reactions that occur at the interface could influence the electronic and band structures of the interfacial materials. Probing the changes in these structures will help to understand charge transfer, the cleavage/formation of chemical bonds, and phase transitions involved at the interface. In this regard, XAS, XPS, and Raman spectroscopies are widely employed.

Both XAS and XPS are known for their sensitivity to the electronic structure, with the difference being in the detectable depth: the former can detect about 100 nm while the latter is less than 10 nm. Therefore, XAS is regarded as a bulk technique while XPS is regarded as a surface technique. Depending on the interfacial thickness, one or the other could be applied, or possibly both could be used to complement each other. For an example, Hakari et al. revealed the reversible association and dissociation of S−S bonds in Li_3PS_4 by XAS and XPS, which contributes to charge compensation during charge/discharge processes.[69] Because of its large probing distance, in situ XAS may be not suitable to investigate the dynamic formation and evolution of the interface, but *in situ* XPS could be doable: Wenzel et al. suggested using the internal argon ion gun of the instrument for sputtering of a Li metal target to deposit a thin metal film on the electrolyte sample surface immediately followed by analysis.[333] Wood et al. applied bias by an electron gun to drive Li^+ migration and extracted valence electrons by ultraviolet light to move back the Li^+ while XPS measurements monitored changes at the exposed surface (Figure 34b).[334] With this method, they discovered the multilayered configuration ($Li^0/Li_2O/Li_3P/Li_2S/Li_3PS_4$) at the Li−$Li_3PS_4$ interface.[334]

Raman spectroscopy is also a surface-sensitive tool but with a much higher spatial resolution (~1 μm) than XPS (~50 μm). Since the Raman signal originates from lattice vibrations in the structure, the spectral change is highly dependent on changes of the local structure and coordination. For example, Raman can distinguish between cubic and tetragonal $Li_7LaZr_2O_{12}$ (LLZO), Li_3PS_4, and $Li_4P_2S_6$; both exhibit partial interconversion at the interface with Li metal (Figure 34c).[335,336] The spatial distribution of two different phases can be further identified by Raman mapping rather than SEM-EDS, highlighting its advantage in probing phase heterogeneity.[335,337]

6.5. Nuclear Magnetic Resonance (NMR) and Electrochemical Impedance Spectroscopy (EIS)

Charge transfer resistance is most often estimated by EIS. The impedance spectrum usually can be divided into a high-frequency region (>1 MHz), a midfrequency region (1 kHz ~ 100 Hz) and a low-frequency region (~1 Hz), corresponding to the resistance contributions from the bulk electrolyte, charge transfer at the interface, and Warburg diffusion, respectively.[338] Time-resolved EIS allows the monitoring of the interfacial resistance change during charge and discharge, a good indicator

https://dx.doi.org/10.1021/acs.chemrev.0c00101
Chem. Rev. XXXX, XXX, XXX−XXX

to trace Li^+ diffusion and charge transfer across the interface.[217,338] For the $LiCoO_2/Li_{10}GeP_2S_{12}/LiIn$ solid-state cell, Zhang et al. found that there is a larger resistance contribution and kinetic hindrance at the metal side rather than the cathode side during cycling.[338] On the basis of the spectroscopic analysis with proper models, the chemical diffusion coefficient of Li can be obtained as well as the interface thickness.[217] On the other hand, the precise interpretation of the impedance spectra requires accurate models. This may be more straightforward for well-defined thin-film ASSBs but difficult or even impossible in the complex morphologies of conventional ASSBs, where the influence of porosity, tortuosity, grain boundaries, physical contact, and other potential factors from electrodes and electrolytes should be taken into account.

NMR spectroscopy has been shown to offer unique and complementary information to EIS due to its high sensitivity to Li^+ mobility in bulk battery materials and its selectivity for charge transfer over phase boundaries by probing spontaneous Li^+ exchange.[171] This extends the Li^+ diffusion time scale from microseconds (with spin relaxation experiments) up to seconds (with exchange NMR) depending on the NMR characteristics of the materials. Using exchange NMR, Yu et al. found the self-diffusion coefficient for $Li_6PS_5Cl–Li_2S$ exchange (1×10^{-11} cm^2/s) is several orders of magnitude smaller than the Li_6PS_5Cl bulk (9×10^{-7} cm^2/s), suggesting that crossing the interface presents a major bottleneck for Li^+ transport in ASSBs.[172] This problem can be mitigated by making the electrode particles nanosized to establish intimate contact with the SE.[171]

Yu et al. compared the conductivity results from DFT-MD calculations, impedance spectroscopy, and NMR spin–lattice relaxation (SLR) and exchange experiments.[172] This covers Li^+ transport over an extremely wide time scale, ranging from 10^{-12} seconds, representing intercage transitions, up to approximately 0.1 s, representing exchange between the SE and electrode. This range allows for several benefits: based on simplified force field potentials or static nudged elastic band calculation, DFT-based MD simulations can be used to predict Li^+ kinetics for fast ionic-conductive materials resulting in good agreement with the NMR SLR experiments, which allows for insights into the diffusion mechanism at the atomic-scale. NMR SLR experiments can probe up to a few Li^+ transitions whereas EIS probes transport over a longer length scale, typically on the order of tens of nm. As a result, RT conductivity determined by EIS is smaller than the bulk conductivity measured by NMR SLR experiments since the former probes both the bulk and grain boundary Li^+ diffusion. NMR exchange experiments make it possible to characterize the equilibrium exchange of Li-ions over the electrolyte-electrode interface, which is the dominant factor responsible for the restricted power performance of current ASSBs.

6.6. Neutron Depth Profiling (NDP)

Because of the high sensitivity of neutrons to light elements such as Li and Na, NDP is a powerful tool to analyze Li distribution and transport in ASSBs. After the reaction $^6Li + n \rightarrow {}^4He$ (2055 keV) + ^3H (2727 keV) takes place, the generated particles lose energy to the matrix at a specified rate, which can be used to identify the initial location of the reaction and the counts indicate the abundance of Li at the corresponding depth.[339] Both Wang et al. and Han et al. established *in situ* NDP to monitor the Li plating-stripping process at the surface of electrolyte and the substrate (Figure 34d).[340,341] The counts within the surface region show a linear dependence on the amount of Li transfer, which increases during Li plating and decreases during Li stripping.[340] Compared with LiPON, Han et al. visualized the direct deposition of Li inside bulk LLZO and Li_3PS_4 and suggested that the high electronic conductivity of LLZO and Li_3PS_4 is probably the root cause for dendrite formation in these SEs.[341]

7. SUMMARY AND PERSPECTIVE

In summary, the recent research progress on interfaces and interphases in all-solid-state batteries, as well as the remaining challenges for the field, have been reviewed thoroughly. Most of the highly conductive SEs (halides, sulfides, oxides, and nitrides) possess a low electrochemical oxidation stability, resulting in the oxidation of SE to form a CEI. On the other hand, except for a few binary SEs (Li_2S, Li_3P, Li_3N, and LiF etc.), most SEs are not stable with Li metal and thus form a SEI. SE decomposition occurs on the electronically conductive surface, such as electrode materials, conductive carbon, and current collectors. The extent of decomposition depends on the chemical/physical properties of SEs, the volume/weight percentage of electrode or carbonaceous materials in the electrode composite, and the operating voltage of ASSBs. If the SEI and CEI form irreversibly and consists of ionically insulating materials (relative to SEs), irreversible impedance growth will occur during the first cycle.

Additional impedance in ASSBs arises from interfacial chemical reactions between electrodes and SEs. It has been realized the cathode charge transfer resistance is the bottleneck for high-power ASSBs. A thermodynamically unstable interface is formed when SEs are coupled with high-voltage oxide cathodes, resulting in the formation of unwanted interfacial side products which degrades the cathode, lowers capacity, and reduces the electrochemical efficiency of ASSBs. Although oxide-based SEs are kinetically stable with oxide cathodes, their interface suffers from poor wettability due to the high Young's modulus (stiffness) of the oxide SEs. Therefore, for oxide SEs, high temperature annealing is required to chemically wet the interface which can simultaneously accelerate undesired chemical reactions at a previously kinetically stable interface which results in high interface impedance. The kinetics of interfacial reactions is also more pronounced at the charged state than the discharged state. Electronically insulating, ionically conductive, and thin coating materials, applied to kinetically protect the interface, improve the rate performance of ASSBs to levels competitive with conventional LE-based batteries.

The mechanical incompatibility at the electrode–SE interface is another crucial problem in ASSBs. Continuous volume change of the cathode and anode (during charging/discharging) induces stress at the interface, and as a result, delamination of either the electrode materials or the protective coating layer occurs. This is accompanied by the formation of cracks/voids at the interface which leads to cycling deterioration. Such cracks/voids expose new electrode surfaces to the SE which react chemically and electrochemically, further lowering cyclic efficiency and capacity. With cracks and voids, Li stripping will then occur on selective contact surfaces, creating voids in one electrode, while Li metal plating in a limited area will increase localized current density, generating hot spots for dendrite growth. A lithophilic coating layer or melted Li metal treatment on LLZO have been applied to minimize Li/LLZO interstitial gaps to promote homogeneous Li metal deposition.

In addition, the Li–SE interface can be also mechanically wetted through Li metal creeping by applying uniaxial stack pressure. Although a high stack pressure is required to better wet the interface, a lower stack pressure is preferred for long cycling.

https://dx.doi.org/10.1021/acs.chemrev.0c00101
Chem. Rev. XXXX, XXX, XXX–XXX

The mechanical properties of the SE are also quite important with regards to Li dendrite growth (according to the Monroe–Newman criteria, the sheer modulus of the SE must be twice that of Li for dendrite prevention). Although oxide-based SEs satisfy these criteria, dendrite growth is still noticeable at current densities above 0.5 mA/cm^2.

Despite the significant progress so far in ASSBs, many challenges remain in terms of the SE, electrode materials, and their interfaces.

I. Although the current ASSB research trend involves development of new highly ionically conductive SEs to compete with LE conductivity, unfortunately, the electrode–SE charge transfer resistance is not considered while designing new SEs. For example, LGPS and LSiPSCl, which have ionic conductivities exceeding those of LEs, are not stable with Li metal, thus exhibiting the lowest CE when using a high voltage cathode. This ultimately makes the electrolytes impractical. Although the incorporation of I, Br, or Se increases the ionic conductivity of SEs, they also cannot be used with high-voltage oxide cathodes as there are multiple anionic redox processes during charging, which results in a thicker, irreversible SEI and high interfacial resistance. Therefore, compositional screening of SEs based on their interfacial properties with specific electrodes must be prioritized and carried out before considering conductivity and ultimately experimental synthesis.

II. Low capacity, poor CE, high polarization, and capacity fade of ASSBs originate from sluggish interfacial charge transfer kinetics, which results from chemical reactions, electrochemical decomposition, and loss of interfacial mechanical integrity. However, there is no quantitative estimation of the participation of each of these components on the sluggish kinetic behavior. Quantitative estimation will help to design better SEs, identify suitable cathodes and allow for an optimal composite electrode composition for high-efficiency cycling.

III. Coatings on high-voltage oxide cathodes that are thermodynamically stable with both the SE and cathode are believed to be electrochemically passivated under high voltage due to sluggish kinetics. However, most ASSBs are reported with limited cycling where kinetic passivation dominates. Long-term cycling stability (>500 cycles) of the coating layer has not been studied so far. In addition, high-temperature rapid cycling could help to exacerbate any side reactions experienced by the coating layer to check the stability in a shorter time. Moreover, it is difficult to isolate the coating layer from bulk ASSBs for analysis and characterization.

IV. The mechanical properties of all of the ASSB components are the most crucial parameters for effective cycling. This is especially important for the soft Li metal anode as Li metal dendrite growth and Li plating/stripping kinetics are highly dependent on mechanical compatibility at the interface. A lithophilic coating layer on Li metal (with oxide-based SEs) stabilizes the Li–SE interface for dendrite-free Li deposition (but at low current density). However, the mechanical stability of such a lithophilic coating layer over long-term cycling and with high capacity (4 mAh/cm^2) Li metal deposition is still questionable. Moreover, the mechanical properties of newly formed interfaces along with their chemical structure and their effects on battery cycling need to be investigated. Precise mechanical and chemical modeling of the interface with/without electric field (static and dynamic changes) need to be analyzed. Moreover, the mechanical stress of ASSBs can propagate over a long distance. For example, thick Li metal deposition on the anode induces stress, which can propagate through the SE to the cathode composite, affecting the chemical and mechanical integrity of the cathode composite during cycling. Full cell-level stress characterization will be necessary and is more relevant rather than characterization of individual components in the ASSB.

V. A full understanding of the interfacial properties in ASSBs requires using various characterization tools to cover a wide range of spatial and temporal scales. The spatial scale includes phenomena such as charge transfer, ion diffusion, the space charge layer, phase transitions, grain boundaries, and physical contact, while the time scale includes charge transfer, ion transport, exchanges between the electrolyte and electrode, and dynamic interface evolution as a function of the state of charge. *Ex situ* and *in situ* experiments should be combined to isolate and identify different interfacial components. Specifically, *in situ* or operando experiments are highly encouraged to monitor real-time interfacial changes while simultaneously avoiding potential contaminations and artifacts that can be present in *ex situ* experiments. Because of the fragile nature of the interface, SEs, and Li metal, cryogenic protection may be needed to stabilize the samples to minimize potential beam damage. In addition, it is important to develop and customize new techniques with integrated functions to enable information acquisition about the structure, composition, and kinetics. Both computation and experiments require high-throughput screening, diagnosis, and interfacial design for ASSBs.

AUTHOR INFORMATION

Corresponding Authors

Ying Shirley Meng – *Department of NanoEngineering, University of California San Diego, La Jolla, California 92093, United States;* orcid.org/0000-0001-8936-8845; Email: shirleymeng@ucsd.edu

Xuefeng Wang – *Department of NanoEngineering, University of California San Diego, La Jolla, California 92093, United States; School of Physical Sciences, University of Chinese Academy of Sciences; Laboratory for Advanced Materials & Electron Microscopy, Institute of Physics, Chinese Academy of Sciences, Beijing 100190, China;* orcid.org/0000-0001-9666-8942; Email: wxf@iphy.ac.cn

Abhik Banerjee – *Department of NanoEngineering, University of California San Diego, La Jolla, California 92093, United States; Research Institute for Sustainable Energy (RISE), TCG Centres for Research and Education in Science and Technology (TCG CREST), Kolkata 700091, India*; Email: abhik.banerjee@tcgcrest.org

Authors

Chengcheng Fang – *Department of NanoEngineering, University of California San Diego, La Jolla, California 92093, United States*

Erik A. Wu – *Department of NanoEngineering, University of California San Diego, La Jolla, California 92093, United States*

https://dx.doi.org/10.1021/acs.chemrev.0c00101
Chem. Rev. XXXX, XXX, XXX–XXX

Complete contact information is available at:
https://pubs.acs.org/10.1021/acs.chemrev.0c00101

Author Contributions

[⊥]AB and XW are cofirst authors, who made equal contributions to the major content of the article.

Notes

The authors declare no competing financial interest.

Biographies

Abhik Banerjee currently holds position of team leader of Research Institute of Sustainable Energy (RISE) under TCG CREST. He received his BSc and MSc degrees in chemistry from the University of Calcutta, India. He earned his PhD degree in 2015 from National Chemical Laboratory, India. He was then a postdoctoral scholar at Ulsan National Institute of Science and Technology, South Korea and University of California, San Diego (UCSD). His research interests include the design principles and interfacial charge-transfer limitations of solid-state electrolytes for Li and Na-ion batteries. Banerjee can be reached by email at abhik.banerjee@tcgcrest.org.

Xuefeng Wang is an Associate Professor in Institute of Physics, Chinese Academy of Sciences. He received his PhD from the Institute of Physics, Chinese Academy of Sciences in 2015, after which he worked as a postdoc research fellow in University of California San Diego. His research interest includes structural and mechanism exploration on energy-storage materials by cryogenic electron microscopies (Cryo-EM) and other advanced techniques including Li-ion batteries, Li metal, solid-state batteries, Li−O_2, and other metal batteries.

Chengcheng Fang is currently a postdoctoral fellow in the Department of NanoEngineering at University of California San Diego (UCSD), working with Prof. Shirley Meng. She received her BS from Zhejiang University and PhD from UCSD both in Materials Science and Engineering. She obtained her MPhil degree in Innovative Technology Leadership from Hong Kong University of Science and Technology. Her research focuses on developing multiscale quantitative characterization tools and designing advanced materials and manufacturing methods for high-performance energy storage. She was awarded the Materials Research Society Graduate Student Award in 2019.

Erik A. Wu is now a PhD candidate in Nanoengineering at the University of California, San Diego. He previously obtained his Bachelor's degree in Materials Science and Engineering in 2011 from the University of California, Berkeley. His research focuses on the synthesis, evaluation, and testing of novel compounds for sodium solid-state batteries toward stable and longer-life batteries.

Dr. Y. Shirley Meng received her PhD in Advance Materials for Micro & Nano Systems from the Singapore-MIT Alliance in 2005, after which she worked as a postdoc research fellow and became a research scientist at MIT. Shirley currently holds the Zable Endowed Chair Professor in Energy Technologies and is Professor of NanoEngineering and Materials Science, University of California San Diego (UCSD). She is the founding Director of Sustainable Power and Energy Center (http://spec.ucsd.edu). Shirley received the National Science Foundation (NSF) CAREER award in 2011, UCSD Chancellor's Interdisciplinary Collaboratories Award in 2013, Science Award in Electrochemistry by BASF and Volkswagen in 2014, C.W. Tobias Young Investigator Award of the Electrochemical Society (2016), IUMRS-Singapore Young Scientist Research Award (2017), International Coalition for Energy Storage and Innovation (ICESI) Inaugural Young Career Award (2018), American Chemical Society ACS Applied Materials & Interfaces Young Investigator Award (2018), and was a finalist for the Blavatnik National Award (2018). Her research group, Laboratory for Energy Storage and Conversion (LESC), focuses on functional nano- and microscale materials for energy storage and conversion. The more recent programs include the design, synthesis, processing, and operando characterization of energy storage materials in advanced rechargeable batteries; new intercalation materials for sodium-ion batteries; and advanced flow batteries for grids large scale storage. Shirley is the author and coauthor of more than 200 peer-reviewed journal articles, 2 book chapters, and 6 patents. She serves on the executive committee for battery division at the Electrochemical Society, and she is the Editor-in-Chief for MRS Energy & Sustainability.

ACKNOWLEDGMENTS

This work was financially supported by the LG Chem through the Battery Innovation Contest (BIC) program as well as the Energy & Biosciences Institute through the EBI-Shell program. YSM and CF acknowledge partial funding from U.S. Department of Energy, Office of Basic Energy Sciences, under Award No. DE-SC0002357 (program manager Dr. Jane Zhu).

ABBREVIATIONS

AB	Acetylene Black
AFM	Atomic Force Microscopy
AIMD	*Ab Initio* Molecular Dynamics
ALD	Atomic layer deposition
ASSBs	All-Solid-State Batteries
CCD	Critical Current Density
CE	Coulombic Efficiency
CEI	Cathode Electrolyte Interphase
CT	X-ray Computed Tomography
CV	Cyclic Voltammetry
DFT	Density Functional Theory
EELS	Electron Energy Loss Spectroscopy
EIS	Electrochemical Impedance Spectroscopy
FIB	Focused Ion Beam
HOMO	Highest Occupied Molecular Orbital
LATP	$Li_{1.3}Al_{0.3}Ti_{1.7}(PO_4)_3$
LCO	$LiCoO_2$
LEs	Liquid Electrolytes
LFP	$LiFePO_4$
LGPS	$Li_{10}GeP_2S_{12}$
LLTO	$Li_{0.33}La_{0.56}TiO_3$
LLZO	$Li_7La_3Zr_2O_{12}$
LNMO	$LiNi_{0.5}Mn_{1.5}O_4$
LPS	Li_3PS_4
LPSCl	Li_6PS_5Cl
LUMO	Lowest Unoccupied Molecular Orbital
MIEC	Mixed Ionic- and Electronic-Conducting
MLD	Molecule Layer Deposition
NAS	Na_3SbS_4
NDP	Neutron Depth Profiling
NMC	$LiNi_xMn_yCo_{1-x-y}O_2$
NMR	Nuclear Magnetic Resonance
PLD	Pulsed Laser Deposition
RT	Room-temperature
SEs	Solid Electrolytes
SEI	Solid−Electrolyte Interphase
SLR	Spin-Lattice Relaxation
STEM	Scanning Transmission Electron Microscopy
TEM	Transmission Electron Microscopy
TOF-SIMS	Time-of-Flight Secondary Ion Mass Spectrometry
TXM	Transmission X-ray Microscopy
VGCF	Vapor-Grown Carbon Fibers

https://dx.doi.org/10.1021/acs.chemrev.0c00101
Chem. Rev. XXXX, XXX, XXX−XXX

XAS X-ray Absorption Spectroscopy
XPS X-ray Photoelectron Spectroscopy

REFERENCES

(1) Gao, Z.; Sun, H.; Fu, L.; Ye, F.; Zhang, Y.; Luo, W.; Huang, Y. Promises, Challenges, and Recent Progress of Inorganic Solid-State Electrolytes for All-Solid-State Lithium Batteries. *Adv. Mater.* **2018**, *30*, 1705702−1705729.

(2) Manthiram, A.; Yu, X.; Wang, S. Lithium Battery Chemistries Enabled by Solid-State Electrolytes. *Nature Reviews Materials* **2017**, *2*, 16103−16119.

(3) Wang, Y.; Richards, W. D.; Ong, S. P.; Miara, L. J.; Kim, J. C.; Mo, Y.; Ceder, G. Design Principles for Solid-State Lithium Superionic Conductors. *Nat. Mater.* **2015**, *14*, 1026−1031.

(4) Mizuno, F.; Hayashi, A.; Tadanaga, K.; Tatsumisago, M. New, Highly Ion-Conductive Crystals Precipitated from Li2S−P2S5 Glasses. *Adv. Mater.* **2005**, *17*, 918−921.

(5) Kamaya, N.; Homma, K.; Yamakawa, Y.; Hirayama, M.; Kanno, R.; Yonemura, M.; Kamiyama, T.; Kato, Y.; Hama, S.; Kawamoto, K.; et al. A Lithium Superionic Conductor. *Nat. Mater.* **2011**, *10*, 682−686.

(6) Kato, Y.; Hori, S.; Saito, T.; Suzuki, K.; Hirayama, M.; Mitsui, A.; Yonemura, M.; Iba, H.; Kanno, R. High-Power All-Solid-State Batteries Using Sulfide Superionic Conductors. *Nature Energy* **2016**, *1*, 16030−16037.

(7) Xu, L.; Tang, S.; Cheng, Y.; Wang, K.; Liang, J.; Liu, C.; Cao, Y.-C.; Wei, F.; Mai, L. Interfaces in Solid-State Lithium Batteries. *Joule* **2018**, *2*, 1991−2015.

(8) Han, F. D.; Zhu, Y. Z.; He, X. F.; Mo, Y. F.; Wang, C. S. Electrochemical Stability of Li10gep2s12 and Li7la3zr2o12 Solid Electrolytes. *Adv. Energy Mater.* **2016**, *6*, 1501590−1501599.

(9) Takada, K.; Ohta, N.; Zhang, L.; Fukuda, K.; Sakaguchi, I.; Ma, R.; Osada, M.; Sasaki, T. Interfacial Modification for High-Power Solid-State Lithium Batteries. *Solid State Ionics* **2008**, *179*, 1333−1337.

(10) Sakuda, A.; Hayashi, A.; Tatsumisago, M. Interfacial Observation between Licoo2 Electrode and Li2S−P2S5 Solid Electrolytes of All-Solid-State Lithium Secondary Batteries Using Transmission Electron Microscopy. *Chem. Mater.* **2010**, *22*, 949−956.

(11) Zhu, Y.; He, X.; Mo, Y. First Principles Study on Electrochemical and Chemical Stability of Solid Electrolyte−Electrode Interfaces in All-Solid-State Li-Ion Batteries. *J. Mater. Chem. A* **2016**, *4*, 3253−3266.

(12) Haruyama, J.; Sodeyama, K.; Tateyama, Y. Cation Mixing Properties toward Co Diffusion at the LiCoO2 Cathode/Sulfide Electrolyte Interface in a Solid-State Battery. *ACS Appl. Mater. Interfaces* **2017**, *9*, 286−292.

(13) Wang, C.; Fu, K.; Kammampata, S. P.; McOwen, D. W.; Samson, A. J.; Zhang, L.; Hitz, G. T.; Nolan, A. M.; Wachsman, E. D.; Mo, Y. Garnet-Type Solid-State Electrolytes: Materials, Interfaces, and Batteries. *Chem. Rev.* **2020**, *120*, 4257.

(14) Wolfenstine, J.; Allen, J. L.; Sakamoto, J.; Siegel, D. J.; Choe, H. Mechanical Behavior of Li-Ion-Conducting Crystalline Oxide-Based Solid Electrolytes: A Brief Review. *Ionics* **2018**, *24*, 1271−1276.

(15) Bi, Z.; Zhao, N.; Ma, L.; Fu, Z.; Xu, F.; Wang, C.; Guo, X. Interface Engineering on Cathode Side for Solid Garnet Batteries. *Chem. Eng. J.* **2020**, *387*, 124089−112095.

(16) Zhao, N.; Khokhar, W.; Bi, Z.; Shi, C.; Guo, X.; Fan, L.-Z.; Nan, C.-W. Solid Garnet Batteries. *Joule* **2019**, *3*, 1190−1199.

(17) Zhao, Q.; Stalin, S.; Zhao, C.-Z.; Archer, L. A. Designing Solid-State Electrolytes for Safe, Energy-Dense Batteries. *Nature Reviews Materials* **2020**, *5*, 229−252.

(18) Li, S.; Zhang, S.-Q.; Shen, L.; Liu, Q.; Ma, J.-B.; Lv, W.; He, Y.-B.; Yang, Q.-H. Progress and Perspective of Ceramic/Polymer Composite Solid Electrolytes for Lithium Batteries. *Advanced Science* **2020**, *7*, 1903088−1903110.

(19) Lopez, J.; Mackanic, D. G.; Cui, Y.; Bao, Z. Designing Polymers for Advanced Battery Chemistries. *Nature Reviews Materials* **2019**, *4*, 312−330.

(20) Zhang, H.; Armand, M.; Rojo, T. Editors' Choice—Review—Innovative Polymeric Materials for Better Rechargeable Batteries: Strategies from Cic Energigune. *J. Electrochem. Soc.* **2019**, *166*, A679−A686.

(21) Goodenough, J. B.; Kim, Y. Challenges for Rechargeable Li Batteries. *Chem. Mater.* **2010**, *22*, 587−603.

(22) Moeremans, B.; Cheng, H.-W.; Merola, C.; Hu, Q.; Oezaslan, M.; Safari, M.; Van Bael, M. K.; Hardy, A.; Valtiner, M.; Renner, F. U. In Situ Mechanical Analysis of the Nanoscopic Solid Electrolyte Interphase on Anodes of Li-Ion Batteries. *Advanced Science* **2019**, *6*, 1900190.

(23) Bedrov, D.; Borodin, O.; Hooper, J. B. Li+ Transport and Mechanical Properties of Model Solid Electrolyte Interphases (SEI): Insight from Atomistic Molecular Dynamics Simulations. *J. Phys. Chem. C* **2017**, *121*, 16098−16109.

(24) Peled, E.; Menkin, S. Review—Sei: Past, Present and Future. *J. Electrochem. Soc.* **2017**, *164*, A1703−A1719.

(25) Horstmann, B.; Single, F.; Latz, A. Review on Multi-Scale Models of Solid-Electrolyte Interphase Formation. *Current Opinion in Electrochemistry* **2019**, *13*, 61−69.

(26) Verma, P.; Maire, P.; Novák, P. A Review of the Features and Analyses of the Solid Electrolyte Interphase in Li-Ion Batteries. *Electrochim. Acta* **2010**, *55*, 6332−6341.

(27) Wang, A.; Kadam, S.; Li, H.; Shi, S.; Qi, Y. Review on Modeling of the Anode Solid Electrolyte Interphase (SEI) for Lithium-Ion Batteries. *npj Computational Materials* **2018**, *4*, 15−41.

(28) Cannarella, J.; Arnold, C. B. Stress Evolution and Capacity Fade in Constrained Lithium-Ion Pouch Cells. *J. Power Sources* **2014**, *245*, 745−751.

(29) Baggetto, L.; Oudenhoven, J. F. M.; van Dongen, T.; Klootwijk, J. H.; Mulder, M.; Niessen, R. A. H.; de Croon, M. H. J. M.; Notten, P. H. L. On the Electrochemistry of an Anode Stack for All-Solid-State 3d-Integrated Batteries. *J. Power Sources* **2009**, *189*, 402−410.

(30) Richards, W. D.; Miara, L. J.; Wang, Y.; Kim, J. C.; Ceder, G. Interface Stability in Solid-State Batteries. *Chem. Mater.* **2016**, *28*, 266−273.

(31) Ong, S. P.; Wang, L.; Kang, B.; Ceder, G. Li−Fe−P−O2 Phase Diagram from First Principles Calculations. *Chem. Mater.* **2008**, *20*, 1798−1807.

(32) Han, F.; Gao, T.; Zhu, Y.; Gaskell, K. J.; Wang, C. A Battery Made from a Single Material. *Adv. Mater.* **2015**, *27*, 3473−3483.

(33) Chen, C. H.; Amine, K. Ionic Conductivity, Lithium Insertion and Extraction of Lanthanum Lithium Titanate. *Solid State Ionics* **2001**, *144*, 51−57.

(34) Xu, X.; Wen, Z.; Yang, X.; Zhang, J.; Gu, Z. High Lithium Ion Conductivity Glass-Ceramics in Li2O−AL2O3−TIO2−P2O5 from Nanoscaled Glassy Powders by Mechanical Milling. *Solid State Ionics* **2006**, *177*, 2611−2615.

(35) Kotobuki, M.; Munakata, H.; Kanamura, K.; Sato, Y.; Yoshida, T. Compatibility of Li7La3Zr2O12 Solid Electrolyte to All-Solid-State Battery Using Li Metal Anode. *J. Electrochem. Soc.* **2010**, *157*, A1076−A1079.

(36) Wolfenstine, J.; et al. Chemical Stability of Cubic Li7La 3Zr 2O 12 with Molten Lithium at Elevated Temperature. *J. Mater. Sci.* **2013**, *48*, 5846−5851.

(37) Wenzel, S.; Randau, S.; Leichtweiß, T.; Weber, D. A.; Sann, J.; Zeier, W. G.; Janek, J. Direct Observation of the Interfacial Instability of the Fast Ionic Conductor Li10GeP2S12 at the Lithium Metal Anode. *Chem. Mater.* **2016**, *28*, 2400−2407.

(38) Hakari, T.; Nagao, M.; Hayashi, A.; Tatsumisago, M. All-Solid-State Lithium Batteries with Li3ps4 Glass as Active Material. *J. Power Sources* **2015**, *293*, 721−725.

(39) Machida, N.; Yamamoto, H.; Asano, S.; Shigematsu, T. Preparation of Amorphous 75L2S·xP2S3·(25−x)P2S5 (Mol%) Solid Electrolytes by a High-Energy Ball-Milling Process and Their Application for an All-Solid-State Lithium Battery. *Solid State Ionics* **2005**, *176*, 473−479.

(40) Swamy, T.; Chen, X.; Chiang, Y.-M. Electrochemical Redox Behavior of Li Ion Conducting Sulfide Solid Electrolytes. *Chem. Mater.* **2019**, *31*, 707−713.

https://dx.doi.org/10.1021/acs.chemrev.0c00101
Chem. Rev. XXXX, XXX, XXX−XXX

(41) Tan, D. H. S.; Wu, E. A.; Nguyen, H.; Chen, Z.; Marple, M. A. T.; Doux, J.-M.; Wang, X.; Yang, H.; Banerjee, A.; Meng, Y. S. Elucidating Reversible Electrochemical Redox of Li6PS5Cl Solid Electrolyte. *ACS Energy Letters* **2019**, *4*, 2418−2427.
(42) Dewald, G. F.; Ohno, S.; Kraft, M. A.; Koerver, R.; Till, P.; Vargas-Barbosa, N. M.; Janek, J.; Zeier, W. G. Experimental Assessment of the Practical Oxidative Stability of Lithium Thiophosphate Solid Electrolytes. *Chem. Mater.* **2019**, *31*, 8328−8337.
(43) Wang, S.; Bai, Q.; Nolan, A. M.; Liu, Y.; Gong, S.; Sun, Q.; Mo, Y. Lithium Chlorides and Bromides as Promising Solid-State Chemistries for Fast Ion Conductors with Good Electrochemical Stability. *Angew. Chem., Int. Ed.* **2019**, *58*, 8039−8043.
(44) Kokal, I.; Somer, M.; Notten, P. H. L.; Hintzen, H. T. Sol−Gel Synthesis and Lithium Ion Conductivity of Li7La3Zr2O12 with Garnet-Related Type Structure. *Solid State Ionics* **2011**, *185*, 42−46.
(45) Koerver, R.; Walther, F.; Aygün, I.; Sann, J.; Dietrich, C.; Zeier, W. G.; Janek, J. Redox-Active Cathode Interphases in Solid-State Batteries. *J. Mater. Chem. A* **2017**, *5*, 22750−22760.
(46) Wu, B.; Wang, S.; Evans, W. J., Iv; Deng, D. Z.; Yang, J.; Xiao, J. Interfacial Behaviours between Lithium Ion Conductors and Electrode Materials in Various Battery Systems. *J. Mater. Chem. A* **2016**, *4*, 15266−15280.
(47) Trevey, J. E.; Stoldt, C. R.; Lee, S.-H. High Power Nanocomposite TiS2 Cathodes for All-Solid-State Lithium Batteries. *J. Electrochem. Soc.* **2011**, *158*, A1282−A1289.
(48) Asano, T.; Sakai, A.; Ouchi, S.; Sakaida, M.; Miyazaki, A.; Hasegawa, S. Solid Halide Electrolytes with High Lithium-Ion Conductivity for Application in 4 V Class Bulk-Type All-Solid-State Batteries. *Adv. Mater.* **2018**, *30*, 1803075−1803082.
(49) Banerjee, S.; Zhang, X.; Wang, L.-W. Motif-Based Design of an Oxysulfide Class of Lithium Superionic Conductors: Toward Improved Stability and Record-High Li-Ion Conductivity. *Chem. Mater.* **2019**, *31*, 7265−7276.
(50) Suzuki, K.; Sakuma, M.; Hori, S.; Nakazawa, T.; Nagao, M.; Yonemura, M.; Hirayama, M.; Kanno, R. Synthesis, Structure, and Electrochemical Properties of Crystalline Li−P−S−O Solid Electrolytes: Novel Lithium-Conducting Oxysulfides of Li10GeP2S12 Family. *Solid State Ionics* **2016**, *288*, 229−234.
(51) Banerjee, A.; Tang, H.; Wang, X.; Cheng, J.-H.; Nguyen, H.; Zhang, M.; Tan, D. H. S.; Wynn, T. A.; Wu, E. A.; Doux, J.-M.; et al. Revealing Nanoscale Solid−Solid Interfacial Phenomena for Long-Life and High-Energy All-Solid-State Batteries. *ACS Appl. Mater. Interfaces* **2019**, *11*, 43138−43145.
(52) Zhu, Y.; He, X.; Mo, Y. Origin of Outstanding Stability in the Lithium Solid Electrolyte Materials: Insights from Thermodynamic Analyses Based on First-Principles Calculations. *ACS Appl. Mater. Interfaces* **2015**, *7*, 23685−23693.
(53) Perdew, J. P. Density Functional Theory and the Band Gap Problem. *Int. J. Quantum Chem.* **1985**, *28*, 497−523.
(54) Julien, C. M.; Mauger, A.; Hussain, O. M. Sputtered LiCoO(2) Cathode Materials for All-Solid-State Thin-Film Lithium Microbatteries. *Materials* **2019**, *12*, 2687.
(55) Li, J.; Ma, C.; Chi, M.; Liang, C.; Dudney, N. J. Solid Electrolyte: The Key for High-Voltage Lithium Batteries. *Adv. Energy Mater.* **2015**, *5*, 1401408−1401414.
(56) Yu, X.; Bates, J. B.; Jellison, G. E.; Hart, F. X. A Stable Thin-Film Lithium Electrolyte: Lithium Phosphorus Oxynitride. *J. Electrochem. Soc.* **1997**, *144*, 524−532.
(57) Chen, Y.-T.; Jena, A.; Pang, W. K.; Peterson, V. K.; Sheu, H.-S.; Chang, H.; Liu, R.-S. Voltammetric Enhancement of Li-Ion Conduction in Al-Doped Li7−xLa3Zr2O12 Solid Electrolyte. *J. Phys. Chem. C* **2017**, *121*, 15565−15573.
(58) Rangasamy, E.; Wolfenstine, J.; Sakamoto, J. The Role of Al and Li Concentration on the Formation of Cubic Garnet Solid Electrolyte of Nominal Composition Li7La3Zr2O12. *Solid State Ionics* **2012**, *206*, 28−32.
(59) Shin, B. R.; Nam, Y. J.; Oh, D. Y.; Kim, D. H.; Kim, J. W.; Jung, Y. S. Comparative Study of TiS2/Li-in All-Solid-State Lithium Batteries Using Glass-Ceramic Li3PS4 and Li10GeP2S12 Solid Electrolytes. *Electrochim. Acta* **2014**, *146*, 395−402.
(60) Minami, K.; Mizuno, F.; Hayashi, A.; Tatsumisago, M. Lithium Ion Conductivity of the Li2S−P2S5 Glass-Based Electrolytes Prepared by the Melt Quenching Method. *Solid State Ionics* **2007**, *178*, 837−841.
(61) Li, J.; Dudney, N. J.; Nanda, J.; Liang, C. Artificial Solid Electrolyte Interphase to Address the Electrochemical Degradation of Silicon Electrodes. *ACS Appl. Mater. Interfaces* **2014**, *6*, 10083−10088.
(62) Le Van-Jodin, L.; Ducroquet, F.; Sabary, F.; Chevalier, I. Dielectric Properties, Conductivity and Li+ Ion Motion in Lipon Thin Films. *Solid State Ionics* **2013**, *253*, 151−156.
(63) Su, Y.; Falgenhauer, J.; Polity, A.; Leichtweiß, T.; Kronenberger, A.; Obel, J.; Zhou, S.; Schlettwein, D.; Janek, J.; Meyer, B. K. Lipon Thin Films with High Nitrogen Content for Application in Lithium Batteries and Electrochromic Devices Prepared by Rf Magnetron Sputtering. *Solid State Ionics* **2015**, *282*, 63−69.
(64) Strauss, F.; Bartsch, T.; de Biasi, L.; Kim, A. Y.; Janek, J.; Hartmann, P.; Brezesinski, T. Impact of Cathode Material Particle Size on the Capacity of Bulk-Type All-Solid-State Batteries. *ACS Energy Letters* **2018**, *3*, 992−996.
(65) Oh, G.; Hirayama, M.; Kwon, O.; Suzuki, K.; Kanno, R. Bulk-Type All Solid-State Batteries with 5 V Class LiNi0.5Mn1.5O4 Cathode and Li10GeP2S12 Solid Electrolyte. *Chem. Mater.* **2016**, *28*, 2634−2640.
(66) Zhang, W.; Leichtweiß, T.; Culver, S. P.; Koerver, R.; Das, D.; Weber, D. A.; Zeier, W. G.; Janek, J. The Detrimental Effects of Carbon Additives in Li10GeP2S12-Based Solid-State Batteries. *ACS Appl. Mater. Interfaces* **2017**, *9*, 35888−35896.
(67) Culver, S. P.; Koerver, R.; Krauskopf, T.; Zeier, W. G. Designing Ionic Conductors: The Interplay between Structural Phenomena and Interfaces in Thiophosphate-Based Solid-State Batteries. *Chem. Mater.* **2018**, *30*, 4179−4192.
(68) Ates, T.; Keller, M.; Kulisch, J.; Adermann, T.; Passerini, S. Development of an All-Solid-State Lithium Battery by Slurry-Coating Procedures Using a Sulfidic Electrolyte. *Energy Storage Materials* **2019**, *17*, 204−210.
(69) Hakari, T.; Deguchi, M.; Mitsuhara, K.; Ohta, T.; Saito, K.; Orikasa, Y.; Uchimoto, Y.; Kowada, Y.; Hayashi, A.; Tatsumisago, M. Structural and Electronic-State Changes of a Sulfide Solid Electrolyte During the Li Deinsertion−Insertion Processes. *Chem. Mater.* **2017**, *29*, 4768−4774.
(70) Hakari, T.; Sato, Y.; Yoshimi, S.; Hayashi, A.; Tatsumisago, M. Favorable Carbon Conductive Additives in Li3PS4 Composite Positive Electrode Prepared by Ball-Milling for All-Solid-State Lithium Batteries. *J. Electrochem. Soc.* **2017**, *164*, A2804−A2811.
(71) Hayashi, A.; Ohtsubo, R.; Nagao, M.; Tatsumisago, M. Characterization of Li2S−P2S5−Cu Composite Electrode for All-Solid-State Lithium Secondary Batteries. *J. Mater. Sci.* **2010**, *45*, 377−381.
(72) Suzuki, K.; Mashimo, N.; Ikeda, Y.; Yokoi, T.; Hirayama, M.; Kanno, R. High Cycle Capability of All-Solid-State Lithium−Sulfur Batteries Using Composite Electrodes by Liquid-Phase and Mechanical Mixing. *ACS Applied Energy Materials* **2018**, *1*, 2373−2377.
(73) Wang, S.; Zhang, Y.; Zhang, X.; Liu, T.; Lin, Y.-H.; Shen, Y.; Li, L.; Nan, C.-W. High-Conductivity Argyrodite Li6PS5Cl Solid Electrolytes Prepared Via Optimized Sintering Processes for All-Solid-State Lithium−Sulfur Batteries. *ACS Appl. Mater. Interfaces* **2018**, *10*, 42279−42285.
(74) Takada, K. Progress and Prospective of Solid-State Lithium Batteries. *Acta Mater.* **2013**, *61*, 759−770.
(75) Koerver, R.; Aygün, I.; Leichtweiß, T.; Dietrich, C.; Zhang, W.; Binder, J. O.; Hartmann, P.; Zeier, W. G.; Janek, J. Capacity Fade in Solid-State Batteries: Interphase Formation and Chemomechanical Processes in Nickel-Rich Layered Oxide Cathodes and Lithium Thiophosphate Solid Electrolytes. *Chem. Mater.* **2017**, *29*, 5574−5582.
(76) Ma, J.; Chen, B.; Wang, L.; Cui, G. Progress and Prospect on Failure Mechanisms of Solid-State Lithium Batteries. *J. Power Sources* **2018**, *392*, 94−115.

https://dx.doi.org/10.1021/acs.chemrev.0c00101
Chem. Rev. XXXX, XXX, XXX−XXX

(77) Pervez, S. A.; Cambaz, M. A.; Thangadurai, V.; Fichtner, M. Interface in Solid-State Lithium Battery: Challenges, Progress, and Outlook. *ACS Appl. Mater. Interfaces* **2019**, *11*, 22029−22050.
(78) Jain, A.; Hautier, G.; Moore, C. J.; Ping Ong, S.; Fischer, C. C.; Mueller, T.; Persson, K. A.; Ceder, G. A High-Throughput Infrastructure for Density Functional Theory Calculations. *Comput. Mater. Sci.* **2011**, *50*, 2295−2310.
(79) Yoshinari, T.; Koerver, R.; Hofmann, P.; Uchimoto, Y.; Zeier, W. G.; Janek, J. Interfacial Stability of Phosphate-Nasicon Solid Electrolytes in Ni-Rich NCM Cathode-Based Solid-State Batteries. *ACS Appl. Mater. Interfaces* **2019**, *11*, 23244−23253.
(80) Tang, H.; Deng, Z.; Lin, Z.; Wang, Z.; Chu, I.-H.; Chen, C.; Zhu, Z.; Zheng, C.; Ong, S. P. Probing Solid−Solid Interfacial Reactions in All-Solid-State Sodium-Ion Batteries with First-Principles Calculations. *Chem. Mater.* **2018**, *30*, 163−173.
(81) Lacivita, V.; Wang, Y.; Bo, S.-H.; Ceder, G. Ab Initio Investigation of the Stability of Electrolyte/Electrode Interfaces in All-Solid-State Na Batteries. *J. Mater. Chem. A* **2019**, *7*, 8144−8155.
(82) Jung, S. H.; Oh, K.; Nam, Y. J.; Oh, D. Y.; Brüner, P.; Kang, K.; Jung, Y. S. Li3BO3−Li2CO3: Rationally Designed Buffering Phase for Sulfide All-Solid-State Li-Ion Batteries. *Chem. Mater.* **2018**, *30*, 8190−8200.
(83) Ohta, N.; Takada, K.; Zhang, L.; Ma, R.; Osada, M.; Sasaki, T. Enhancement of the High-Rate Capability of Solid-State Lithium Batteries by Nanoscale Interfacial Modification. *Adv. Mater.* **2006**, *18*, 2226−2229.
(84) Cao, D.; Zhang, Y.; Nolan, A. M.; Sun, X.; Liu, C.; Sheng, J.; Mo, Y.; Wang, Y.; Zhu, H. Stable Thiophosphate-Based All-Solid-State Lithium Batteries through Conformally Interfacial Nanocoating. *Nano Lett.* **2020**, *20*, 1483−1490.
(85) Jung, S.-K.; Gwon, H.; Lee, S.-S.; Kim, H.; Lee, J. C.; Chung, J. G.; Park, S. Y.; Aihara, Y.; Im, D. Understanding the Effects of Chemical Reactions at the Cathode−Electrolyte Interface in Sulfide Based All-Solid-State Batteries. *J. Mater. Chem. A* **2019**, *7*, 22967−22976.
(86) Woo, J. H.; Trevey, J. E.; Cavanagh, A. S.; Choi, Y. S.; Kim, S. C.; George, S. M.; Oh, K. H.; Lee, S.-H. Nanoscale Interface Modification of LiCoO2 by Al2O3 Atomic Layer Deposition for Solid-State Li Batteries. *J. Electrochem. Soc.* **2012**, *159*, A1120−A1124.
(87) Auvergniot, J.; Cassel, A.; Ledeuil, J.-B.; Viallet, V.; Seznec, V.; Dedryvère, R. Interface Stability of Argyrodite Li6PS5Cl toward LiCoO2, LiNi1/3Co1/3Mn1/3O2, and LiMn2O4 in Bulk All-Solid-State Batteries. *Chem. Mater.* **2017**, *29*, 3883−3890.
(88) Ohta, S.; Kobayashi, T.; Seki, J.; Asaoka, T. Electrochemical Performance of an All-Solid-State Lithium Ion Battery with Garnet-Type Oxide Electrolyte. *J. Power Sources* **2012**, *202*, 332−335.
(89) Kim, K. H.; Iriyama, Y.; Yamamoto, K.; Kumazaki, S.; Asaka, T.; Tanabe, K.; Fisher, C. A. J.; Hirayama, T.; Murugan, R.; Ogumi, Z. Characterization of the Interface between Licoo2 and Li7La3Zr2O12 in an All-Solid-State Rechargeable Lithium Battery. *J. Power Sources* **2011**, *196*, 764−767.
(90) Park, K.; Yu, B.-C.; Jung, J.-W.; Li, Y.; Zhou, W.; Gao, H.; Son, S.; Goodenough, J. B. Electrochemical Nature of the Cathode Interface for a Solid-State Lithium-Ion Battery: Interface between LiCoO2 and Garnet-Li7La3Zr2O12. *Chem. Mater.* **2016**, *28*, 8051−8059.
(91) Vardar, G.; Bowman, W. J.; Lu, Q.; Wang, J.; Chater, R. J.; Aguadero, A.; Seibert, R.; Terry, J.; Hunt, A.; Waluyo, I.; et al. Structure, Chemistry, and Charge Transfer Resistance of the Interface between Li7La3Zr2O12 Electrolyte and LiCoO2 Cathode. *Chem. Mater.* **2018**, *30*, 6259−6276.
(92) Haruyama, J.; Sodeyama, K.; Han, L.; Takada, K.; Tateyama, Y. Space−Charge Layer Effect at Interface between Oxide Cathode and Sulfide Electrolyte in All-Solid-State Lithium-Ion Battery. *Chem. Mater.* **2014**, *26*, 4248−4255.
(93) Swift, M. W.; Qi, Y. First-Principles Prediction of Potentials and Space-Charge Layers in All-Solid-State Batteries. *Phys. Rev. Lett.* **2019**, *122*, 167701.
(94) Tateyama, Y.; Gao, B.; Jalem, R.; Haruyama, J. Theoretical Picture of Positive Electrode−Solid Electrolyte Interface in All-Solid-State Battery from Electrochemistry and Semiconductor Physics Viewpoints. *Current Opinion in Electrochemistry* **2019**, *17*, 149−157.
(95) Ohta, N.; Takada, K.; Sakaguchi, I.; Zhang, L.; Ma, R.; Fukuda, K.; Osada, M.; Sasaki, T. LiNbO3-Coated LiCoO2 as Cathode Material for All Solid-State Lithium Secondary Batteries. *Electrochem. Commun.* **2007**, *9*, 1486−1490.
(96) Takada, K.; Ohta, N.; Tateyama, Y. Recent Progress in Interfacial Nanoarchitectonics in Solid-State Batteries. *J. Inorg. Organomet. Polym. Mater.* **2015**, *25*, 205−213.
(97) Masuda, H.; Ishida, N.; Ogata, Y.; Ito, D.; Fujita, D. Internal Potential Mapping of Charged Solid-State-Lithium Ion Batteries Using in Situ Kelvin Probe Force Microscopy. *Nanoscale* **2017**, *9*, 893−898.
(98) Yamamoto, K.; Iriyama, Y.; Asaka, T.; Hirayama, T.; Fujita, H.; Fisher, C. A. J.; Nonaka, K.; Sugita, Y.; Ogumi, Z. Dynamic Visualization of the Electric Potential in an All-Solid-State Rechargeable Lithium Battery. *Angew. Chem., Int. Ed.* **2010**, *49*, 4414−4417.
(99) Xiao, Y.; Miara, L. J.; Wang, Y.; Ceder, G. Computational Screening of Cathode Coatings for Solid-State Batteries. *Joule* **2019**, *3*, 1252−1275.
(100) Wang, Z.; Shao, G. Theoretical Design of Solid Electrolytes with Superb Ionic Conductivity: Alloying Effect on Li+ Transportation in Cubic Li6PA5x Chalcogenides. *J. Mater. Chem. A* **2017**, *5*, 21846−21857.
(101) Choi, Y.-S.; Lee, J.-C. Electronic and Mechanistic Origins of the Superionic Conductivity of Sulfide-Based Solid Electrolytes. *J. Power Sources* **2019**, *415*, 189−196.
(102) Xu, H.; Yu, Y.; Wang, Z.; Shao, G. First Principle Material Genome Approach for All Solid-State Batteries. *Energy & Environmental Materials* **2019**, *2*, 234−250.
(103) Rong, Z.; Kitchaev, D.; Canepa, P.; Huang, W.; Ceder, G. An Efficient Algorithm for Finding the Minimum Energy Path for Cation Migration in Ionic Materials. *J. Chem. Phys.* **2016**, *145*, 074112−074120.
(104) Xie, J.; Sendek, A. D.; Cubuk, E. D.; Zhang, X.; Lu, Z.; Gong, Y.; Wu, T.; Shi, F.; Liu, W.; Reed, E. J.; et al. Atomic Layer Deposition of Stable LiAlF4 Lithium Ion Conductive Interfacial Layer for Stable Cathode Cycling. *ACS Nano* **2017**, *11*, 7019−7027.
(105) de Bernabe, A.; Prieto, C.; de Andres, A. Effect of Stoichiometry on the Dynamic Mechanical Properties of Linbo3. *J. Appl. Phys.* **1996**, *79*, 143−148.
(106) Sosunov, A. V.; Volyntsev, A. B.; Tsiberkin, K. B.; Yuriev, V. A.; Ponomarev, R. S. Features of Structure and Mechanical Properties Linbo3. *Ferroelectrics* **2017**, *506*, 24−31.
(107) Du, F.; Zhao, N.; Li, Y.; Chen, C.; Liu, Z.; Guo, X. All Solid State Lithium Batteries Based on Lamellar Garnet-Type Ceramic Electrolytes. *J. Power Sources* **2015**, *300*, 24−28.
(108) Kato, T.; Hamanaka, T.; Yamamoto, K.; Hirayama, T.; Sagane, F.; Motoyama, M.; Iriyama, Y. In-Situ Li7La3Zr2O12/LiCoO2 Interface Modification for Advanced All-Solid-State Battery. *J. Power Sources* **2014**, *260*, 292−298.
(109) Ohta, S.; Seki, J.; Yagi, Y.; Kihira, Y.; Tani, T.; Asaoka, T. Co-Sinterable Lithium Garnet-Type Oxide Electrolyte with Cathode for All-Solid-State Lithium Ion Battery. *J. Power Sources* **2014**, *265*, 40−44.
(110) Okumura, T.; Nakatsutsumi, T.; Ina, T.; Orikasa, Y.; Arai, H.; Fukutsuka, T.; Iriyama, Y.; Uruga, T.; Tanida, H.; Uchimoto, Y.; et al. Depth-Resolved X-Ray Absorption Spectroscopic Study on Nanoscale Observation of the Electrode−Solid Electrolyte Interface for All Solid State Lithium Ion Batteries. *J. Mater. Chem.* **2011**, *21*, 10051−10060.
(111) Hu, S.-K.; Cheng, G.-H.; Cheng, M.-Y.; Hwang, B.-J.; Santhanam, R. Cycle Life Improvement of ZrO2-Coated Spherical LiNi1/3Co1/3Mn1/3O2 Cathode Material for Lithium Ion Batteries. *J. Power Sources* **2009**, *188*, 564−569.
(112) Tatsumisago, M.; Mizuno, F.; Hayashi, A. All-Solid-State Lithium Secondary Batteries Using Sulfide-Based Glass−Ceramic Electrolytes. *J. Power Sources* **2006**, *159*, 193−199.
(113) Sakuda, A.; Kitaura, H.; Hayashi, A.; Tadanaga, K.; Tatsumisago, M. All-Solid-State Lithium Secondary Batteries with Oxide-Coated LiCoO2 Electrode and Li2S−P2S5 Electrolyte. *J. Power Sources* **2009**, *189*, 527−530.

https://dx.doi.org/10.1021/acs.chemrev.0c00101
Chem. Rev. XXXX, XXX, XXX−XXX

(114) Hayashi, A.; Muramatsu, H.; Ohtomo, T.; Hama, S.; Tatsumisago, M. Improved Chemical Stability and Cyclability in Li2S−P2S5−P2O5−ZnO Composite Electrolytes for All-Solid-State Rechargeable Lithium Batteries. *J. Alloys Compd.* **2014**, *591*, 247−250.
(115) Machida, N.; Kashiwagi, J.; Naito, M.; Shigematsu, T. Electrochemical Properties of All-Solid-State Batteries with ZrO2-Coated LiNi1/3Mn1/3Co1/3O2 as Cathode Materials. *Solid State Ionics* **2012**, *225*, 354−358.
(116) Seino, Y.; Ota, T.; Takada, K. High Rate Capabilities of All-Solid-State Lithium Secondary Batteries Using Li4Ti5O12-Coated LiNi0.8Co0.15Al0.05O2 and a Sulfide-Based Solid Electrolyte. *J. Power Sources* **2011**, *196*, 6488−6492.
(117) Sakuda, A.; Hayashi, A.; Tatsumisago, M. Electrochemical Performance of All-Solid-State Lithium Secondary Batteries Improved by the Coating of Li2O−TiO2 Films on LiCoO2 Electrode. *J. Power Sources* **2010**, *195*, 599−603.
(118) Noh, S.; Kim, J.; Eom, M.; Shin, D. Surface Modification of LiCoO2 with Li3xLa2/3−xTiO3 for All-Solid-State Lithium Ion Batteries Using Li2S−P2S5 Glass−Ceramic. *Ceram. Int.* **2013**, *39*, 8453−8458.
(119) Ito, S.; Fujiki, S.; Yamada, T.; Aihara, Y.; Park, Y.; Kim, T. Y.; Baek, S.-W.; Lee, J.-M.; Doo, S.; Machida, N. A Rocking Chair Type All-Solid-State Lithium Ion Battery Adopting Li2O−ZrO2 Coated LiNi0.8Co0.15Al0.05O2 and a Sulfide Based Electrolyte. *J. Power Sources* **2014**, *248*, 943−950.
(120) Sakuda, A.; Kitaura, H.; Hayashi, A.; Tadanaga, K.; Tatsumisago, M. Improvement of High-Rate Performance of All-Solid-State Lithium Secondary Batteries Using LiCoO2 Coated with Li2O−SiO2 Glasses. *Electrochem. Solid-State Lett.* **2008**, *11*, A1.
(121) Okada, K.; Machida, N.; Naito, M.; Shigematsu, T.; Ito, S.; Fujiki, S.; Nakano, M.; Aihara, Y. Preparation and Electrochemical Properties of LiAlO2-Coated Li(Ni1/3Mn1/3Co1/3)O2 for All-Solid-State Batteries. *Solid State Ionics* **2014**, *255*, 120−127.
(122) Visbal, H.; Aihara, Y.; Ito, S.; Watanabe, T.; Park, Y.; Doo, S. The Effect of Diamond-Like Carbon Coating on LiNi0.8Co0.15Al0.05O2 Particles for All Solid-State Lithium-Ion Batteries Based on Li2S−P2S5 Glass-Ceramics. *J. Power Sources* **2016**, *314*, 85−92.
(123) Ito, Y.; Sakurai, Y.; Yubuchi, S.; Sakuda, A.; Hayashi, A.; Tatsumisago, M. Application of LiCoO2 Particles Coated with Lithium Ortho-Oxosalt Thin Films to Sulfide-Type All-Solid-State Lithium Batteries. *J. Electrochem. Soc.* **2015**, *162*, A1610−A1616.
(124) Yubuchi, S.; Ito, Y.; Matsuyama, T.; Hayashi, A.; Tatsumisago, M. 5V Class LiNi0.5Mn1.5O4 Positive Electrode Coated with Li3PO4 Thin Film for All-Solid-State Batteries Using Sulfide Solid Electrolyte. *Solid State Ionics* **2016**, *285*, 79−82.
(125) Li, X.; Liang, J.; Chen, N.; Luo, J.; Adair, K. R.; Wang, C.; Banis, M. N.; Sham, T.-K.; Zhang, L.; Zhao, S.; et al. Water-Mediated Synthesis of a Superionic Halide Solid Electrolyte. *Angew. Chem., Int. Ed.* **2019**, *58*, 16427−16432.
(126) Li, X.; Liang, J.; Luo, J.; Norouzi Banis, M.; Wang, C.; Li, W.; Deng, S.; Yu, C.; Zhao, F.; Hu, Y.; et al. Air-Stable Li3InCl6 Electrolyte with High Voltage Compatibility for All-Solid-State Batteries. *Energy Environ. Sci.* **2019**, *12*, 2665−2671.
(127) Zhang, W.; Richter, F. H.; Culver, S. P.; Leichtweiss, T.; Lozano, J. G.; Dietrich, C.; Bruce, P. G.; Zeier, W. G.; Janek, J. Degradation Mechanisms at the Li10GeP2S12/LiCoO2 Cathode Interface in an All-Solid-State Lithium-Ion Battery. *ACS Appl. Mater. Interfaces* **2018**, *10*, 22226−22236.
(128) Wang, C.; Li, X.; Zhao, Y.; Banis, M. N.; Liang, J.; Li, X.; Sun, Y.; Adair, K. R.; Sun, Q.; Liu, Y.; et al. Manipulating Interfacial Nanostructure to Achieve High-Performance All-Solid-State Lithium-Ion Batteries. *Small Methods* **2019**, *3*, 1900261−1900269.
(129) Reimers, J. N.; Dahn, J. R. Electrochemical and in Situ X-Ray Diffraction Studies of Lithium Intercalation in LixCoO2. *J. Electrochem. Soc.* **1992**, *139*, 2091−2097.
(130) Cho, J.; Kim, Y. J.; Park, B. LiCoO2 Cathode Material That Does Not Show a Phase Transition from Hexagonal to Monoclinic Phase. *J. Electrochem. Soc.* **2001**, *148*, A1110−A1115.
(131) Tsai, Y. W.; Hwang, B. J.; Ceder, G.; Sheu, H. S.; Liu, D. G.; Lee, J. F. In-Situ X-Ray Absorption Spectroscopic Study on Variation of Electronic Transitions and Local Structure of LiNi1/3Co1/3Mn1/3O2 Cathode Material During Electrochemical Cycling. *Chem. Mater.* **2005**, *17*, 3191−3199.
(132) Yoon, W.-S.; Chung, K. Y.; McBreen, J.; Yang, X.-Q. A Comparative Study on Structural Changes of LiCo1/3Ni1/3Mn1/3O2 and LiNi0.8Co0.15Al0.05O2 During First Charge Using in Situ Xrd. *Electrochem. Commun.* **2006**, *8*, 1257−1262.
(133) Gu, M.; Li, Y.; Li, X.; Hu, S.; Zhang, X.; Xu, W.; Thevuthasan, S.; Baer, D. R.; Zhang, J.-G.; Liu, J.; et al. In Situ Tem Study of Lithiation Behavior of Silicon Nanoparticles Attached to and Embedded in a Carbon Matrix. *ACS Nano* **2012**, *6*, 8439−8447.
(134) Wang, C.-M.; Li, X.; Wang, Z.; Xu, W.; Liu, J.; Gao, F.; Kovarik, L.; Zhang, J.-G.; Howe, J.; Burton, D. J.; et al. In Situ Tem Investigation of Congruent Phase Transition and Structural Evolution of Nanostructured Silicon/Carbon Anode for Lithium Ion Batteries. *Nano Lett.* **2012**, *12*, 1624−1632.
(135) Sokolov, I. A.; Il'in, A. A.; Tarlakov, Y. P.; Valova, N. A.; Pronkin, A. A. Structure and Physicochemical Properties of Glasses in the Li2S−LIPO3 System. *Glass Phys. Chem.* **2003**, *29*, 282−290.
(136) Sakuda, A.; Hayashi, A.; Tatsumisago, M. Sulfide Solid Electrolyte with Favorable Mechanical Property for All-Solid-State Lithium Battery. *Sci. Rep.* **2013**, *3*, 2261.
(137) Nose, M.; Kato, A.; Sakuda, A.; Hayashi, A.; Tatsumisago, M. Evaluation of Mechanical Properties of Na2S−P2S5 Sulfide Glass Electrolytes. *J. Mater. Chem. A* **2015**, *3*, 22061−22065.
(138) Deng, Z.; Wang, Z.; Chu, I.-H.; Luo, J.; Ong, S. P. Elastic Properties of Alkali Superionic Conductor Electrolytes from First Principles Calculations. *J. Electrochem. Soc.* **2016**, *163*, A67−A74.
(139) McGrogan, F. P.; Swamy, T.; Bishop, S. R.; Eggleton, E.; Porz, L.; Chen, X.; Chiang, Y.-M.; Van Vliet, K. J. Compliant yet Brittle Mechanical Behavior of Li2S−P2S5 Lithium-Ion-Conducting Solid Electrolyte. *Adv. Energy Mater.* **2017**, *7*, 1602011−1602016.
(140) Kato, A.; Yamamoto, M.; Sakuda, A.; Hayashi, A.; Tatsumisago, M. Mechanical Properties of Li2S−P2S5 Glasses with Lithium Halides and Application in All-Solid-State Batteries. *ACS Applied Energy Materials* **2018**, *1*, 1002−1007.
(141) Makishima, A.; Mackenzie, J. D. Direct Calculation of Young's Moidulus of Glass. *J. Non-Cryst. Solids* **1973**, *12*, 35−45.
(142) Soga, N.; Yamanaka, H.; Hisamoto, C.; Kunugi, M. Elastic Properties and Structure of Alkaline-Earth Silicate Glasses. *J. Non-Cryst. Solids* **1976**, *22*, 67−76.
(143) Tian, H.-K.; Qi, Y. Simulation of the Effect of Contact Area Loss in All-Solid-State Li-Ion Batteries. *J. Electrochem. Soc.* **2017**, *164*, E3512−E3521.
(144) Koerver, R.; Zhang, W.; de Biasi, L.; Schweidler, S.; Kondrakov, A. O.; Kolling, S.; Brezesinski, T.; Hartmann, P.; Zeier, W. G.; Janek, J. Chemo-Mechanical Expansion of Lithium Electrode Materials − on the Route to Mechanically Optimized All-Solid-State Batteries. *Energy Environ. Sci.* **2018**, *11*, 2142−2158.
(145) Zhang, W.; Schröder, D.; Arlt, T.; Manke, I.; Koerver, R.; Pinedo, R.; Weber, D. A.; Sann, J.; Zeier, W. G.; Janek, J. (Electro)Chemical Expansion During Cycling: Monitoring the Pressure Changes in Operating Solid-State Lithium Batteries. *J. Mater. Chem. A* **2017**, *5*, 9929−9936.
(146) Doux, J. M.; Nguyen, H.; Tan, D. H. S.; Banerjee, A.; Wang, X.; Wu, E. A.; Jo, C.; Yang, H.; Meng, Y. S. Stack Pressure Considerations for Room-Temperature All-Solid-State Lithium Metal Batteries. *Adv. Energy Mater.* **2020**, *10*, 1903253−1903259.
(147) Strauss, F.; de Biasi, L.; Kim, A. Y.; Hertle, J.; Schweidler, S.; Janek, J.; Hartmann, P.; Brezesinski, T. Rational Design of Quasi-Zero-Strain NCM Cathode Materials for Minimizing Volume Change Effects in All-Solid-State Batteries. *ACS Materials Letters* **2020**, *2*, 84−88.
(148) Wu, X.; Billaud, J.; Jerjen, I.; Marone, F.; Ishihara, Y.; Adachi, M.; Adachi, Y.; Villevieille, C.; Kato, Y. Operando Visualization of Morphological Dynamics in All-Solid-State Batteries. *Adv. Energy Mater.* **2019**, *9*, 1901547−1901557.

https://dx.doi.org/10.1021/acs.chemrev.0c00101
Chem. Rev. XXXX, XXX, XXX−XXX

(149) McDowell, M. T.; Lee, S. W.; Harris, J. T.; Korgel, B. A.; Wang, C.; Nix, W. D.; Cui, Y. In Situ Tem of Two-Phase Lithiation of Amorphous Silicon Nanospheres. *Nano Lett.* **2013**, *13*, 758−764.
(150) Bucci, G.; Talamini, B.; Renuka Balakrishna, A.; Chiang, Y.-M.; Carter, W. C. Mechanical Instability of Electrode-Electrolyte Interfaces in Solid-State Batteries. *Physical Review Materials* **2018**, *2*, 105407−105418.
(151) Bucci, G.; Swamy, T.; Chiang, Y.-M.; Carter, W. C. Modeling of Internal Mechanical Failure of All-Solid-State Batteries During Electrochemical Cycling, and Implications for Battery Design. *J. Mater. Chem. A* **2017**, *5*, 19422−19430.
(152) Hao, F.; Mukherjee, P. P. Mesoscale Analysis of the Electrolyte-Electrode Interface in All-Solid-State Li-Ion Batteries. *J. Electrochem. Soc.* **2018**, *165*, A1857−A1864.
(153) Bielefeld, A.; Weber, D. A.; Janek, J. Microstructural Modeling of Composite Cathodes for All-Solid-State Batteries. *J. Phys. Chem. C* **2019**, *123*, 1626−1634.
(154) Lewis, J. A.; Tippens, J.; Cortes, F. J. Q.; McDowell, M. T. Chemo-Mechanical Challenges in Solid-State Batteries. *Trends in Chemistry* **2019**, *1*, 845−857.
(155) Wild, M.; O'Neill, L.; Zhang, T.; Purkayastha, R.; Minton, G.; Marinescu, M.; Offer, G. J. Lithium Sulfur Batteries, a Mechanistic Review. *Energy Environ. Sci.* **2015**, *8*, 3477−3494.
(156) Zhang, S. S. Liquid Electrolyte Lithium/Sulfur Battery: Fundamental Chemistry, Problems, and Solutions. *J. Power Sources* **2013**, *231*, 153−162.
(157) Umeshbabu, E.; Zheng, B.; Yang, Y. Recent Progress in All-Solid-State Lithium−Sulfur Batteries Using High Li-Ion Conductive Solid Electrolytes. *Electrochemical Energy Reviews* **2019**, *2*, 199−230.
(158) Lin, Z.; Liu, Z.; Dudney, N. J.; Liang, C. Lithium Superionic Sulfide Cathode for All-Solid Lithium-Sulfur Batteries. *ACS Nano* **2013**, *7*, 2829−2833.
(159) Hassoun, J.; Scrosati, B. Moving to a Solid-State Configuration: A Valid Approach to Making Lithium-Sulfur Batteries Viable for Practical Applications. *Adv. Mater.* **2010**, *22*, 5198−5201.
(160) Hayashi, A.; Ohtomo, T.; Mizuno, F.; Tadanaga, K.; Tatsumisago, M. All-Solid-State Li/S Batteries with Highly Conductive Glass−Ceramic Electrolytes. *Electrochem. Commun.* **2003**, *5*, 701−705.
(161) Nagao, M.; Hayashi, A.; Tatsumisago, M. Sulfur−Carbon Composite Electrode for All-Solid-State Li/S Battery with Li2S−P2S5 Solid Electrolyte. *Electrochim. Acta* **2011**, *56*, 6055−6059.
(162) Yue, J.; Yan, M.; Yin, Y.-X.; Guo, Y.-G. Progress of the Interface Design in All-Solid-State Li−S Batteries. *Adv. Funct. Mater.* **2018**, *28*, 1707533−1707549.
(163) Ji, X.; Lee, K. T.; Nazar, L. F. A Highly Ordered Nanostructured Carbon−Sulphur Cathode for Lithium−Sulphur Batteries. *Nat. Mater.* **2009**, *8*, 500−506.
(164) Luo, C.; Ji, X.; Chen, J.; Gaskell, K. J.; He, X.; Liang, Y.; Jiang, J.; Wang, C. Solid-State Electrolyte Anchored with a Carboxylated Azo Compound for All-Solid-State Lithium Batteries. *Angew. Chem., Int. Ed.* **2018**, *57*, 8567−8571.
(165) Aso, K.; Sakuda, A.; Hayashi, A.; Tatsumisago, M. All-Solid-State Lithium Secondary Batteries Using Nis-Carbon Fiber Composite Electrodes Coated with LI2S−P2S5 Solid Electrolytes by Pulsed Laser Deposition. *ACS Appl. Mater. Interfaces* **2013**, *5*, 686−690.
(166) Kinoshita, S.; Okuda, K.; Machida, N.; Naito, M.; Sigematsu, T. All-Solid-State Lithium Battery with Sulfur/Carbon Composites as Positive Electrode Materials. *Solid State Ionics* **2014**, *256*, 97−102.
(167) Hakari, T.; Hayashi, A.; Tatsumisago, M. Li2s-Based Solid Solutions as Positive Electrodes with Full Utilization and Superlong Cycle Life in All-Solid-State Li/S Batteries. *Advanced Sustainable Systems* **2017**, *1*, 1700017−1700023.
(168) Suzuki, K.; Kato, D.; Hara, K.; Yano, T.-a.; Hirayama, M.; Hara, M.; Kanno, R. Composite Sulfur Electrode Prepared by High-Temperature Mechanical Milling for Use in an All-Solid-State Lithium−Sulfur Battery with a Li3.25Ge0.25P0.75S4 Electrolyte. *Electrochim. Acta* **2017**, *258*, 110−115.
(169) Nagao, M.; Hayashi, A.; Tatsumisago, M. Electrochemical Performance of All-Solid-State Li/S Batteries with Sulfur-Based Composite Electrodes Prepared by Mechanical Milling at High Temperature. *Energy Technology* **2013**, *1*, 186−192.
(170) Kobayashi, T.; Imade, Y.; Shishihara, D.; Homma, K.; Nagao, M.; Watanabe, R.; Yokoi, T.; Yamada, A.; Kanno, R.; Tatsumi, T. All Solid-State Battery with Sulfur Electrode and Thio-Lisicon Electrolyte. *J. Power Sources* **2008**, *182*, 621−625.
(171) Yu, C.; Ganapathy, S.; Eck, E. R. H. v.; Wang, H.; Basak, S.; Li, Z.; Wagemaker, M. Accessing the Bottleneck in All-Solid State Batteries, Lithium-Ion Transport over the Solid-Electrolyte-Electrode Interface. *Nat. Commun.* **2017**, *8*, 1086−1095.
(172) Yu, C.; Ganapathy, S.; de Klerk, N. J. J.; Roslon, I.; van Eck, E. R. H.; Kentgens, A. P. M.; Wagemaker, M. Unravelling Li-Ion Transport from Picoseconds to Seconds: Bulk Versus Interfaces in an Argyrodite Li6PS5Cl−Li2S All-Solid-State Li-Ion Battery. *J. Am. Chem. Soc.* **2016**, *138*, 11192−11201.
(173) Hakari, T.; Hayashi, A.; Tatsumisago, M. Highly Utilized Lithium Sulfide Active Material by Enhancing Conductivity in All-Solid-State Batteries. *Chem. Lett.* **2015**, *44*, 1664−1666.
(174) Hakari, T.; Hayashi, A.; Tatsumisago, M. Li2S-Based Solid Solutions as Positive Electrodes with Full Utilization and Superlong Cycle Life in All-Solid-State Li/S Batteries. *Advanced Sustainable Systems* **2017**, *1*, 1700017.
(175) Lin, Z.; Liu, Z.; Fu, W.; Dudney, N. J.; Liang, C. Lithium Polysulfidophosphates: A Family of Lithium-Conducting Sulfur-Rich Compounds for Lithium−Sulfur Batteries. *Angew. Chem., Int. Ed.* **2013**, *52*, 7460−7463.
(176) Han, F.; Yue, J.; Fan, X.; Gao, T.; Luo, C.; Ma, Z.; Suo, L.; Wang, C. High-Performance All-Solid-State Lithium−Sulfur Battery Enabled by a Mixed-Conductive Li2S Nanocomposite. *Nano Lett.* **2016**, *16*, 4521−4527.
(177) Lin, Z.; Liu, Z.; Fu, W.; Dudney, N. J.; Liang, C. Lithium Polysulfidophosphates: A Family of Lithium-Conducting Sulfur-Rich Compounds for Lithium−Sulfur Batteries. *Angew. Chem.* **2013**, *125*, 7608−7611.
(178) Ulissi, U.; Ito, S.; Hosseini, S. M.; Varzi, A.; Aihara, Y.; Passerini, S. High Capacity All-Solid-State Lithium Batteries Enabled by Pyrite-Sulfur Composites. *Adv. Energy Mater.* **2018**, *8*, 1801462.
(179) Liu, L.; Xu, J.; Wang, S.; Wu, F.; Li, H.; Chen, L. Practical Evaluation of Energy Densities for Sulfide Solid-State Batteries. *eTransportation* **2019**, *1*, 100010−100026.
(180) Sakuda, A.; Hayashi, A.; Hama, S.; Tatsumisago, M. Preparation of Highly Lithium-Ion Conductive 80Li2S·20P2S5 Thin-Film Electrolytes Using Pulsed Laser Deposition. *J. Am. Ceram. Soc.* **2010**, *93*, 765−768.
(181) Sakuda, A.; Hayashi, A.; Ohtomo, T.; Hama, S.; Tatsumisago, M. All-Solid-State Lithium Secondary Batteries Using LiCoO2 Particles with Pulsed Laser Deposition Coatings of Li2S−P2S5 Solid Electrolytes. *J. Power Sources* **2011**, *196*, 6735−6741.
(182) Ito, Y.; Otoyama, M.; Hayashi, A.; Ohtomo, T.; Tatsumisago, M. Electrochemical and Structural Evaluation for Bulk-Type All-Solid-State Batteries Using Li4GeS4-Li3PS4 Electrolyte Coating on LiCoO2 Particles. *J. Power Sources* **2017**, *360*, 328−335.
(183) Park, K. H.; Oh, D. Y.; Choi, Y. E.; Nam, Y. J.; Han, L.; Kim, J.-Y.; Xin, H.; Lin, F.; Oh, S. M.; Jung, Y. S. Solution-Processable Glass Lii-Li4sns4 Superionic Conductors for All-Solid-State Li-Ion Batteries. *Adv. Mater.* **2016**, *28*, 1874−1883.
(184) Choi, Y. E.; Park, K. H.; Kim, D. H.; Oh, D. Y.; Kwak, H. R.; Lee, Y.-G.; Jung, Y. S. Coatable Li4sns4 Solid Electrolytes Prepared from Aqueous Solutions for All-Solid-State Lithium-Ion Batteries. *ChemSusChem* **2017**, *10*, 2605−2611.
(185) Heo, J. W.; Banerjee, A.; Park, K. H.; Jung, Y. S.; Hong, S.-T. New Na-Ion Solid Electrolytes Na4−xSn1−xSbxS4 ($0.02 \leq X \leq 0.33$) for All-Solid-State Na-Ion Batteries. *Adv. Energy Mater.* **2018**, *8*, 1702716−1702722.
(186) Park, K. H.; Kim, D. H.; Kwak, H.; Jung, S. H.; Lee, H.-J.; Banerjee, A.; Lee, J. H.; Jung, Y. S. Solution-Derived Glass-Ceramic Nai·Na3SbS4 Superionic Conductors for All-Solid-State Na-Ion Batteries. *J. Mater. Chem. A* **2018**, *6*, 17192−17200.

https://dx.doi.org/10.1021/acs.chemrev.0c00101
Chem. Rev. XXXX, XXX, XXX−XXX

(187) Uematsu, M.; Yubuchi, S.; Noi, K.; Sakuda, A.; Hayashi, A.; Tatsumisago, M. Preparation of Na3PS4 Electrolyte by Liquid-Phase Process Using Ether. *Solid State Ionics* **2018**, *320*, 33−37.
(188) Banerjee, A.; Park, K. H.; Heo, J. W.; Nam, Y. J.; Moon, C. K.; Oh, S. M.; Hong, S.-T.; Jung, Y. S. Na3SbS4: A Solution Processable Sodium Superionic Conductor for All-Solid-State Sodium-Ion Batteries. *Angew. Chem., Int. Ed.* **2016**, *55*, 9634−9638.
(189) Park, K. H.; Bai, Q.; Kim, D. H.; Oh, D. Y.; Zhu, Y.; Mo, Y.; Jung, Y. S. Design Strategies, Practical Considerations, and New Solution Processes of Sulfide Solid Electrolytes for All-Solid-State Batteries. *Adv. Energy Mater.* **2018**, *8*, 1800035−1800059.
(190) Hayashi, A.; Muramatsu, H.; Ohtomo, T.; Hama, S.; Tatsumisago, M. Improvement of Chemical Stability of Li3PS4 Glass Electrolytes by Adding MxOy (M = Fe, Zn, and Bi) Nanoparticles. *J. Mater. Chem. A* **2013**, *1*, 6320−6326.
(191) Muramatsu, H.; Hayashi, A.; Ohtomo, T.; Hama, S.; Tatsumisago, M. Structural Change of Li2S−P2S5 Sulfide Solid Electrolytes in the Atmosphere. *Solid State Ionics* **2011**, *182*, 116−119.
(192) Rosero-Navarro, N. C.; Miura, A.; Tadanaga, K. Composite Cathode Prepared by Argyrodite Precursor Solution Assisted by Dispersant Agents for Bulk-Type All-Solid-State Batteries. *J. Power Sources* **2018**, *396*, 33−40.
(193) Yubuchi, S.; Teragawa, S.; Aso, K.; Tadanaga, K.; Hayashi, A.; Tatsumisago, M. Preparation of High Lithium-Ion Conducting Li6ps5cl Solid Electrolyte from Ethanol Solution for All-Solid-State Lithium Batteries. *J. Power Sources* **2015**, *293*, 941−945.
(194) Yubuchi, S.; Uematsu, M.; Deguchi, M.; Hayashi, A.; Tatsumisago, M. Lithium-Ion-Conducting Argyrodite-Type Li6PS5x (X = Cl, Br, I) Solid Electrolytes Prepared by a Liquid-Phase Technique Using Ethanol as a Solvent. *ACS Applied Energy Materials* **2018**, *1*, 3622−3629.
(195) Yubuchi, S.; Uematsu, M.; Hotehama, C.; Sakuda, A.; Hayashi, A.; Tatsumisago, M. An Argyrodite Sulfide-Based Superionic Conductor Synthesized by a Liquid-Phase Technique with Tetrahydrofuran and Ethanol. *J. Mater. Chem. A* **2019**, *7*, 558−566.
(196) Chida, S.; Miura, A.; Rosero-Navarro, N. C.; Higuchi, M.; Phuc, N. H. H.; Muto, H.; Matsuda, A.; Tadanaga, K. Liquid-Phase Synthesis of Li6PS5Br Using Ultrasonication and Application to Cathode Composite Electrodes in All-Solid-State Batteries. *Ceram. Int.* **2018**, *44*, 742−746.
(197) Yao, X.; Liu, D.; Wang, C.; Long, P.; Peng, G.; Hu, Y.-S.; Li, H.; Chen, L.; Xu, X. High-Energy All-Solid-State Lithium Batteries with Ultralong Cycle Life. *Nano Lett.* **2016**, *16*, 7148−7154.
(198) Zhang, Q.; Mwizerwa, J. P.; Wan, H.; Cai, L.; Xu, X.; Yao, X. Fe3S4@Li7P3S11 Nanocomposites as Cathode Materials for All-Solid-State Lithium Batteries with Improved Energy Density and Low Cost. *J. Mater. Chem. A* **2017**, *5*, 23919−23925.
(199) Xu, R. C.; Wang, X. L.; Zhang, S. Z.; Xia, Y.; Xia, X. H.; Wu, J. B.; Tu, J. P. Rational Coating of Li7P3S11 Solid Electrolyte on MoS2 Electrode for All-Solid-State Lithium Ion Batteries. *J. Power Sources* **2018**, *374*, 107−112.
(200) Wan, H.; Mwizerwa, J. P.; Qi, X.; Liu, X.; Xu, X.; Li, H.; Hu, Y.-S.; Yao, X. Core−Shell Fe1−xS@Na2.9PS3.95Se0.05 Nanorods for Room Temperature All-Solid-State Sodium Batteries with High Energy Density. *ACS Nano* **2018**, *12*, 2809−2817.
(201) Wan, H.; Mwizerwa, J. P.; Qi, X.; Xu, X.; Li, H.; Zhang, Q.; Cai, L.; Hu, Y.-S.; Yao, X. Nanoscaled Na3PS4 Solid Electrolyte for All-Solid-State FeS2/Na Batteries with Ultrahigh Initial Coulombic Efficiency of 95% and Excellent Cyclic Performances. *ACS Appl. Mater. Interfaces* **2018**, *10*, 12300−12304.
(202) Long, P.; Zhang, Z.; Peng, G.; Zhang, Q.; Liu, D.; Xu, X.; Yao, X. Facile Synthesis of Co9s8 Nanosheets for Lithium Ion Batteries with Enhanced Rate Capability and Cycling Stability. *New J. Chem.* **2017**, *41*, 9184−9191.
(203) Homma, K.; Yonemura, M.; Kobayashi, T.; Nagao, M.; Hirayama, M.; Kanno, R. Crystal Structure and Phase Transitions of the Lithium Ionic Conductor Li3PS4. *Solid State Ionics* **2011**, *182*, 53−58.
(204) Kim, D. H.; Oh, D. Y.; Park, K. H.; Choi, Y. E.; Nam, Y. J.; Lee, H. A.; Lee, S.-M.; Jung, Y. S. Infiltration of Solution-Processable Solid Electrolytes into Conventional Li-Ion-Battery Electrodes for All-Solid-State Li-Ion Batteries. *Nano Lett.* **2017**, *17*, 3013−3020.
(205) Kim, D. H.; Lee, H. A.; Song, Y. B.; Park, J. W.; Lee, S.-M.; Jung, Y. S. Sheet-Type Li6PS5Cl-Infiltrated Si Anodes Fabricated by Solution Process for All-Solid-State Lithium-Ion Batteries. *J. Power Sources* **2019**, *426*, 143−150.
(206) Kawaguchi, T.; Nakamura, H.; Watano, S. Dry Coating of Electrode Particle with Model Particle of Sulfide Solid Electrolytes for All-Solid-State Secondary Battery. *Powder Technol.* **2018**, *323*, 581−587.
(207) Han, X.; Gong, Y.; Fu, K.; He, X.; Hitz, G. T.; Dai, J.; Pearse, A.; Liu, B.; Wang, H.; Rubloff, G.; et al. Negating Interfacial Impedance in Garnet-Based Solid-State Li Metal Batteries. *Nat. Mater.* **2017**, *16*, 572−579.
(208) Oh, D. Y.; Nam, Y. J.; Park, K. H.; Jung, S. H.; Cho, S.-J.; Kim, Y. K.; Lee, Y.-G.; Lee, S.-Y.; Jung, Y. S. Excellent Compatibility of Solvate Ionic Liquids with Sulfide Solid Electrolytes: Toward Favorable Ionic Contacts in Bulk-Type All-Solid-State Lithium-Ion Batteries. *Adv. Energy Mater.* **2015**, *5*, 1500865−1500872.
(209) Oh, D. Y.; Nam, Y. J.; Park, K. H.; Jung, S. H.; Kim, K. T.; Ha, A. R.; Jung, Y. S. Slurry-Fabricable Li+-Conductive Polymeric Binders for Practical All-Solid-State Lithium-Ion Batteries Enabled by Solvate Ionic Liquids. *Adv. Energy Mater.* **2019**, *9*, 1802927−1802937.
(210) Fan, X.; Ji, X.; Han, F.; Yue, J.; Chen, J.; Chen, L.; Deng, T.; Jiang, J.; Wang, C. Fluorinated Solid Electrolyte Interphase Enables Highly Reversible Solid-State Li Metal Battery. *Science Advances* **2018**, *4*, eaau9245−eaau9255.
(211) Chen, B.; Ju, J.; Ma, J.; Zhang, J.; Xiao, R.; Cui, G.; Chen, L. An Insight into Intrinsic Interfacial Properties between Li Metals and Li10GeP2S12 Solid Electrolytes. *Phys. Chem. Chem. Phys.* **2017**, *19*, 31436−31442.
(212) Hartmann, P.; Leichtweiss, T.; Busche, M. R.; Schneider, M.; Reich, M.; Sann, J.; Adelhelm, P.; Janek, J. Degradation of Nasicon-Type Materials in Contact with Lithium Metal: Formation of Mixed Conducting Interphases (MCI) on Solid Electrolytes. *J. Phys. Chem. C* **2013**, *117*, 21064−21074.
(213) Wenzel, S.; Sedlmaier, S. J.; Dietrich, C.; Zeier, W. G.; Janek, J. Interfacial Reactivity and Interphase Growth of Argyrodite Solid Electrolytes at Lithium Metal Electrodes. *Solid State Ionics* **2018**, *318*, 102−112.
(214) Hayashi, A.; Hama, S.; Mizuno, F.; Tadanaga, K.; Minami, T.; Tatsumisago, M. Characterization of Li2S−P2S5 Glass-Ceramics as a Solid Electrolyte for Lithium Secondary Batteries. *Solid State Ionics* **2004**, *175*, 683−686.
(215) Nagao, M.; Hayashi, A.; Tatsumisago, M.; Kanetsuku, T.; Tsuda, T.; Kuwabata, S. In Situ Sem Study of a Lithium Deposition and Dissolution Mechanism in a Bulk-Type Solid-State Cell with a Li2S−P2S5 Solid Electrolyte. *Phys. Chem. Chem. Phys.* **2013**, *15*, 18600−18606.
(216) Trevey, J. E.; Gilsdorf, J. R.; Stoldt, C. R.; Lee, S.-H.; Liu, P. Electrochemical Investigation of All-Solid-State Lithium Batteries with a High Capacity Sulfur-Based Electrode. *J. Electrochem. Soc.* **2012**, *159*, A1019−A1022.
(217) Bron, P.; Roling, B.; Dehnen, S. Impedance Characterization Reveals Mixed Conducting Interphases between Sulfidic Superionic Conductors and Lithium Metal Electrodes. *J. Power Sources* **2017**, *352*, 127−134.
(218) Zhang, Z.; Chen, S.; Yang, J.; Wang, J.; Yao, L.; Yao, X.; Cui, P.; Xu, X. Interface Re-Engineering of Li10GeP2S12 Electrolyte and Lithium Anode for All-Solid-State Lithium Batteries with Ultralong Cycle Life. *ACS Appl. Mater. Interfaces* **2018**, *10*, 2556−2565.
(219) Sahu, G.; Lin, Z.; Li, J.; Liu, Z.; Dudney, N.; Liang, C. Air-Stable, High-Conduction Solid Electrolytes of Arsenic-Substituted Li4sns4. *Energy Environ. Sci.* **2014**, *7*, 1053−1058.
(220) Liu, Y.; Sun, Q.; Zhao, Y.; Wang, B.; Kaghazchi, P.; Adair, K. R.; Li, R.; Zhang, C.; Liu, J.; Kuo, L.-Y.; et al. Stabilizing the Interface of Nasicon Solid Electrolyte against Li Metal with Atomic Layer Deposition. *ACS Appl. Mater. Interfaces* **2018**, *10*, 31240−31248.

https://dx.doi.org/10.1021/acs.chemrev.0c00101
Chem. Rev. XXXX, XXX, XXX−XXX

(221) Hao, X.; Zhao, Q.; Su, S.; Zhang, S.; Ma, J.; Shen, L.; Yu, Q.; Zhao, L.; Liu, Y.; Kang, F.; et al. Constructing Multifunctional Interphase between Li1.4Al0.4Ti1.6(PO4)3 and Li Metal by Magnetron Sputtering for Highly Stable Solid-State Lithium Metal Batteries. *Adv. Energy Mater.* **2019**, *9*, 1901604−1901612.
(222) Tian, Y.; Sun, Y.; Hannah, D. C.; Xiao, Y.; Liu, H.; Chapman, K. W.; Bo, S.-H.; Ceder, G. Reactivity-Guided Interface Design in Na Metal Solid-State Batteries. *Joule* **2019**, *3*, 1037−1050.
(223) Yu, S.; Schmohl, S.; Liu, Z.; Hoffmeyer, M.; Schön, N.; Hausen, F.; Tempel, H.; Kungl, H.; Wiemhöfer, H. D.; Eichel, R. A. Insights into a Layered Hybrid Solid Electrolyte and Its Application in Long Lifespan High-Voltage All-Solid-State Lithium Batteries. *J. Mater. Chem. A* **2019**, *7*, 3882−3894.
(224) Bosubabu, D.; Sivaraj, J.; Sampathkumar, R.; Ramesha, K. Lagpl Li Interface Modification through a Wetted Polypropylene Interlayer for Solid State Li-Ion and Li−S Batteries. *ACS Applied Energy Materials* **2019**, *2*, 4118−4125.
(225) Hu, P.; Zhang, Y.; Chi, X.; Kumar Rao, K.; Hao, F.; Dong, H.; Guo, F.; Ren, Y.; Grabow, L. C.; Yao, Y. Stabilizing the Interface between Sodium Metal Anode and Sulfide-Based Solid-State Electrolyte with an Electron-Blocking Interlayer. *ACS Appl. Mater. Interfaces* **2019**, *11*, 9672−9678.
(226) Zhou, W.; Wang, S.; Li, Y.; Xin, S.; Manthiram, A.; Goodenough, J. B. Plating a Dendrite-Free Lithium Anode with a Polymer/Ceramic/Polymer Sandwich Electrolyte. *J. Am. Chem. Soc.* **2016**, *138*, 9385−9388.
(227) Liang, J.; Sun, Q.; Zhao, Y.; Sun, Y.; Wang, C.; Li, W.; Li, M.; Wang, D.; Li, X.; Liu, Y.; et al. Stabilization of All-Solid-State Li−S Batteries with a Polymer−Ceramic Sandwich Electrolyte by Atomic Layer Deposition. *J. Mater. Chem. A* **2018**, *6*, 23712−23719.
(228) Yamamoto, T.; Sugiura, Y.; Iwasaki, H.; Motoyama, M.; Iriyama, Y. Freestanding All-Solid-State Rechargeable Lithium Batteries with in-Situ Formed Positive Electrodes. *Solid State Ionics* **2019**, *337*, 19−23.
(229) Sun, Y.; Suzuki, K.; Hara, K.; Hori, S.; Yano, T.-a.; Hara, M.; Hirayama, M.; Kanno, R. Oxygen Substitution Effects in Li10GeP2S12 Solid Electrolyte. *J. Power Sources* **2016**, *324*, 798−803.
(230) Zhang, Z.; Zhang, L.; Yan, X.; Wang, H.; Liu, Y.; Yu, C.; Cao, X.; van Eijck, L.; Wen, B. All-in-One Improvement toward Li6PS5Br-Based Solid Electrolytes Triggered by Compositional Tune. *J. Power Sources* **2019**, *410*−*411*, 162−170.
(231) Xu, R.-c.; Xia, X.-h.; Wang, X.-l.; Xia, Y.; Tu, J.-p. Tailored Li2S−P2S5 Glass-Ceramic Electrolyte by MoS2 Doping, Possessing High Ionic Conductivity for All-Solid-State Lithium-Sulfur Batteries. *J. Mater. Chem. A* **2017**, *5*, 2829−2834.
(232) Liu, G.; Xie, D.; Wang, X.; Yao, X.; Chen, S.; Xiao, R.; Li, H.; Xu, X. High Air-Stability and Superior Lithium Ion Conduction of Li3 + 3xP1-xZnxS4-xOx by Aliovalent Substitution of Zno for All-Solid-State Lithium Batteries. *Energy Storage Materials* **2019**, *17*, 266−274.
(233) Li, W.; Wu, G.; Araújo, C. M.; Scheicher, R. H.; Blomqvist, A.; Ahuja, R.; Xiong, Z.; Feng, Y.; Chen, P. Li+ Ion Conductivity and Diffusion Mechanism in A-Li3N and B-Li3N. *Energy Environ. Sci.* **2010**, *3*, 1524−1530.
(234) Park, K.; Goodenough, J. B. Dendrite-Suppressed Lithium Plating from a Liquid Electrolyte Via Wetting of Li3N. *Adv. Energy Mater.* **2017**, *7*, 1700732−1700739.
(235) Kızılaslan, A.; Akbulut, H. Assembling All-Solid-State Lithium−Sulfur Batteries with Li3N-Protected Anodes. *ChemPlusChem* **2019**, *84*, 183−189.
(236) Xu, H.; Li, Y.; Zhou, A.; Wu, N.; Xin, S.; Li, Z.; Goodenough, J. B. Li3N-Modified Garnet Electrolyte for All-Solid-State Lithium Metal Batteries Operated at 40 °C. *Nano Lett.* **2018**, *18*, 7414−7418.
(237) Li, Y.; Sun, Y.; Pei, A.; Chen, K.; Vailionis, A.; Li, Y.; Zheng, G.; Sun, J.; Cui, Y. Robust Pinhole-Free Li3N Solid Electrolyte Grown from Molten Lithium. *ACS Cent. Sci.* **2018**, *4*, 97−104.
(238) Court-Castagnet, R.; Kaps, C.; Cros, C.; Hagenmuller, P. Ionic Conductivity-Enhancement of Licl by Homogeneous and Heterogeneous Dopings. *Solid State Ionics* **1993**, *61*, 327−334.
(239) Li, C.; Gu, L.; Maier, J. Enhancement of the Li Conductivity in Lif by Introducing Glass/Crystal Interfaces. *Adv. Funct. Mater.* **2012**, *22*, 1145−1149.
(240) Sudo, R.; Nakata, Y.; Ishiguro, K.; Matsui, M.; Hirano, A.; Takeda, Y.; Yamamoto, O.; Imanishi, N. Interface Behavior between Garnet-Type Lithium-Conducting Solid Electrolyte and Lithium Metal. *Solid State Ionics* **2014**, *262*, 151−154.
(241) Suzuki, Y.; Kami, K.; Watanabe, K.; Watanabe, A.; Saito, N.; Ohnishi, T.; Takada, K.; Sudo, R.; Imanishi, N. Transparent Cubic Garnet-Type Solid Electrolyte of Al2O3-Doped Li7La3Zr2O12. *Solid State Ionics* **2015**, *278*, 172−176.
(242) Ishiguro, K.; Nakata, Y.; Matsui, M.; Uechi, I.; Takeda, Y.; Yamamoto, O.; Imanishi, N. Stability of Nb-Doped Cubic Li7La3Zr2O12 with Lithium Metal. *J. Electrochem. Soc.* **2013**, *160*, A1690−A1693.
(243) Basappa, R. H.; Ito, T.; Yamada, H. Contact between Garnet-Type Solid Electrolyte and Lithium Metal Anode: Influence on Charge Transfer Resistance and Short Circuit Prevention. *J. Electrochem. Soc.* **2017**, *164*, A666−A671.
(244) Zhang, S.; Ding, M. S.; Xu, K.; Allen, J.; Jow, T. R. Understanding Solid Electrolyte Interface Film Formation on Graphite Electrodes. *Electrochem. Solid-State Lett.* **2001**, *4*, A206−A208.
(245) Liu, P.; Wang, J.; Hicks-Garner, J.; Sherman, E.; Soukiazian, S.; Verbrugge, M.; Tataria, H.; Musser, J.; Finamore, P. Aging Mechanisms of LiFePO4 Batteries Deduced by Electrochemical and Structural Analyses. *J. Electrochem. Soc.* **2010**, *157*, A499−A507.
(246) Aurbach, D. Review of Selected Electrode−Solution Interactions Which Determine the Performance of Li and Li Ion Batteries. *J. Power Sources* **2000**, *89*, 206−218.
(247) Broussely, M.; Biensan, P.; Bonhomme, F.; Blanchard, P.; Herreyre, S.; Nechev, K.; Staniewicz, R. J. Main Aging Mechanisms in Li Ion Batteries. *J. Power Sources* **2005**, *146*, 90−96.
(248) Wang, C.; Gong, Y.; Liu, B.; Fu, K.; Yao, Y.; Hitz, E.; Li, Y.; Dai, J.; Xu, S.; Luo, W.; et al. Conformal, Nanoscale Zno Surface Modification of Garnet-Based Solid-State Electrolyte for Lithium Metal Anodes. *Nano Lett.* **2017**, *17*, 565−571.
(249) Luo, W.; Gong, Y.; Zhu, Y.; Fu, K. K.; Dai, J.; Lacey, S. D.; Wang, C.; Liu, B.; Han, X.; Mo, Y.; et al. Transition from Superlithiophobicity to Superlithiophilicity of Garnet Solid-State Electrolyte. *J. Am. Chem. Soc.* **2016**, *138*, 12258−12262.
(250) Tsai, C.-L.; Roddatis, V.; Chandran, C. V.; Ma, Q.; Uhlenbruck, S.; Bram, M.; Heitjans, P.; Guillon, O. Li7La3Zr2O12 Interface Modification for Li Dendrite Prevention. *ACS Appl. Mater. Interfaces* **2016**, *8*, 10617−10626.
(251) Lu, Y.; Huang, X.; Ruan, Y.; Wang, Q.; Kun, R.; Yang, J.; Wen, Z. An in Situ Element Permeation Constructed High Endurance Li−LLZO Interface at High Current Densities. *J. Mater. Chem. A* **2018**, *6*, 18853−18858.
(252) Luo, W.; Gong, Y.; Zhu, Y.; Li, Y.; Yao, Y.; Zhang, Y.; Fu, K.; Pastel, G.; Lin, C.-F.; Mo, Y.; et al. Reducing Interfacial Resistance between Garnet-Structured Solid-State Electrolyte and Li-Metal Anode by a Germanium Layer. *Adv. Mater.* **2017**, *29*, 1606042−1606049.
(253) Fu, K.; Gong, Y.; Fu, Z.; Xie, H.; Yao, Y.; Liu, B.; Carter, M.; Wachsman, E.; Hu, L. Transient Behavior of the Metal Interface in Lithium Metal−Garnet Batteries. *Angew. Chem., Int. Ed.* **2017**, *56*, 14942−14947.
(254) Zhou, W.; Zhu, Y.; Grundish, N.; Sen, X.; Wang, S.; You, Y.; Wu, N.; Gao, J.; Cui, Z.; Li, Y.; et al. Polymer Lithium-Garnet Interphase for an All-Solid-State Rechargeable Battery. *Nano Energy* **2018**, *53*, 926−931.
(255) Liu, B.; Gong, Y.; Fu, K.; Han, X.; Yao, Y.; Pastel, G.; Yang, C.; Xie, H.; Wachsman, E. D.; Hu, L. Garnet Solid Electrolyte Protected Li-Metal Batteries. *ACS Appl. Mater. Interfaces* **2017**, *9*, 18809−18815.
(256) Wang, X.; Liu, Z.; Zhang, C.; Kong, Q.; Yao, J.; Han, P.; Jiang, W.; Xu, H.; Cui, G. Exploring Polymeric Lithium Tartaric Acid Borate for Thermally Resistant Polymer Electrolyte of Lithium Batteries. *Electrochim. Acta* **2013**, *92*, 132−138.
(257) Zhang, T.; Imanishi, N.; Hirano, A.; Takeda, Y.; Yamamoto, O. Stability of Li/Polymer Electrolyte-Ionic Liquid Composite/Lithium

https://dx.doi.org/10.1021/acs.chemrev.0c00101
Chem. Rev. XXXX, XXX, XXX−XXX

Conducting Glass Ceramics in an Aqueous Electrolyte. *Electrochem. Solid-State Lett.* **2011**, *14*, A45−A48.
(258) Zhang, J.; Zang, X.; Wen, H.; Dong, T.; Chai, J.; Li, Y.; Chen, B.; Zhao, J.; Dong, S.; Ma, J.; et al. High-Voltage and Free-Standing Poly(Propylene Carbonate)/Li6.75La3Zr1.75Ta0.25O12 Composite Solid Electrolyte for Wide Temperature Range and Flexible Solid Lithium Ion Battery. *J. Mater. Chem. A* **2017**, *5*, 4940−4948.
(259) Zhang, J.; Zhao, N.; Zhang, M.; Li, Y.; Chu, P. K.; Guo, X.; Di, Z.; Wang, X.; Li, H. Flexible and Ion-Conducting Membrane Electrolytes for Solid-State Lithium Batteries: Dispersion of Garnet Nanoparticles in Insulating Polyethylene Oxide. *Nano Energy* **2016**, *28*, 447−454.
(260) Croce, F.; Appetecchi, G. B.; Persi, L.; Scrosati, B. Nanocomposite Polymer Electrolytes for Lithium Batteries. *Nature* **1998**, *394*, 456−458.
(261) Sharafi, A.; Yu, S.; Naguib, M.; Lee, M.; Ma, C.; Meyer, H. M.; Nanda, J.; Chi, M.; Siegel, D. J.; Sakamoto, J. Impact of Air Exposure and Surface Chemistry on Li−Li7La3Zr2O12 Interfacial Resistance. *J. Mater. Chem. A* **2017**, *5*, 13475−13487.
(262) Cheng, L.; Crumlin, E. J.; Chen, W.; Qiao, R.; Hou, H.; Franz Lux, S.; Zorba, V.; Russo, R.; Kostecki, R.; Liu, Z.; et al. The Origin of High Electrolyte−Electrode Interfacial Resistances in Lithium Cells Containing Garnet Type Solid Electrolytes. *Phys. Chem. Chem. Phys.* **2014**, *16*, 18294−18300.
(263) Shimonishi, Y.; Toda, A.; Zhang, T.; Hirano, A.; Imanishi, N.; Yamamoto, O.; Takeda, Y. Synthesis of Garnet-Type Li7−xLa3Zr2O12−1/2x and Its Stability in Aqueous Solutions. *Solid State Ionics* **2011**, *183*, 48−53.
(264) Galven, C.; Dittmer, J.; Suard, E.; Le Berre, F.; Crosnier-Lopez, M.-P. Instability of Lithium Garnets against Moisture. Structural Characterization and Dynamics of Li7-xHxLa3Sn2O12 and Li5-xHxLa3Nb2O12. *Chem. Mater.* **2012**, *24*, 3335−3345.
(265) Toda, S.; Ishiguro, K.; Shimonishi, Y.; Hirano, A.; Takeda, Y.; Yamamoto, O.; Imanishi, N. Low Temperature Cubic Garnet-Type Co2-Doped Li7La3Zr2O12. *Solid State Ionics* **2013**, *233*, 102−106.
(266) Xia, W.; Xu, B.; Duan, H.; Guo, Y.; Kang, H.; Li, H.; Liu, H. Ionic Conductivity and Air Stability of Al-Doped Li7La3Zr2O12 Sintered in Alumina and Pt Crucibles. *ACS Appl. Mater. Interfaces* **2016**, *8*, 5335−5342.
(267) Taylor, N. J.; Stangeland-Molo, S.; Haslam, C. G.; Sharafi, A.; Thompson, T.; Wang, M.; Garcia-Mendez, R.; Sakamoto, J. Demonstration of High Current Densities and Extended Cycling in the Garnet Li7La3Zr2O12 Solid Electrolyte. *J. Power Sources* **2018**, *396*, 314−318.
(268) Sharafi, A.; Kazyak, E.; Davis, A. L.; Yu, S.; Thompson, T.; Siegel, D. J.; Dasgupta, N. P.; Sakamoto, J. Surface Chemistry Mechanism of Ultra-Low Interfacial Resistance in the Solid-State Electrolyte Li7La3Zr2O12. *Chem. Mater.* **2017**, *29*, 7961−7968.
(269) Wang, C.; Zhao, Y.; Sun, Q.; Li, X.; Liu, Y.; Liang, J.; Li, X.; Lin, X.; Li, R.; Adair, K. R.; et al. Stabilizing Interface between Li10Sn2S12 and Li Metal by Molecular Layer Deposition. *Nano Energy* **2018**, *53*, 168−174.
(270) Xie, D.; Chen, S.; Zhang, Z.; Ren, J.; Yao, L.; Wu, L.; Yao, X.; Xu, X. High Ion Conductive Sb2O5-Doped B-Li3PS4 with Excellent Stability against Li for All-Solid-State Lithium Batteries. *J. Power Sources* **2018**, *389*, 140−147.
(271) Gao, Y.; Wang, D.; Li, Y. C.; Yu, Z.; Mallouk, T. E.; Wang, D. Salt-Based Organic−Inorganic Nanocomposites: Towards a Stable Lithium Metal/Li10GeP2S12 Solid Electrolyte Interface. *Angew. Chem., Int. Ed.* **2018**, *57*, 13608−13612.
(272) Xu, R.; Han, F.; Ji, X.; Fan, X.; Tu, J.; Wang, C. Interface Engineering of Sulfide Electrolytes for All-Solid-State Lithium Batteries. *Nano Energy* **2018**, *53*, 958−966.
(273) Zheng, B. Z.; Zhu, J. P.; Wang, H. C.; Feng, M.; Umeshbabu, E.; Li, Y. X.; Wu, Q. H.; Yang, Y. Stabilizing Li10SnP2S12/Li Interface Via an in Situ Formed Solid Electrolyte Interphase Layer. *ACS Appl. Mater. Interfaces* **2018**, *10*, 25473−25482.
(274) Sang, L.; Bassett, K. L.; Castro, F. C.; Young, M. J.; Chen, L.; Haasch, R. T.; Elam, J. W.; Dravid, V. P.; Nuzzo, R. G.; Gewirth, A. A. Understanding the Effect of Interlayers at the Thiophosphate Solid Electrolyte/Lithium Interface for All-Solid-State Li Batteries. *Chem. Mater.* **2018**, *30*, 8747−8756.
(275) Umeshbabu, E.; Zheng, B.; Zhu, J.; Wang, H.; Li, Y.; Yang, Y. Stable Cycling Lithium−Sulfur Solid Batteries with Enhanced Li/Li10GeP2S12 Solid Electrolyte Interface Stability. *ACS Appl. Mater. Interfaces* **2019**, *11*, 18436−18447.
(276) Liang, J.; Li, X.; Zhao, Y.; Goncharova, L. V.; Li, W.; Adair, K. R.; Banis, M. N.; Hu, Y.; Sham, T.-K.; Huang, H. An Air-Stable and Dendrite-Free Li Anode for Highly Stable All-Solid-State Sulfide-Based Li Batteries. *Adv. Energy Mater.* **2019**, *9*, 1902125−1902135.
(277) Wang, C.; Adair, K. R.; Liang, J.; Li, X.; Sun, Y.; Li, X.; Wang, J.; Sun, Q.; Zhao, F.; Lin, X.; et al. Solid-State Plastic Crystal Electrolytes: Effective Protection Interlayers for Sulfide-Based All-Solid-State Lithium Metal Batteries. *Adv. Funct. Mater.* **2019**, *29*, 1900392−1900400.
(278) Philip, M. A.; Sullivan, P. T.; Zhang, R.; Wooley, G. A.; Kohn, S. A.; Gewirth, A. A. Improving Cell Resistance and Cycle Life with Solvate-Coated Thiophosphate Solid Electrolytes in Lithium Batteries. *ACS Appl. Mater. Interfaces* **2019**, *11*, 2014−2021.
(279) Shen, Y.; Zhang, Y.; Han, S.; Wang, J.; Peng, Z.; Chen, L. Unlocking the Energy Capabilities of Lithium Metal Electrode with Solid-State Electrolytes. *Joule* **2018**, *2*, 1674−1689.
(280) LePage, W. S.; Chen, Y.; Kazyak, E.; Chen, K.-H.; Sanchez, A. J.; Poli, A.; Arruda, E. M.; Thouless, M. D.; Dasgupta, N. P. Lithium Mechanics: Roles of Strain Rate and Temperature and Implications for Lithium Metal Batteries. *J. Electrochem. Soc.* **2019**, *166*, A89−A97.
(281) Wang, M.; Sakamoto, J. Correlating the Interface Resistance and Surface Adhesion of the Li Metal-Solid Electrolyte Interface. *J. Power Sources* **2018**, *377*, 7−11.
(282) Wood, K. N.; Noked, M.; Dasgupta, N. P. Lithium Metal Anodes: Toward an Improved Understanding of Coupled Morphological, Electrochemical, and Mechanical Behavior. *ACS Energy Letters* **2017**, *2*, 664−672.
(283) Cheng, E. J.; Sharafi, A.; Sakamoto, J. Intergranular Li Metal Propagation through Polycrystalline Li6.25Al0.25La3Zr2O12 Ceramic Electrolyte. *Electrochim. Acta* **2017**, *223*, 85−91.
(284) Porz, L.; Swamy, T.; Sheldon, B. W.; Rettenwander, D.; Frömling, T.; Thaman, H. L.; Berendts, S.; Uecker, R.; Carter, W. C.; Chiang, Y.-M. Mechanism of Lithium Metal Penetration through Inorganic Solid Electrolytes. *Adv. Energy Mater.* **2017**, *7*, 1701003−1701015.
(285) Wu, B.; Wang, S.; Lochala, J.; Desrochers, D.; Liu, B.; Zhang, W.; Yang, J.; Xiao, J. The Role of the Solid Electrolyte Interphase Layer in Preventing Li Dendrite Growth in Solid-State Batteries. *Energy Environ. Sci.* **2018**, *11*, 1803−1810.
(286) Yu, S.; Schmidt, R. D.; Garcia-Mendez, R.; Herbert, E.; Dudney, N. J.; Wolfenstine, J. B.; Sakamoto, J.; Siegel, D. J. Elastic Properties of the Solid Electrolyte Li7La3Zr2O12 (LLZO). *Chem. Mater.* **2016**, *28*, 197−206.
(287) Sundström, L.-G.; Bark, F. H. On Morphological Instability During Electrodeposition with a Stagnant Binary Electrolyte. *Electrochim. Acta* **1995**, *40*, 599−614.
(288) Monroe, C.; Newman, J. The Impact of Elastic Deformation on Deposition Kinetics at Lithium/Polymer Interfaces. *J. Electrochem. Soc.* **2005**, *152*, A396−A404.
(289) Barai, P.; Higa, K.; Srinivasan, V. Effect of Initial State of Lithium on the Propensity for Dendrite Formation: A Theoretical Study. *J. Electrochem. Soc.* **2017**, *164*, A180−A189.
(290) Yu, S.; Siegel, D. J. Grain Boundary Softening: A Potential Mechanism for Lithium Metal Penetration through Stiff Solid Electrolytes. *ACS Appl. Mater. Interfaces* **2018**, *10*, 38151−38158.
(291) Masias, A.; Felten, N.; Garcia-Mendez, R.; Wolfenstine, J.; Sakamoto, J. Elastic, Plastic, and Creep Mechanical Properties of Lithium Metal. *J. Mater. Sci.* **2019**, *54*, 2585−2600.
(292) Kasemchainan, J.; Zekoll, S.; Spencer Jolly, D.; Ning, Z.; Hartley, G. O.; Marrow, J.; Bruce, P. G. Critical Stripping Current Leads to Dendrite Formation on Plating in Lithium Anode Solid Electrolyte Cells. *Nat. Mater.* **2019**, *18*, 1105−1111.

https://dx.doi.org/10.1021/acs.chemrev.0c00101
Chem. Rev. XXXX, XXX, XXX−XXX

(293) Wang, M.; Wolfenstine, J. B.; Sakamoto, J. Temperature Dependent Flux Balance of the Li/Li7La3Zr2O12 Interface. *Electrochim. Acta* **2019**, *296*, 842−847.
(294) Krauskopf, T.; Hartmann, H.; Zeier, W. G.; Janek, J. Toward a Fundamental Understanding of the Lithium Metal Anode in Solid-State Batteries—an Electrochemo-Mechanical Study on the Garnet-Type Solid Electrolyte Li6.25Al0.25La3Zr2O12. *ACS Appl. Mater. Interfaces* **2019**, *11*, 14463−14477.
(295) Koshikawa, H.; Matsuda, S.; Kamiya, K.; Miyayama, M.; Kubo, Y.; Uosaki, K.; Hashimoto, K.; Nakanishi, S. Dynamic Changes in Charge-Transfer Resistance at Li Metal/Li7La3Zr2O12 Interfaces During Electrochemical Li Dissolution/Deposition Cycles. *J. Power Sources* **2018**, *376*, 147−151.
(296) Janek, J. Oscillatory Kinetics at Solid/Solid Phase Boundaries in Ionic Crystals. *Solid State Ionics* **2000**, *131*, 129−142.
(297) Swamy, T.; Park, R.; Sheldon, B. W.; Rettenwander, D.; Porz, L.; Berendts, S.; Uecker, R.; Carter, W. C.; Chiang, Y.-M. Lithium Metal Penetration Induced by Electrodeposition through Solid Electrolytes: Example in Single-Crystal Li6La3ZrTaO12 Garnet. *J. Electrochem. Soc.* **2018**, *165*, A3648−A3655.
(298) Shen, F.; Dixit, M. B.; Xiao, X.; Hatzell, K. B. Effect of Pore Connectivity on Li Dendrite Propagation within LLZO Electrolytes Observed with Synchrotron X-Ray Tomography. *ACS Energy Letters* **2018**, *3*, 1056−1061.
(299) Sharafi, A.; Haslam, C. G.; Kerns, R. D.; Wolfenstine, J.; Sakamoto, J. Controlling and Correlating the Effect of Grain Size with the Mechanical and Electrochemical Properties of Li7La3Zr2O12 Solid-State Electrolyte. *J. Mater. Chem. A* **2017**, *5*, 21491−21504.
(300) Cheng, L.; Wu, C. H.; Jarry, A.; Chen, W.; Ye, Y.; Zhu, J.; Kostecki, R.; Persson, K.; Guo, J.; Salmeron, M.; et al. Interrelationships among Grain Size, Surface Composition, Air Stability, and Interfacial Resistance of Al-Substituted Li7La3Zr2O12 Solid Electrolytes. *ACS Appl. Mater. Interfaces* **2015**, *7*, 17649−17655.
(301) Tschopp, M. A.; Solanki, K. N.; Gao, F.; Sun, X.; Khaleel, M. A.; Horstemeyer, M. F. Probing Grain Boundary Sink Strength at the Nanoscale: Energetics and Length Scales of Vacancy and Interstitial Absorption by Grain Boundaries in Alpha-Fe. *Phys. Rev. B: Condens. Matter Mater. Phys.* **2012**, *85*, 064108−064129.
(302) David, I. N.; Thompson, T.; Wolfenstine, J.; Allen, J. L.; Sakamoto, J. Microstructure and Li-Ion Conductivity of Hot-Pressed Cubic Li7La3Zr2O12. *J. Am. Ceram. Soc.* **2015**, *98*, 1209−1214.
(303) Saylor, D. M.; El Dasher, B.; Pang, Y.; Miller, H. M.; Wynblatt, P.; Rollett, A. D.; Rohrer, G. S. Habits of Grains in Dense Polycrystalline Solids. *J. Am. Ceram. Soc.* **2004**, *87*, 724−726.
(304) Pesci, F. M.; Brugge, R. H.; Hekselman, A. K. O.; Cavallaro, A.; Chater, R. J.; Aguadero, A. Elucidating the Role of Dopants in the Critical Current Density for Dendrite Formation in Garnet Electrolytes. *J. Mater. Chem. A* **2018**, *6*, 19817−19827.
(305) Xu, K. Electrolytes and Interphases in Li-Ion Batteries and Beyond. *Chem. Rev.* **2014**, *114*, 11503−11618.
(306) Cheng, X.-B.; Zhang, R.; Zhao, C.-Z.; Zhang, Q. Toward Safe Lithium Metal Anode in Rechargeable Batteries: A Review. *Chem. Rev.* **2017**, *117*, 10403−10473.
(307) Fang, C.; Li, J.; Zhang, M.; Zhang, Y.; Yang, F.; Lee, J. Z.; Lee, M.-H.; Alvarado, J.; Schroeder, M. A.; Yang, Y.; et al. Quantifying Inactive Lithium in Lithium Metal Batteries. *Nature* **2019**, *572*, 511−515.
(308) Niu, C.; Lee, H.; Chen, S.; Li, Q.; Du, J.; Xu, W.; Zhang, J.-G.; Whittingham, M. S.; Xiao, J.; Liu, J. High-Energy Lithium Metal Pouch Cells with Limited Anode Swelling and Long Stable Cycles. *Nature Energy* **2019**, *4*, 551−559.
(309) Peled, E.; Golodnitsky, D.; Ardel, G. Advanced Model for Solid Electrolyte Interphase Electrodes in Liquid and Polymer Electrolytes. *J. Electrochem. Soc.* **1997**, *144*, L208−L210.
(310) Cao, X.; Ren, X.; Zou, L.; Engelhard, M. H.; Huang, W.; Wang, H.; Matthews, B. E.; Lee, H.; Niu, C.; Arey, B. W.; et al. Monolithic Solid−Electrolyte Interphases Formed in Fluorinated Orthoformate-Based Electrolytes Minimize Li Depletion and Pulverization. *Nature Energy* **2019**, *4*, 796−805.
(311) Li, N.-W.; Yin, Y.-X.; Yang, C.-P.; Guo, Y.-G. An Artificial Solid Electrolyte Interphase Layer for Stable Lithium Metal Anodes. *Adv. Mater.* **2016**, *28*, 1853−1858.
(312) Xu, R.; Cheng, X.-B.; Yan, C.; Zhang, X.-Q.; Xiao, Y.; Zhao, C.-Z.; Huang, J.-Q.; Zhang, Q. Artificial Interphases for Highly Stable Lithium Metal Anode. *Matter* **2019**, *1*, 317−344.
(313) Liu, Y.; Tzeng, Y.-K.; Lin, D.; Pei, A.; Lu, H.; Melosh, N. A.; Shen, Z.-X.; Chu, S.; Cui, Y. An Ultrastrong Double-Layer Nanodiamond Interface for Stable Lithium Metal Anodes. *Joule* **2018**, *2*, 1595−1609.
(314) Gu, Y.; Wang, W.-W.; Li, Y.-J.; Wu, Q.-H.; Tang, S.; Yan, J.-W.; Zheng, M.-S.; Wu, D.-Y.; Fan, C.-H.; Hu, W.-Q.; et al. Designable Ultra-Smooth Ultra-Thin Solid-Electrolyte Interphases of Three Alkali Metal Anodes. *Nat. Commun.* **2018**, *9*, 1339−1348.
(315) Lu, D.; Shao, Y.; Lozano, T.; Bennett, W. D.; Graff, G. L.; Polzin, B.; Zhang, J.; Engelhard, M. H.; Saenz, N. T.; Henderson, W. A.; et al. Failure Mechanism for Fast-Charged Lithium Metal Batteries with Liquid Electrolytes. *Adv. Energy Mater.* **2015**, *5*, 1400993−1401000.
(316) Fang, C.; Wang, X.; Meng, Y. S. Key Issues Hindering a Practical Lithium-Metal Anode. *Trends in Chemistry* **2019**, *1*, 152−158.
(317) Nagpure, S. C.; Tanim, T. R.; Dufek, E. J.; Viswanathan, V. V.; Crawford, A. J.; Wood, S. M.; Xiao, J.; Dickerson, C. C.; Liaw, B. Impacts of Lean Electrolyte on Cycle Life for Rechargeable Li Metal Batteries. *J. Power Sources* **2018**, *407*, 53−62.
(318) Pei, A.; Zheng, G.; Shi, F.; Li, Y.; Cui, Y. Nanoscale Nucleation and Growth of Electrodeposited Lithium Metal. *Nano Lett.* **2017**, *17*, 1132−1139.
(319) Wang, J.; Huang, W.; Pei, A.; Li, Y.; Shi, F.; Yu, X.; Cui, Y. Improving Cyclability of Li Metal Batteries at Elevated Temperatures and Its Origin Revealed by Cryo-Electron Microscopy. *Nature Energy* **2019**, *4*, 664−670.
(320) Weber, R.; Genovese, M.; Louli, A. J.; Hames, S.; Martin, C.; Hill, I. G.; Dahn, J. R. Long Cycle Life and Dendrite-Free Lithium Morphology in Anode-Free Lithium Pouch Cells Enabled by a Dual-Salt Liquid Electrolyte. *Nature Energy* **2019**, *4*, 683−689.
(321) Albertus, P.; Babinec, S.; Litzelman, S.; Newman, A. Status and Challenges in Enabling the Lithium Metal Electrode for High-Energy and Low-Cost Rechargeable Batteries. *Nature Energy* **2018**, *3*, 16−21.
(322) Zhu, Y.; He, X.; Mo, Y. Strategies Based on Nitride Materials Chemistry to Stabilize Li Metal Anode. *Advanced Science* **2017**, *4*, 1600517−1600528.
(323) Wang, Z.; Santhanagopalan, D.; Zhang, W.; Wang, F.; Xin, H. L.; He, K.; Li, J.; Dudney, N.; Meng, Y. S. In Situ Stem-Eels Observation of Nanoscale Interfacial Phenomena in All-Solid-State Batteries. *Nano Lett.* **2016**, *16*, 3760−3767.
(324) Brazier, A.; Dupont, L.; Dantras-Laffont, L.; Kuwata, N.; Kawamura, J.; Tarascon, J. M. First Cross-Section Observation of an All Solid-State Lithium-Ion "Nanobattery" by Transmission Electron Microscopy. *Chem. Mater.* **2008**, *20*, 2352−2359.
(325) Wang, X.; Zhang, M.; Alvarado, J.; Wang, S.; Sina, M.; Lu, B.; Bouwer, J.; Xu, W.; Xiao, J.; Zhang, J.-G.; et al. New Insights on the Structure of Electrochemically Deposited Lithium Metal and Its Solid Electrolyte Interphases Via Cryogenic Tem. *Nano Lett.* **2017**, *17*, 7606−7612.
(326) Lee, J. Z.; Wynn, T. A.; Schroeder, M. A.; Alvarado, J.; Wang, X.; Xu, K.; Meng, Y. S. Cryogenic Focused Ion Beam Characterization of Lithium Metal Anodes. *ACS Energy Letters* **2019**, *4*, 489−493.
(327) Banerjee, A.; Tang, H.; Wang, X.; Cheng, J.-h.; Nguyen, H.; Zhang, M.; Tan, D.; Wynn, T.; Wu, E.; Doux, J.-M.; et al. Revealing Nanoscale Solid-Solid Interfacial Phenomena for Long-Life and High-Energy All-Solid-State Batteries. *ACS Appl. Mater. Interfaces* **2019**, *11*, 43138−43145.
(328) Harry, K. J.; Hallinan, D. T.; Parkinson, D. Y.; MacDowell, A. A.; Balsara, N. P. Detection of Subsurface Structures Underneath Dendrites Formed on Cycled Lithium Metal Electrodes. *Nat. Mater.* **2014**, *13*, 69−73.
(329) Seitzman, N.; Guthrey, H.; Sulas, D. B.; Platt, H. A. S.; Al-Jassim, M.; Pylypenko, S. Toward All-Solid-State Lithium Batteries:

https://dx.doi.org/10.1021/acs.chemrev.0c00101
Chem. Rev. XXXX, XXX, XXX−XXX

Three-Dimensional Visualization of Lithium Migration in Beta-Li3PS4 Ceramic Electrolyte. *J. Electrochem. Soc.* **2018**, *165*, A3732−A3737.
(330) Liang, J.-Y.; Zeng, X.-X.; Zhang, X.-D.; Wang, P.-F.; Ma, J.-Y.; Yin, Y.-X.; Wu, X.-W.; Guo, Y.-G.; Wan, L.-J. Mitigating Interfacial Potential Drop of Cathode−Solid Electrolyte Via Ionic Conductor Layer to Enhance Interface Dynamics for Solid Batteries. *J. Am. Chem. Soc.* **2018**, *140*, 6767−6770.
(331) Gittleson, F. S.; El Gabaly, F. Non-Faradaic Li+ Migration and Chemical Coordination across Solid-State Battery Interfaces. *Nano Lett.* **2017**, *17*, 6974−6982.
(332) Fingerle, M.; Buchheit, R.; Sicolo, S.; Albe, K.; Hausbrand, R. Reaction and Space Charge Layer Formation at the LiCoO2−Lipon Interface: Insights on Defect Formation and Ion Energy Level Alignment by a Combined Surface Science−Simulation Approach. *Chem. Mater.* **2017**, *29*, 7675−7685.
(333) Wenzel, S.; Leichtweiss, T.; Krüger, D.; Sann, J.; Janek, J. Interphase Formation on Lithium Solid Electrolytes—an in Situ Approach to Study Interfacial Reactions by Photoelectron Spectroscopy. *Solid State Ionics* **2015**, *278*, 98−105.
(334) Wood, K. N.; Steirer, K. X.; Hafner, S. E.; Ban, C.; Santhanagopalan, S.; Lee, S.-H.; Teeter, G. Operando X-Ray Photoelectron Spectroscopy of Solid Electrolyte Interphase Formation and Evolution in Li2s-P2s5 Solid-State Electrolytes. *Nat. Commun.* **2018**, *9*, 2490−2500.
(335) Rettenwander, D.; Wagner, R.; Reyer, A.; Bonta, M.; Cheng, L.; Doeff, M. M.; Limbeck, A.; Wilkening, M.; Amthauer, G. Interface Instability of Fe-Stabilized Li7La3Zr2O12 Versus Li Metal. *J. Phys. Chem. C* **2018**, *122*, 3780−3785.
(336) Sang, L.; Haasch, R. T.; Gewirth, A. A.; Nuzzo, R. G. Evolution at the Solid Electrolyte/Gold Electrode Interface During Lithium Deposition and Stripping. *Chem. Mater.* **2017**, *29*, 3029−3037.
(337) Otoyama, M.; Ito, Y.; Hayashi, A.; Tatsumisago, M. Raman Imaging for LiCoO2 Composite Positive Electrodes in All-Solid-State Lithium Batteries Using Li2S−P2S5 Solid Electrolytes. *J. Power Sources* **2016**, *302*, 419−425.
(338) Zhang, W.; Weber, D. A.; Weigand, H.; Arlt, T.; Manke, I.; Schröder, D.; Koerver, R.; Leichtweiss, T.; Hartmann, P.; Zeier, W. G.; et al. Interfacial Processes and Influence of Composite Cathode Microstructure Controlling the Performance of All-Solid-State Lithium Batteries. *ACS Appl. Mater. Interfaces* **2017**, *9*, 17835−17845.
(339) Wang, H.; Downing, R. G.; Dura, J. A.; Hussey, D. S. In *Polymers for Energy Storage and Delivery: Polyelectrolytes for Batteries and Fuel Cells*; American Chemical Society, 2012; Vol. *1096*.
(340) Wang, C.; Gong, Y.; Dai, J.; Zhang, L.; Xie, H.; Pastel, G.; Liu, B.; Wachsman, E.; Wang, H.; Hu, L. In Situ Neutron Depth Profiling of Lithium Metal−Garnet Interfaces for Solid State Batteries. *J. Am. Chem. Soc.* **2017**, *139*, 14257−14264.
(341) Han, F.; Westover, A. S.; Yue, J.; Fan, X.; Wang, F.; Chi, M.; Leonard, D. N.; Dudney, N. J.; Wang, H.; Wang, C. High Electronic Conductivity as the Origin of Lithium Dendrite Formation within Solid Electrolytes. *Nature Energy* **2019**, *4*, 187−196.

https://dx.doi.org/10.1021/acs.chemrev.0c00101
Chem. Rev. XXXX, XXX, XXX−XXX